NAZARBAYEV UNIVERSITY

ENGINEERING OF METAL OXIDE NANOSTRUCTURES AND INTERFACES FOR APPLICATIONS IN PEROVSKITE SOLAR CELLS

by
Zhuldyz Yelzhanova

Submitted in partial fulfillment of the requirements for the degree of Doctor of Philosophy in Electrical Engineering

Date of Completion
April, 2026

APPENDIX: TITLE PAGE

ENGINEERING OF METAL OXIDE NANOSTRUCTURES AND INTERFACES FOR APPLICATIONS IN PEROVSKITE SOLAR CELLS

By

Zhuldyz Yelzhanova

Submitted in partial fulfillment of the requirements for the degree of

Doctor of Philosophy in Electrical Engineering

Department of Electrical and Computer Engineering

School of Engineering and Digital Sciences

Nazarbayev University

April, 2026

Supervised by

Prof. Ng Annie (Lead Supervisor)

Prof. Balanay Mannix (Co-supervisor)

Declaration

I, Zhuldyz Yelzhanova, declare that the research contained in this thesis, unless otherwise formally indicated within the text, is the author's original work. The thesis has not been previously submitted to this or any other university for a degree and does not incorporate any material already submitted for a degree.

Signature: 

Date: 16/04/2026

Abstract

Continued growth of the global population has driven electricity usage to unprecedented heights, placing pressure on conventional energy sources and accelerating the transition to renewable technologies. Among these, solar energy is especially attractive due to advances in materials science and scalable photovoltaic fabrication.

Although silicon-based photovoltaic cells dominate the market, their high-temperature and energy-intensive manufacturing underscores the demand for alternative technologies. Consequently, solution-processable perovskite solar cells (PSCs) have emerged as promising candidates, characterized by low-temperature fabrication, rapid power conversion efficiency (PCE) gains reaching 27% in just 17 years, and tunable bandgaps suitable for single-junction and tandem devices. However, persistent stability issues hinder the broader application of PSCs.

Central to this investigation is the electron transport layer (ETL)/perovskite interface, as it significantly impacts charge transport, recombination dynamics, and device stability. Accordingly, two distinct interfacial engineering techniques were investigated for different PSC architectures: hybrid organic-inorganic and all-inorganic perovskite-based solar cells.

The first approach focused on nanostructured ETLs, offering a large surface area, tunable geometric characteristics, and enhanced charge transport pathways for effective interfacial engineering. Considering that the solvothermal growth of SnO_2 nanorod arrays is highly sensitive to the synthesis conditions, every critical parameter was systematically optimized to establish a reliable and reproducible fabrication protocol. Several parameters are involved: reactor pressure, substrate orientation, solvent ratio, seed-layer configuration, acetic acid concentration, and growth duration. The findings emphasize the importance of precisely controlling growth parameters for effective interfacial engineering and provide a practical framework for future customization of specific nanorod shapes by adjusting the identified synthesis parameters.

In the second approach, an ultrathin MgO interlayer was incorporated between the ETL and the $CsPbI_2Br$. The influence of the MgO interlayer was evaluated through a comprehensive set of investigations, revealing that MgO-incorporated PSCs significantly improved the photovoltaic performance and stability. Following 7 weeks of storage, the MgO-incorporated devices maintained 70% of their initial PCE, whereas the unmodified counterparts dropped to 55%. The devices were further tested for their resilience against proton irradiation to assess their performance in harsh environments. The MgO-optimized devices exhibited high durability and demonstrated a slight improvement in photovoltaic parameters. In contrast, the unmodified devices showed a significant reduction, retaining only 47% of their initial performance after 11 weeks.

This thesis underscores the critical role of interfacial engineering in PSCs, demonstrating how innovative strategies enable the development of stable and efficient perovskite solar technologies.

Acknowledgments

This work owes its foundation to Professor Charles Surya, whose visionary leadership launched the perovskite photovoltaics research at Nazarbayev University. My genuine appreciation goes to my lead supervisor, Professor Annie Ng, whose constant support and expert guidance motivated me to continue my research after my Master's completion. Her insights, comprehensive approach to designing experiments, and dedication to excellence in every aspect have given me a deep understanding of the research process. Moreover, Professor Annie Ng spearheaded the acquisition and commissioning of state-of-the-art solar device fabrication equipment, establishing the optimal research infrastructure for our studies. Additionally, I sincerely thank my internal supervisor, Professor Mannix Balanay, for teaching me the basics of chemical experimentation, which established the foundation for all future investigations.

I am also grateful to my external supervisor, Professor Shifeng Wang, for his valuable guidance, support, and helpful discussions throughout this work. I sincerely thank the Examiners, Professor Alexander Tikhonov and Professor Sergey Makarov, for their careful evaluation of my work and for their insightful comments, which significantly improved this thesis.

I sincerely appreciate Professor Tri Pham and his students, Dr. Amanzhol Turlybekuly, Ms. Meruyert Tilegen and Mr. Timur Elebessov for their invaluable assistance in conducting KPFM measurements and for crucial help in designing our custom 3D-printed sample holder. I also extend my gratitude to Professor Marat Kaikanov for facilitating proton irradiation tests on my devices, a contribution that significantly strengthened this research.

I extend my heartfelt thanks to the Core Facility team. I sincerely thank to Dr. Aidos Baumuratov and Dr. Alexandr Arbuz. I am particularly grateful to Ms. Laura Khamkhash and Ms. Rakhima Shamenova. Through their patient guidance and dedicated mentorship, I gained the confidence and skill to independently operate the AFM and SEM instruments. I

am grateful to Ms. Nurgul Daniyeva and Mr. Alisher Rapikov; they have always been ready to help and eager to share their expertise with the equipment. I also acknowledge Mr. Arman Tuigynbek for his expert management of the XPS measurements and for providing comprehensive instruction on its fundamentals.

I extend my sincere gratitude to the School of Engineering and Digital Sciences faculty for their support and for delivering the core courses that underpinned my doctoral studies. I am particularly thankful to Professor Luis R. Rojas-Solorzano, Professor Mehdi Bagheri, and Professor Daniele Tosi for their steadfast administrative assistance throughout my PhD journey.

I have been fortunate to work alongside colleagues who became dear friends throughout my time in the laboratory. I especially thank my dream team, Dr. Gulzhan Zhumadil and Ms. Gaukhar Nigmetova, for their unwavering support, collaborative work on numerous experiments, and joint celebration of each success. I would like to express my appreciation to Dr. Damir Aidarkhanov, Dr. Yerassyl Yerlanuly, Mr. Alibek Kakim, and Mr. Almaz Beisenbayev for their timely support and help. I am also thankful to Dr. Hryhorii Parkhomenko for performing the current-voltage measurements on my electron-only devices and for his valuable guidance with other instruments.

I am deeply thankful to my family for their consistent belief in me. I extend my sincere gratitude to my parents and parents-in-law, whose relentless support and shared enthusiasm for science have motivated me, to my brother, whose deep passion for engineering ignited my interest in renewable energy, to my sister-in-law and niece, whose generous encouragement has helped me overcome every obstacle. Finally, I am especially grateful to my husband, whose steadfast support, heartfelt care, and constant encouragement made this PhD journey significantly easier—I am forever thankful to have him by my side.

Contents

List of Tables

List of Figures

List of Abbreviations

AC	alternating current
AFM	atomic force microscopy
AIST-NT	Advanced Integrated Scanning Tools for Nano-Technology
ALD	atomic layer deposition
AM	air mass
BE	binding energy
BHJ	bulk heterojunction
c-AFM	conductive AFM
c-Si	crystalline silicon
CB	chlorobenzene
CBD	common beam depolarizer
CBM	common beam mask
CBM	conduction-band minimum
CC	Creative Commons
CHCl	choline chloride
CIGSe	copper indium gallium selenide
CPD	contact potential difference
CTL	charge transport layer
CTM	charge transport materials
CZTSe	Copper Zinc Tin Selenide
DC	direct current
DI	deionized
DMF	N, N-dimethylformamide
DMSO	dimethyl sulfoxide
DOD	drop-on-demand
DSSC	dye-sensitized solar cells

EDS	energy dispersive spectroscopy
EOD	electron only device
EQE	external quantum efficiency
ETL	electron transport layer
FA	formamidinium
FAI	formamidinium iodide
FF	fill factor
FS	forward scan
FTO	fluorine-doped tin oxide
GaAs	Gallium Arsenide
GHJ	graded heterojunction
GW	gigawatts
$HCOO^-$	pseudo-halide anion formate
HI	hysteresis index
HTL	hole transport layer
HTM	hole transport material
HV	high voltage
i-NURA	Ion-Nazarbayev University Research Accelerator
IEL	ionizing energy loss
IL	ionic liquid
IPA	isopropanol
IQE	internal quantum efficiency
ITO	indium tin oxide
IV	current-voltage
IVA	induction voltage adder
K	potassium
KI	potassium iodide

KPFM	kelvin probe force microscopy
Li-TFSI	bis(trifluoromethane)sulfonimide lithium salt
M-O	metal-oxygen
MA	methylammonium
MACl	methylammonium chloride
MAI	methylammonium Iodide
MOFs	metal-organic frameworks
mp	mesoporous
MPP	maximum power point
NA	nanorod array
NIEL	non-ionizing energy loss
NIR	near-infrared
OA	oleic acid
OPV	organic photovoltaic
P3HT	poly-3-hexylthiophene
PCBM	[6,6]-phenyl-C61-butyric acid methyl ester
PCE	power conversion efficiency
PEDOT:PSS	poly(3,4-ethylenedioxythiophene)poly(styrene sulfonate)
PET	polyethylene terephthalate
PI	proton irradiation
PM6	poly[(2,6-(4,8-bis(5-(2-ethylhexyl-3-fluoro)thiophen-2-yl)-benzo[1,2-b:4,5-b′]dithiophene))-alt-(5,5-(1′,3′-di-2-thienyl-5′,7′-bis(2-ethylhexyl)benzo[1′,2′-c:4′,5′-c′]dithiophene-4,8-dione)]
PMMA	poly(methyl methacrylate)
PSC	perovskite solar cell
PTAA	poly-triarylamine
PV	photovoltaics

QD	quantum dot
quasi-2D DJ	quasi-two-dimensional Dion-Jacobson
RF	radio frequency
RMS	root mean square
RS	reverse scan
SAM	Self-assembled monolayer
SCLC	space charge limited current
SDBS	sodium dodecyl benzene sulfonate
SEM	scanning electron microscope
SG	spark gap
Sn	tin
Spiro-MeOTAD	2,2′,7,7′-Tetrakis(N,N-di-p-methoxyphenylamino)-9,9′-spirobifluorene
SPM	scanning probe microscope
TBP	4-tert butylpyridine
TL	transmission lines
UPS	ultraviolet photoelectron spectroscopy
VBM	valence-band maximum
VIS	visible
VTFL	trap-filled-limit voltage
WF	work function
XPS	x-ray photoelectron spectroscopy
XRD	x-ray diffraction

List of Symbols

C	capacitive storage
d	distance
ΔE	change in energy
$E_{cut\text{-}off}$	electron cutoff
E_f	Fermi energy
E_g	bandgap energy
J_D	current density
J_{sc}	short-circuit current density
n	integer
n_{trap}	trap-state density
q	elementary charge
r	decay rate
S	switch
t	irradiation time
Tr	transformer
V_{oc}	open-circuit voltage
ε_r	relative dielectric constant
ε_0	permittivity of the vacuum
η	efficiency/power conversion efficiency
μ_n	carrier mobility
ϕ_{sample}	WF of sample
ϕ_{tip}	WF of tip
λ	wavelength
θ	the angle

List of Publications

Published journal papers:

1. **Yelzhanova Z**, Nigmetova G, Mukasheva D, Parkhomenko H, Zhumadil G, Aidarkhanov D, Kaikanov M, Elebessov T, Wang T, Kalmakhanbet A, Duan D, Hu H, Pham T, Balanay M, Jumabekov A, Ng A. Solution-Processed Magnesium Oxide Buffer Layer for Improved Stability of $CsPbI_2Br$ Perovskite Solar Cells. Solar RRL. 2026 January 10. Available from: https://doi.org/10.1002/solr.202500762
2. **Yelzhanova Z**, Nigmetova G, Aidarkhanov D, Daniyar B, Baptayev B, Balanay MP, Jumabekov AN, Ng A. A morphological study of solvothermally grown SnO_2 nanostructures for application in perovskite solar cells. Nanomaterials. 2022 May 15;12(10):1686. Available from: https://doi.org/10.3390/nano12101686
3. Nigmetova G, **Yelzhanova Z**, Zhumadil G, Parkhomenko HP, Tilegen M, Zhou X, Pavlenko V, Beisenbayev A, Aidarkhanov D, Jumabekov AN, Kaikanov M, Pham TT, Balanay MP, Lim CK, Wang Y, Hu H, Ng A. Controlling the growth of Cs_2PbX_4 nanostructures enhances the stability of inorganic Cesium-Based perovskite solar cells for potential low Earth orbit applications. ACS Applied Materials & Interfaces. 2025 May 16; Available from: https://doi.org/10.1021/acsami.5c03064
4. Zhumadil G, Cao M, Han Y, Pavlenko V, Nigmetova G, **Yelzhanova Z**, Parkhomenko HP, Ergasheva Z, Aidarkhanov D, Balanay MP, Jumabekov AN, Li G, Ren Z, Ng A. Ionic Liquid-Assisted Strategy for morphology engineering of inorganic Cesium-Based perovskite thin films toward High-Performance solar cells. ACS Applied Materials & Interfaces. 2024 Oct 31; Available from: https://doi.org/10.1021/acsami.4c15880
5. Goponenko D, Zhumanova K, Shamarova S, **Yelzhanova Z**, Ng A, Atabaev TSh. Hydrophobic and luminescent polydimethylsiloxane PDMS-Y_2O_3:EU^{3+} coating for power enhancement and UV protection of SI solar cells. Nanomaterials. 2024 Apr 12;14(8):674. Available from: https://doi.org/10.3390/nano14080674
6. Aidarkhanov D, **Yelzhanova Z**, Ren Z, Nigmetova G, Lau SP, Balanay MP, Hu H, Surya C, Djurišić AB, Ng A. Synergic effects of incorporating black phosphorus for interfacial engineering in perovskite solar cells. Surfaces and Interfaces. 2023 Oct 21;43:103531. Available from: https://doi.org/10.1016/j.surfin.2023.103531
7. Remizov A, Tukaziban A, **Yelzhanova Z**, Junussova T, Karaca F. Adoption of Green Building Assessment Systems to Existing Buildings under Kazakhstani Conditions. Buildings. 2021 Jul 28;11(8):325. Available from: https://doi.org/10.3390/buildings11080325

8. Aidarkhanov D, Ren Z, **Yelzhanova Z**, Baptayev B, Balanay M, Surya C, Ng A. Interfacial engineering for high performance perovskite solar cells. Materials Today Proceedings. 2021 Jan 25;49:2482–6. Available from: https://doi.org/10.1016/j.matpr.2020.11.918
9. Aidarkhanov D, Ren Z, Lim CK, **Yelzhanova Z**, Nigmetova G, Taltanova G, Baptayev B, Liu F, Cheung SH, Balanay M, Baumuratov A, Djurišić AB, So SK, Surya C, Prasad PN, Ng A. Passivation engineering for hysteresis-free mixed perovskite solar cells. Solar Energy Materials and Solar Cells. 2020 Jul 31;215:110648. Available from: https://doi.org/10.1016/j.solmat.2020.110648

Conference proceedings:

1. **Yelzhanova Z**, Nigmetova G, Bizhanova G, Yermekov N, Kashkimbayev U, Ng A. Optimization of Zinc Oxide Electron Transport Layers for Cs-based Perovskite Solar Cells**.** 2023 IEEE 50th Photovoltaic Specialists Conference (PVSC). 2023. Available from: https://doi.org/10.1109/pvsc48320.2023.10359713
2. **Yelzhanova Z**, Nigmetova G, Aidarkhanov D, Maxim A, Baptayev B, Balanay M, Surya C, Ng A. Optimization of Tin (IV) Oxide Nanostructures Grown by a Solvothermal Method for Perovskite Solar Cells. 2020 IEEE 47th Photovoltaic Specialists Conference (PVSC). 2020. Available from: https://doi.org/10.1109/pvsc45281.2020.9300951
3. Zhumadil G, Pavlenko V, Nigmetova G, **Yelzhanova Z**, Balanay MP, Ng A. Engineering $CsPbI_2Br$ Perovskite Thin Film Morphology with Ionic Liquid Additives for Enhanced Performance Solar Cells**.** 2024 IEEE 52nd Photovoltaic Specialist Conference (PVSC). 2024. Available from: https://doi.org/10.1109/pvsc57443.2024.10749384
4. Aidarkhanov D, Maxim A, Ren Z, **Yelzhanova Z**, Ualibek O, Daniyar B, Saibitihan A, Balanay M, Djurisic A, Surya C, Ng A. Optimization of electron transport layers for high performance perovskite solar cells. 2022 IEEE 6th Electron Devices Technology &Amp; Manufacturing Conference (EDTM). 2020 Apr 1;4:1–4. Available from: https://doi.org/10.1109/edtm47692.2020.9118013
5. Ng A, Surya C, Ren Z, Aidarkhanov D, **Yelzhanova Z**, Nigmetova G, Maxim A, Akhmetov B, Fong PWK, Djurisic AB. Effective Strategies for High Performance Hysteresis-free Mixed Perovskite Solar Cells**.** 2019 IEEE 46th Photovoltaic Specialists Conference (PVSC). 2019. Available from: https://doi.org/10.1109/pvsc40753.2019.8980784

CHAPTER 1: INTRODUCTION

1.1 Renewable Energy

World energy consumption continues to steadily rise alongside the growing global population. Although the adverse effects of relying on non-renewable energy sources, including air pollution, climate change, resource depletion, and habitat destruction, are becoming increasingly severe, renewable energy sources, such as solar, geothermal, wind, and biomass, offer a sustainable alternative to fossil fuels. The International Energy Agency's Renewables 2024 – Global Overview[1] forecasts a ~60% rise in the consumption of renewable energy across the sectors of electricity, heating, and transportation over the next 6 years. This growth increases the proportion of renewables, which are expected to contribute to approximately 20% of the final energy consumption, with solar and wind being the primary drivers compared with 13% of the final energy consumption in 2023. Kazakhstan is also demonstrating progress in moving toward cleaner energy sources, reporting[2] that the country has 146 active renewable energy facilities with a total installed capacity of 2.9 gigawatts (GW) as of March 2024, including various wind, solar, hydroelectric, and biogas power plants.

Solar energy stands out among various renewable sources because of its availability and simple solid-state conversion into electricity. The Sun emits a massive amount of energy approximately 3.86×10^{26} W,[3] of which about 1.75×10^{17} W[3] is intercepted by the Earth. The rest of the incoming solar energy is dispersed, reflected, or absorbed by clouds and the atmosphere, without reaching the Earth's surface. In one and a half days, the Earth's surface receives 1.7×10^{22} J[4] of solar energy, which is equivalent to the energy produced by burning three trillion barrels of oil. This highlights the enormous potential of solar energy, which far exceeds the limited reserves of fossil fuels. Moreover, owing to notable advancements in photovoltaic (PV) technology, solar energy tends to be the cheapest energy source.[5]

As of now, silicon (Si) solar cells maintain their dominance in the commercial PV

market, given their mature manufacturing processes, decreased production costs of Si-based solar cells resulting from the expanding market, and durability. Despite their advantages, the indirect band gap of 1.1 eV[6] in Si-based solar cells limits efficiency, preventing them from fully realizing their theoretical maximum, as described by the Shockley–Queisser limit. Specifically, a power conversion efficiency (PCE) of 33.16% is expected if the solar cell material has a bandgap between 0.93 and 1.61 eV range, achieving the maximum efficiency at 1.34 eV.[7] Nevertheless, PV technology is continuously improving, and new innovative materials for solar cells are being developed to surpass the PCE limits of Si-based solar cells and adapt to more diverse applications. In recent years, interest in perovskite solar cells (PSCs) has intensified owing ever-improving PCE, simple manufacturing, and economic efficiency. Since their debut in 2009, PSCs have developed rapidly, achieving energy conversion efficiencies comparable to conventional Si - solar cells while promising much lower manufacturing costs. In April 2025, 26.95%[8] PCE was reached through the collaborative efforts of Soochow University in China and the University of New South Wales in Australia.

PSCs' lightweight and flexible characteristics enable their use in various applications beyond traditional rooftop installations. Their versatility enables seamless integration into architectural elements (e.g., facades and windows), which is often referred to as building-integrated PVs, as well as portable electronics and electric vehicles. These attributes position PSCs as significant contributors to the advancement of renewable energy technologies, particularly in areas where conventional Si-based PVs encounter limitations. Although PSCs offer numerous advantages, they are vulnerable to environmental factors such as humidity, heat, and UV radiation, which severely limits their lifetime and reliability, inhibiting their widespread commercialization.

1.2 Problem Statement

PSCs represent a promising PV technology with high PCE, cost-effective fabrication, and

tunable optoelectronic properties. However, their widespread adoption remains limited by their stability issues, as perovskite material degrades under environmental conditions such as moisture, heat, and UV exposure. Given the urgent global demand for reliable, low-cost, and sustainable energy solutions, addressing the instability of PSCs is a critical step toward their commercial viability and large-scale implementation. To address this, various engineering techniques have been investigated. Among these approaches, interface engineering has emerged as one of the most effective strategy because the interfaces strongly influence charge carrier dynamics, energy level alignment, and defect formation, ultimately improving charge transport, reducing recombination losses, and enhancing the device's overall stability. Optimizing these interfacial properties is essential for achieving high PCE and ensuring long-term operational stability and reproducibility.

A critical component of PSCs is the electron transport layer (ETL), which facilitates efficient electron extraction, minimizes charge recombination and influences interfacial energy alignment. The overall effectiveness of the ETL depends not only on its intrinsic properties, but also on its interfacial compatibility with the perovskite absorber. Choosing an appropriate ETL is essential, because it directly affects perovskite film formation, energy level matching, and charge transfer dynamics. An incompatible ETL can lead to poor film coverage, increased trap-state density, and accelerated device degradation. While many metal oxide ETLs offer desirable characteristics, such as high electron mobility and optical transparency, their interfaces with perovskite layers often require further optimization to suppress non-radiative recombination losses and ensure long-term operational stability. Hence, understanding and engineering the interaction between the ETL and the perovskite is fundamental to developing high-performance and durable PSCs.

Throughout this work, I undertook extensive experimental efforts to explore how different ETL materials and structures interact with hybrid and all-inorganic perovskites. Special emphasis was placed on developing and integrating 1D nanostructured ETLs, such as vertically aligned nanorods. Another architectural approach involved the investigation of

an ultrathin interfacial layer between the ETL and absorber layer.

This research involved device fabrication, detailed material characterization, and performance analysis. The findings from this study provide insight into the optimization of ETL/perovskite interface, contributing to the advancement and commercialization of high-efficiency and stable PSCs.

1.3 Research Questions

- Why is achieving a high-quality interface between the charge transport layer (CTL) and perovskite absorber critical for the performance and stability of PSCs?
- How can optimizing the interface between the CTL and perovskite layer improve charge carrier dynamics and operational stability?
- How can interfacial engineering strategies be used to enhance the long-term operational stability of PSCs?
- What strategies can be employed to control the growth and morphology of nanostructured ETLs for PSC applications?
- What is the effect of engineering different ETL-based heterojunction architectures on the interfacial charge transport and recombination processes in PSCs?
- What is the influence of incorporating ultrathin interfacial layers between the ETL and perovskite absorber on interfacial energy alignment, film formation, and device performance?
- How do PSCs with engineered interfaces perform under different environmental conditions?

1.4 Thesis Outline

The organization of the thesis is as follows:

- Chapter 1 introduces renewable energy technologies, outlines the problem statement behind this research, and presents the overall objectives of the study.

- Chapter 2 reviews the evolution of solar cell technologies, discusses the background of perovskite materials, and outlines the historical development of PSCs. It also highlights key challenges and summarizes recent strategies aimed at improving stability and efficiency.
- Chapter 3 explain the experimental methodology of sample preparation, device fabrication procedures, and characterization techniques employed throughout the study. Furthermore, the results of advanced cross-sectional characterization are shown.
- Chapter 4 presents a morphological study of ETL nanostructure for hybrid organic-inorganic PSCs.
- Chapter 5 investigates the effects of modified ETL by incorporation of thin interfacial layer on the PV performance and stability of cesium-based PSCs.
- Chapter 6 summarizes the key findings of the research, draws conclusions, and outlines recommendations for future work.

CHAPTER 2: LITERATURE REVIEW

2.1 Development of Solar Energy

To date, PV technology has progressed through three generations, with first-generation solar cells currently dominating the market (Figure 2.1). These cells are primarily composed of mono and polycrystalline cells manufactured from silicon wafers. Their widespread adoption is attributed to their high efficiency (15%–25%), stability, and long operational lifetime exceeding 20 years.[9] Despite significant advantages, first-generation PV cells face notable disadvantages, which are mainly attributed to Si wafer production and processing. Furthermore, conventional solar cells exhibit thermal sensitivity[10] leading to efficiency losses at elevated temperatures, thus impacting overall performance, particularly in high-temperature operating environments

In pursuit of more cost-efficient solutions, the second generation of cells emerged, focusing on thin-film technology comprising microcrystalline and amorphous Si, cadmium telluride, and other materials. The fabrication of thin-film devices is based on the deposition of PV materials onto rigid and flexible substrates composed of glass, plastic, polymer, or metal.[11] These cells are significantly thinner (1 μm) than first-generation solar cells (350 μm).[9] Moreover, although this generation of cells achieved a lower PCE (10%–15%), innovative low-temperature manufacturing techniques were developed and applied, which reduced material waste and costs, and made solar technology more accessible. One of the primary limitations of second-generation solar cells is light-induced degradation[12] in amorphous Si, which negatively impacts long-term stability and efficiency.

The leading edge of PV cells research is currently in its third generation, encompassing a wide range of new materials and technologies, such as organic PV, dye-sensitized solar cells (DSSCs), multi-junction cells, quantum dot (QD) solar cells, etc.[9] This generation of cells is designed to achieve even lower manufacturing costs without compromising the PCE. These new cells also aim to overcome the Shockley–Queisser limit in single-bandgap cell configurations, with some experimental multi-junction setups

reporting up to 40%.[13] Notably, third-generation technologies exhibit the fastest efficiency improvement rate compared with their predecessors. However, a major challenge remains in ensuring long-term stability, considering that many third-generation solar cells are susceptible to degradation under regular environmental conditions. Thus, improving stability and efficiency is the focus of ongoing research on these solar cells. One type of promising solar cell that belongs to this generation is the PSC.

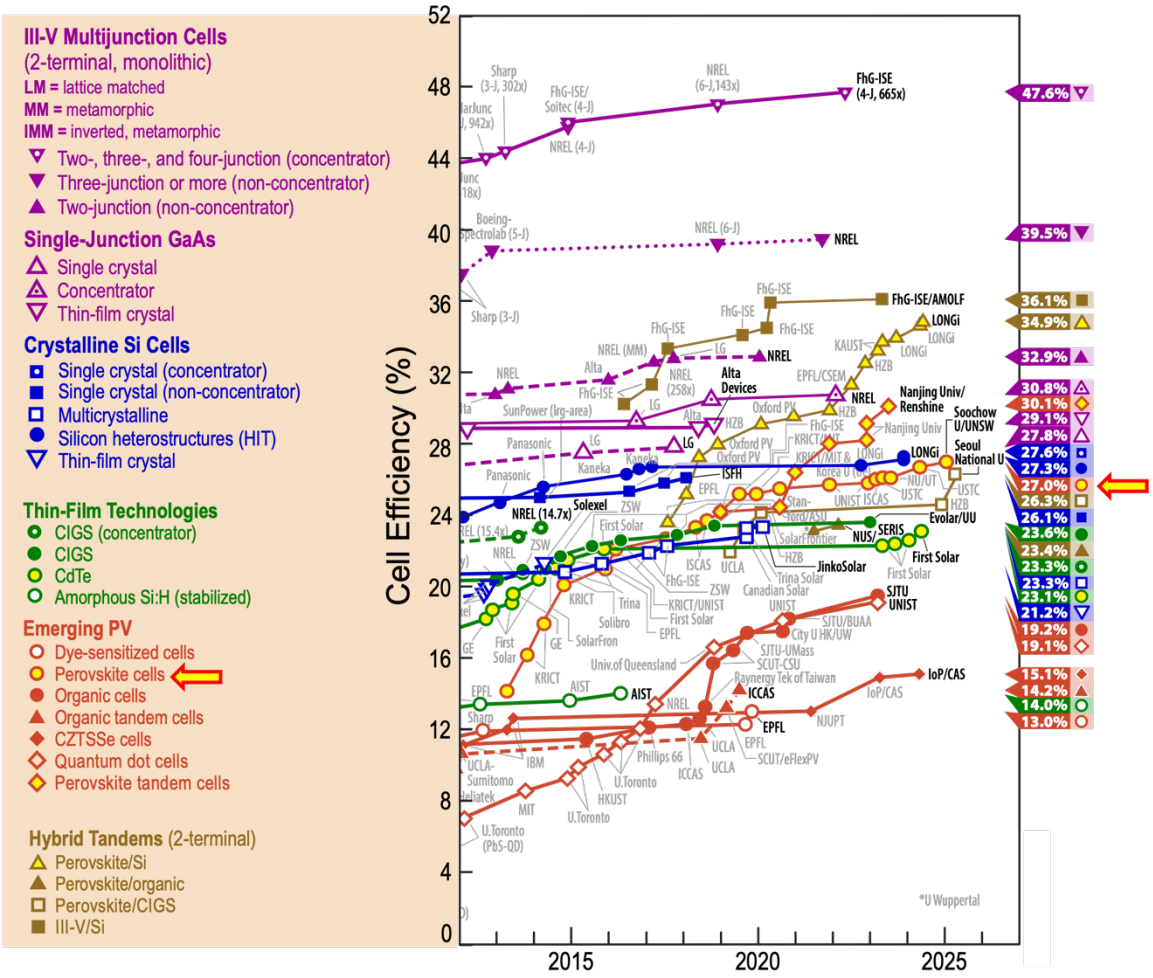

Figure 2.1 Evolution of the best research-based cell efficiencies across PV technologies.[8] The chart was last updated on April 21, 2025

2.2 Fundamentals of PSCs

2.2.1. Perovskite Structure and Composition

The term "perovskite" refers to a class of materials with ABX_3 crystal structure (Figure 2.2), exhibiting a unique three-dimensional crystal structure. This structure contains three main components:

- ***A-site Cations:*** This large cation can be an organic molecule, such as methylammonium ($CH_3NH_3^+$) and formamidinium ($HC(NH_2)_2^+$), or an inorganic ion like cesium (Cs^+), rubidium (Rb^+), and potassium (K^+).[14,15] The A-site cations reside in the cuboctahedral cavities of the corner-sharing BX_6 octahedral framework, where they ensure charge neutrality and structural stability of the lattice.[16–19] Based on the number of A-site cations present in the crystal structure, perovskites can be classified as single, double, triple, or quadruple A-cation perovskites.[14]
- ***B-site Cations:*** The B cation is smaller than the A cation and is commonly a divalent metal ion, most often lead (Pb^{2+}) or tin (Sn^{2+}).[14] The choice of this metal impacts the electronic band structure and charge transport properties of the material, which are critical factors in determining the efficiency.[20]
- ***X-site Anions*:** The X-site anion consists of a halide ion such as iodide (I^-), bromide (Br^-), or chloride (Cl^-).[14] These halide ions substantially affect the optical and electronic properties of perovskite materials by altering the bandgap,[21] which significantly influences light absorption and overall efficiency in PV applications.

The ideal perovskite structure is cubic, where B-site cations exhibit sixfold coordination, being surrounded by an octahedral arrangement of X-site anions.[22] Meanwhile, the A-site cations are positioned in 12-fold cuboctahedral coordination. Figure 2.2a illustrates the three-dimensional arrangement of the ABX_3 lattice, highlighting the spatial relationship among the A, B, and X ions and the overall symmetry of the structure. Figure 2.2b shows a planar slice of the crystal, making it easier to visualize the atomic arrangement and connectivity within a single layer of the perovskite lattice. Finally, Figure 2.2c focuses on the unit cell, the smallest repeating unit of the perovskite lattice, clearly showing the positions of the A, B, and X ions and their coordination environments.

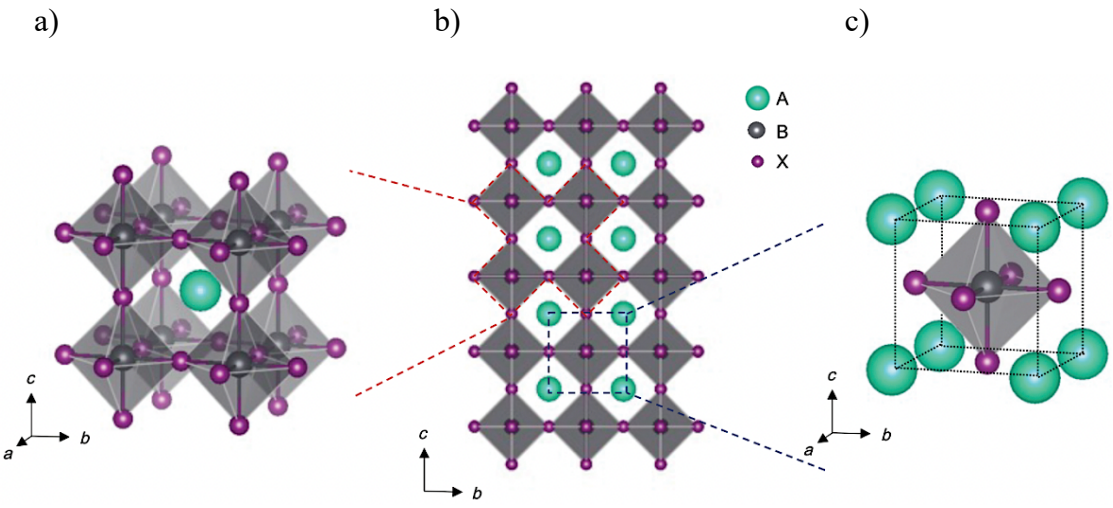

Figure 2.2 Illustrations of the a) 3D cubic perovskite material, b) 2D projection, and c) unit cell structure; reprinted from Ref.[22] with permission (Order №: 6030460337609)

Owing to their high structural tolerance, PSCs have easily tunable band gaps.[23] This characteristic reduces the need for strict lattice matching between subcells in solar cell configurations, allowing greater flexibility in material selection. Perovskite structural stability is frequently analyzed using the Goldschmidt tolerance factor, expressed as:[23]

$$t = \frac{r_A + r_B}{\sqrt{2}(r_A + r_X)} \tag{2.1}$$

where r_A, r_B, and r_X are ionic radiuses of the A cation, B cation and X anion, respectively. A tolerance factor of $0.81 \leq t \leq 1$[24] ensures the formation of a three-dimensional metal halide perovskite structure, preventing structural distortions or transitions into non-perovskite phases. A tolerance factor exceeding 1[24] usually signifies an oversized A-site cation, which generally prevents perovskite formation. Conversely, if t drops below 0.8,[24] the A-site cation may be undersized, often causing the structure to deviate into alternative non-perovskite phases. Meanwhile, the tolerance factor of 1[24] represents an ideal perovskite structure, where the ionic radii of the A-site, B-site, and X-site ions are perfectly matched.

2.2.2 Working Principle

A typical PSC consists of several layers that work together to generate electricity. The structure includes five main components (Figure 2.3a):

- ***Transparent Conductive Oxides (TCO):*** Transparent electrodes efficiently collect charge carriers while also functioning as anti-reflective coatings to enhance light

absorption.[25] Two common types of TCOs are indium tin oxide (ITO), consisting of indium oxide (In_2O_3) doped with tin oxide (SnO_2), and fluorine-doped tin oxide (FTO). is widely adopted owing to high transmittance, high electrical conductivity, minimal light absorption, and durability.[25] FTO exhibits low resistivity and offers greater chemical, thermal, and mechanical stability compared to the ITO while also more cost-effective in deposition.[26]

- ***ETL:*** This layer collects photogenerated electrons from the absorber layer and transfers them to the cathode. The choice of ETL material impacts the interfacial properties between the electrode and the perovskite layer, influencing charge extraction and the device's overall performance.
- ***Perovskite Layer:*** This layer contains the main light-absorbing component. The strong absorption capability of the perovskite across a broad range of wavelengths enables the generation of high-density charge carriers.
- ***Hole Transport Layer (HTL):*** This layer facilitates the extraction of photogenerated holes from the absorber and efficiently transports them to the anode. HTL material choice greatly influences the interfacial properties, charge extraction, and overall solar cell performance.
- ***Metal Electrode:*** This electrode serves as the back contact and is typically composed of gold (Au), silver (Ag), copper (Cu), or aluminum (Al). Among these metals, Au is the most commonly used because of its high work function (WF), high conductivity, and chemical stability, although its high-cost limits scalability. Ag and Cu are considered more cost-effective alternatives, but they pose challenges related to diffusion and performance degradation in PSCs. Al is sometimes employed in inverted PSC architectures.

The working principle of PSC is based on the PV effect, involving light absorption, charge generation, charge separation, and charge collection, as illustrated in Figure 2.3b. When sunlight strikes the absorber, photons with energy above the material bandgap are

absorbed, exciting electrons from the valence band to the conduction band and creating electron-hole pairs.[27] The absorbed photons generate free electrons and holes in the perovskite layer, and these charge carriers can move independently owing to the material's unique electronic structure. The built-in electric field within the solar cell separates the photogenerated electrons and holes preferentially, with electrons moving toward the ETL and holes moving toward the HTL. Thus, electrons are collected at the cathode, while the holes are gathered at the anode.[27] The flow of these charge carriers through an external circuit produces an electric current.

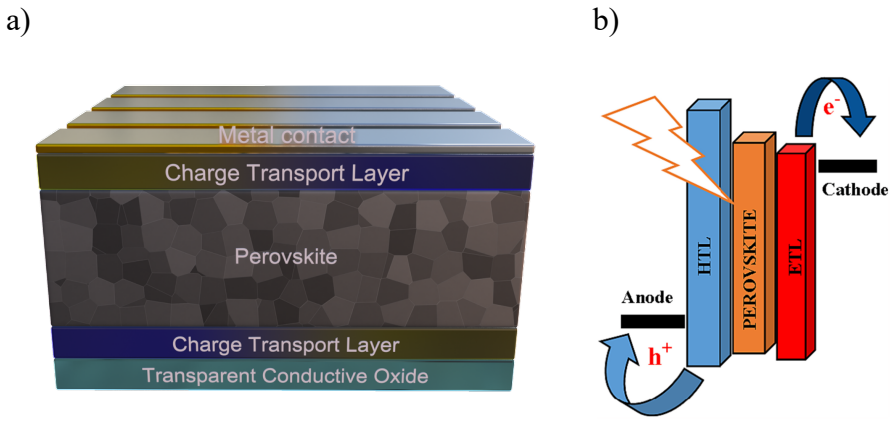

Figure 2.3 a) Basic PSC structure. b) PSC working principle; reproduced from Ref.[27] under Creative Commons CC BY 4.0

2.3 Historical Background

The original perovskite mineral, with the chemical formula $CaTiO_3$, was first discovered in 1839 in mineral-rich deposits located in the Ural Mountains.[28] The material was named in honor of the mineralogist and statesman Lev A. Perovski.[29] Perovskite crystals exhibit a hardness of 5.5 to 6 on the Mohs scale, making them moderately hard,[28] and the density is between 4000 and 4300 kg/m³, which contributes to their robust structural properties.[28] The other material characteristics are outlined in Table 2.1.

Table 2.1 Characteristics of perovskite material. Adapted from Ref [30] with permission (Order №: 6030870755046)

Features	Values range
Bandgap	1.5–2.5 eV
Absorption coefficient	10^5 cm^{-1}
Exciton binding energy	<10 meV
Crystallization energy barrier	56.6–97.3 kJ mol^{-1}
PL quantum efficiency	70%
Charge carrier lifetime	>300 ns
Relative permittivity	3
Carrier mobility	800 cm^2 /Vs
Carrier diffusion length	>1 μm
Trap-state density	10^{10} cm^3 (single crystals) 10^{15}–10^{17} cm^3 (polycrystalline)

In 1998, Mitzi *et al.*[31] investigated the optoelectronic characteristics of hybrid perovskites, and found pronounced excitonic properties, suggesting the material's potential for use in light-emitting diodes, transistors, and PV devices. The evolution of the PSC architecture began in 2009 with the pioneering work of Kojima *et al.*[32] on synthetic organic-inorganic hybrid perovskite nanocrystals. This discovery represented a significant milestone in PV technology because these nanocrystals exhibited potential as alternative light absorbers and sensitizers. The liquid electrolyte DSSCs (Figure 2.4a) inspired the earliest PSC designs, demonstrating proof-of-concept performance with $CH_3NH_3PbI_3$/$MAPbI_3$ and $CH_3NH_3PbBr_3$/$MAPbBr_3$ structures achieving PCEs of 3.8% and 3.1%, respectively.[33] However, these DSSCs suffered from significant stability issues, primarily attributed to the perovskite dissolution in the highly corrosive iodide-based electrolyte, severely restricting the device's stability and shelf-life to just a few minutes. These limitations highlighted the need for a solid-state HTL, leading to the development of mesoscopic architectures with solid-state charge transport materials (CTMs). In 2012, Kim *et al.*[34] reached a PCE of 9.7% and extended the shelf-lifetime to over 500 h under ambient conditions, using 2,2′,7,7′-tetrakis[*N*,*N*-di(4-methoxyphenyl)amino]-9,9'- spirobifluorene (Spiro-OMeTAD)[35] as the HTL (Figure 2.4b). Moreover, there was a notable enhancement in the short-circuit current density (J_{sc}) and open-circuit voltage (V_{oc}), further reinforcing the transition to fully solid-state device architectures. At the same time, Li *et al.*[36] introduced a new architecture by

replacing n-type TiO_2 with a mesoporous (mp) insulating Al_2O_3 layer. Notably, $MAPbI_{3-x}Cl_x$ deposited on mp-Al_2O_3 scaffold outperformed those fabricated on TiO_2, achieving 10.9% and 7.6% efficiency, respectively. Considering the lack of an electron extraction layer, this configuration was designated as a meso-superstructured solar cell.

As research in the PV area progressed, various architectural modifications of PSCs were investigated and improved. Following the recognition of surface trap states in mp-TiO_2 as a significant factor limiting performance, in 2013, Ball *et al.*[37] introduced a planar heterojunction (PHJ) thin-film architecture incorporating a perovskite layer. This design, commonly employed in PV technologies such, as organic PVs (OPVs), gallium arsenide (GaAs), copper indium gallium selenide (CIGSe), and copper zinc tin selenide (CZTSe), replaced mp-TiO_2 with a compact n-type TiO_2 layer. A thin p-type Spiro-OMeTAD layer also encapsulated the intrinsic perovskite layer, serving as a hole transport material (HTM) (Figure 2.4c). The transition to a planar n-i-p architecture allowed for the fabrication of PSCs at significantly lower processing temperatures, from 500 to 150 °C. Consequently, this advancement in fabrication led to reduced manufacturing costs and enabled the possibility of high-throughput printed electronics on flexible substrates. Moreover, the PHJ achieved a high internal quantum efficiency (IQE), demonstrating that perovskite thin films can function as intrinsic layers with long carrier lifetimes and extended diffusion lengths for both electrons and holes.

In parallel, in 2013, Jeng *et al.*[38] identified the electron transport ability of [6,6]-phenyl-C61-butyric acid methyl ester (PCBM) by fabricating a $CH_3NH_3PbI_3$/fullerene absorber layer - based PHJ structure. By inverting the p- and n-type CTLs and effectively reversing the carrier flow, the device achieved a PCE of 3.9% (Figure 2.4d).

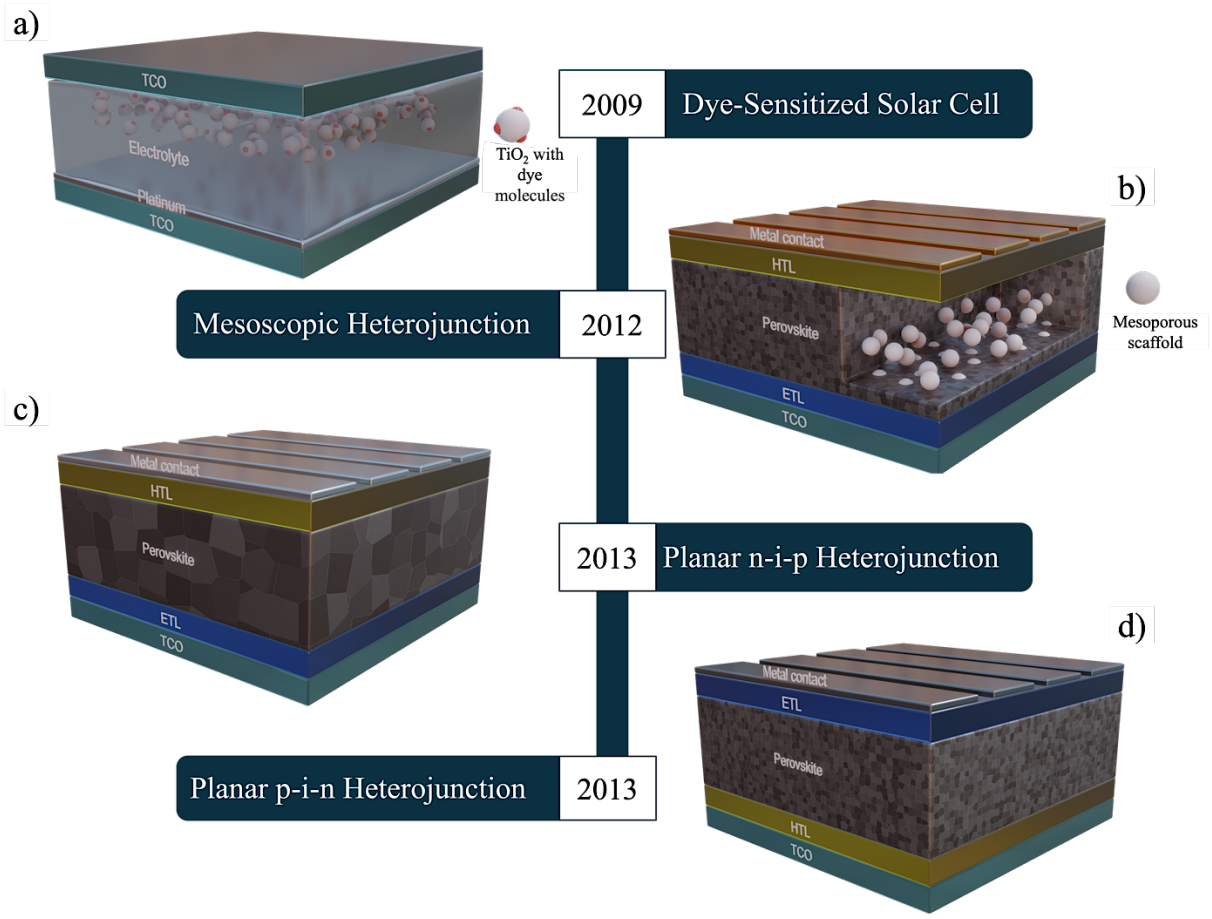

Figure 2.4 Evolution of perovskite-based solar cells. The earliest PSCs were adapted from a) DSSC technology. b) Mesoscopic heterojunction in which the perovskite absorber is infiltrated into a mp-TiO_2 scaffold and capped with a solid-state HTL. c) n-i-p PHJ thin-film architecture. d) p-i-n PHJ thin-film architecture

At the same time, Burschka *et al.*[39] discovered that solution-processable organic-inorganic hybrid perovskites, such as $CH_3NH_3PbX_3$ (X = Cl, Br, I), exhibited useful light-harvesting properties in mesoscopic solar devices. Initially, absorber films were deposited using a single-step fabrication technique. However, this method led to morphological inconsistencies due to uncontrolled deposition, thereby limiting the device's performance and reproducibility. The two-step method was conducted by introducing PbI_2 into an mp-TiO_2 film and then transforming it into perovskite by exposing it to a CH_3NH_3I solution. This innovative fabrication technique enabled better control over the perovskite formation, providing a uniform morphology and superior device reproducibility. Thus, PCE of 15 % was observed for the champion device, employing the sequential deposition technique in solid-state PSCs.

In 2014, Im *et al*.[40] employed a two-step solution process to fabricate $MAPbI_3$-PSCs. They achieved 17% PCE for the champion device by adjusting the size of the perovskite cuboids to optimize the light-collection and charge transfer efficiency. Their findings revealed that cuboid size was influenced by the concentration of the methylammonium iodide (MAI) solution and the exposure time of PbI_2 to MAI before spin-coating. One of the earliest demonstrations of nanostructured ETLs in PSCs was presented by Dong *et al.*,[41] who adapted DSSC technology, namely growing vertically aligned ZnO nanowire arrays[42] on a seed layer and applied it to PSCs. However, the developed architecture suffered significant recombination losses at the $ZnO/CH_3NH_3PbI_3$ interface, highlighting the need to modify the structure. Thus, ZnO was doped with Al, demonstrating increased electron density and faster electron mobility. As a result, the optimized nanostructured architecture (Figure 2.5a) resulted in an average PCE of 10.07 %, compared with 8.5 % for the control devices. Later, Löper *et al.*[43] introduced the first perovskite/silicon tandem solar cell (Figure 2.5b). A four-terminal architecture, consisting of a $CH_3NH_3PbI_3$ top cell and crystalline silicon (c-Si) bottom cell was employed to leverage their complementary bandgaps for enhanced light harvesting. The tandem cell achieved a combined efficiency of 13.4% under simulated sunlight, with 6.2% from the perovskite cell and 7.2% from the c-Si cell.

In 2015, Wang *et al.* [44] introduced the first bulk heterojunction (BHJ) hybrid PSCs to address the imbalance in charge carrier diffusion lengths in planar devices (Figure 2.5c). By blending perovskite materials with fullerene derivatives, the BHJ structure enlarged the interfacial area, improving charge carrier extraction and reducing recombination losses. This approach achieved a record fill factor (FF) of 86.7% while also demonstrating a 22% improvement in PCE compared with the planar architecture. Meanwhile, the work on mesoporous architectures continued; Giordano *et al.*[45] enhanced the electronic properties of the mp-TiO_2 layer by introducing lithium (Li), resulting in a high efficiency of 19.3%. The optimized structure exhibited enhanced electronic properties and faster electron transfer, attributed to reduced electron traps. This modification significantly minimized the hysteresis

loss, reaching a value of less than 0.3%. At the same time, Yang *et al.*[46] replaced the $MAPbI_3$ absorber layer with $FAPbI_3$, discovering that substituting methylammonium (MA) with formamidinium (FA) led to an enhanced PCE of 20.1%. Although these architectures demonstrated high performance, exceeding 20% PCE, the reliance of PSCs on daylight operation highlighted the necessity for alternative energy storage solutions, including solar fuel production, which demands substantial potential energy. Heo and Im[47] developed hybrid tandem PSCs using a lamination fabrication technique, integrating single-junction $MAPbBr_3$ and $MAPbI_3$ planar solar cells (Figure 2.5d). When light illuminates the device, weakly bound electron-hole pairs or free charge carriers are generated in both the $MAPbBr_3$ and $MAPbI_3$ absorber layers. In the $MAPbBr_3$ front cell, electrons move to the blocking (bl-TiO_2) electron conductor, while holes are transported to the poly-3-hexylthiophene or poly- (triaryl amine) (PTAA) HTL. Similarly, in the $MAPbI_3$ back cell, electrons are transferred to the PCBM electron conductor, and holes move to the PEDOT:PSS hole conductor. The PTAA-based tandem configuration exhibited a V_{oc} of 2.25 V, a J_{sc} of 8.3 mA cm^{-2}, an FF of 56%, and a PCE of 10.4%. The following year, Li *et al.*[48] developed PSCs based on the $FA_{0.81}MA_{0.15}PbI_{2.51}Br_{0.45}$ absorber layer using the vacuum flash-assisted solution fabrication technique. During that period, when the record efficiency of similarly sized PSCs was 15.6%, Li *et al.*[48] reported a remarkable efficiency of 20.5% (certified PCE of 19.6%) for devices with an aperture area larger than 1 cm^2. Simultaneously, Bi *et al.*[49] developed a new method to fabricate perovskite films. During the perovskite spin-coating deposition, poly (methyl methacrylate) was introduced in chlorobenzene (CB)/toluene solution, acting as a structural support, which facilitated the nucleation of tiny perovskite crystals and directed their subsequent growth, leading to a more uniform and high-quality film formation. Utilizing this approach, a certified 21.02% PCE was achieved. In 2017, Yang *et al.*[50] studied the impact of defect states on the performance of PSCs with FA-based multiple cations and mixed halide anions. They introduced additional iodide ions during perovskite layer formation, which lowered the number of deep-level defects through an intramolecular exchange process. This

defect-engineering approach resulted in PCEs of 22.1% in small-scale PSCs and 19.7% in 1 cm^2 devices. Rajagopal *et al.*[51] introduced a novel approach to defect passivation in PSCs by implementing a graded heterojunction (GHJ) structure (Figure 2.5e), which they compared with PHJ and BHJ PSCs to evaluate their performance. The incorporation of fluoroalkyl-substituted fullerene in the $CH_3NH_3Pb_{0.5}Sn_{0.5}I_3$ perovskite layer effectively reduced trap states and improved charge carrier recombination resistance. As a result, the GHJ PSCs achieved an average PCE of 15.18% with a V_{oc} of 0.87 V. The devices with PHJ architecture exhibited 11.02% PCE and 0.68 V of V_{oc}. While the BHJ structured devices demonstrated the lowest efficiency, with a PCE of 7.37% and a V_{oc} of 0.57 V. These results underscore the superiority of the GHJ architecture, highlighting its potential for enhanced charge extraction and improved PV performance. In 2018, Yang *et al.*[52] fabricated planar PSCs with an ETL comprising ethylene diamine tetraacetic acid complexed SnO_2. The better Fermi level alignment with perovskite and threefold higher electron mobility than SnO_2 led to a record PCE of 21.60% (certified 21.52%) with negligible hysteresis for planar PSCs, and 18.28% PCE for flexible devices. Meanwhile, the PCE of single-junction PSCs further increased to 23.7%,[53] attaining a high V_{oc} closer to the bandgap by tailoring a high-quality perovskite layer that minimized recombination losses.

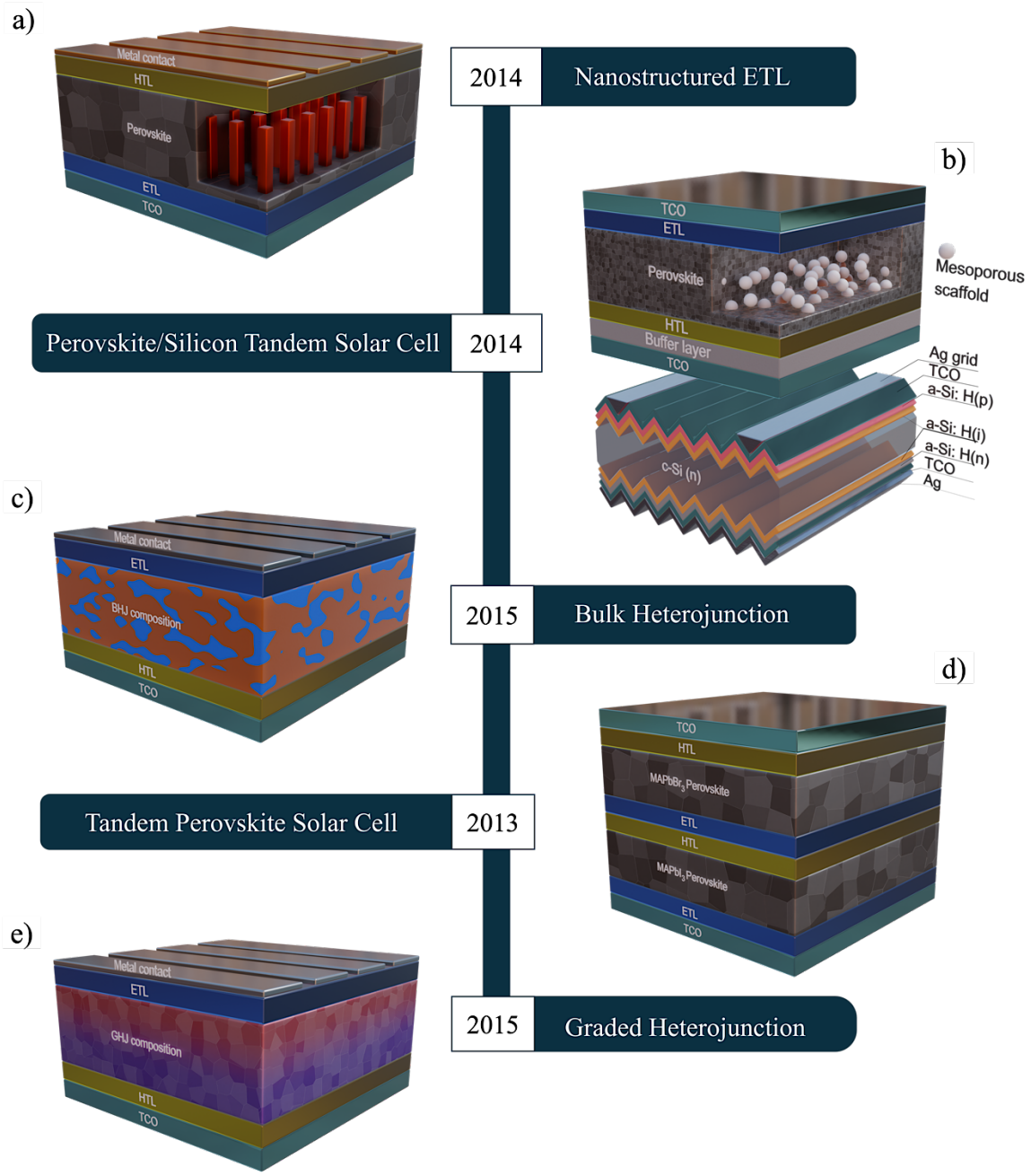

Figure 2.5 Evolution of perovskite-based solar cells. a) Nanostructured TiO_2 ETL. b) perovskite/silicon tandem solar cell. c) BHJ architecture. d) single-junction $MAPbBr_3$ and $MAPbI_3$ planar solar cell. e) GHJ architecture

In 2019, Jiang *et al.*[54] demonstrated the effectiveness of phenethylammonium iodide post-treatment in $FA_{1-x}MA_xPbI_3$-based PSCs, resulting in higher-efficiency planar PSCs with a certified PCE of 23.32% and a V_{oc} of 1.18 V. A record efficiency of 25.2%[8] for single-junction PSCs was achieved in 2019 through a collaboration between the Korea Research Institute of Chemical Technology and the Massachusetts Institute of Technology. In 2020, Jeong *et al.*[55] presented an anion engineering strategy, incorporating the pseudo-halide anion

formate ($HCOO^-$) to suppress anion-vacancy defects at grain boundaries and film surfaces, enhancing perovskite crystallinity. The demonstrated fabricated devices with a PCE of 25.6% and long-term operational stability exceeding 450 h. In 2021, Feng *et al.*[56] reported an advanced vacuum deposition technique designed for large-area device fabrication, successfully depositing perovskite films on 400 cm^2 glass and 300 cm^2 flexible substrates. Considering the temperature sensitivity of PSCs, the authors incorporated a low-temperature annealing process at 60°C, resulting in a PCE of 21.32%, the highest reported result for vacuum-deposited PSCs. A research team at Ulsan National Institute of Science and Technology achieved a record PCE of 25.8%[8] with a V_{oc} of 1.1797 V, a J_{sc} of 25.77 mA cm^{-2}, and an FF of 84.9% in 2022, marking a significant advancement in high-performance perovskite PVs. In 2023, Japan Electrical Safety and Environment Technology Laboratories certified a 26.0%[8] efficiency for a small 0.07 cm^2 PSCs fabricated by the Institute of Semiconductors, Chinese Academy of Sciences. Later, Xu *et al.* from the University of Science and Technology of China achieved a certified 26.1%[8] PCE for inverted PSCs and subsequently enhanced the record to 26.7%[8] PCE in 2024. The rapid efficiency improvements in PSC technology over the past 12 years highlight its disruptive potential in the PV field. The latest world-certified record of 26.95%[8] from the collaboration between Soochow University and the University of New South Wales brings PSCs within 0.35% of Si solar cells. With low-cost fabrication, lightweight and flexible design, and advantageous low-light performance, PSCs present a highly promising complement for scalable and diverse solar energy applications.

2.4 Current Limitations in PSCs

PSCs have significantly progressed in a short period. However, some critical issues must be solved before they can be widely implemented. Key concerns include poor long-term stability, interfacial and perovskite layer defects, difficulties in scaling up to large-area fabrication, and the toxicity of certain constituent materials.

2.4.1 Toxicity

Lead (Pb) played a significant role in advancing PSC technology. While it has been a cornerstone in the rapid rise of PCE over the years, the toxicity of Pb-based materials remains a challenge and poses serious environmental and public health concerns. There are many ways Pb compounds can enter the human body: through ingestion, respiratory tract, and skin contact. Pb primarily targets the central nervous system; owing to its ionic affinity, Pb^{2+} can mimic calcium ions (Ca^{2+}) and cross the blood-brain barrier.[57] After accumulating in neural tissue, Pb can cause oxidative stress and genetic damage. In addition to its neurotoxicity, Pb is gradually deposited in the skeletal system as lead phosphate, where it can persist for decades with a biological half-life of 20–30 years. Long-term exposure to Pb, even at low concentrations of 5 μg dL^{-1}, has been linked to cognitive impairment, motor skill deficiencies, and behavioral issues such as anxiety, depression, and aggression.[57,58] Additionally, evaluating the Pb density in PSCs is important for understanding the possible effects on the environment. The thickness of the perovskite layer in the PHJ device is around 500 nm. Thus, the estimated lead content for $MAPbI_3$, $FAPbI_3$, and $CsPbI_3$ devices is approximately 0.066, 0.067, and 0.077 mg/cm^2, respectively.[15] Nonetheless, commercial Si solar cells contain 0.61 mg/cm^2[15] of lead material in the solder, exhibiting a substantially higher Pb content than PSCs. In addition, to address toxicity in solar cells, the Pb-free alternatives have been investigated by incorporating substitute cations such as germanium,[59] tin,[60] and bismuth.[61]

Solvent engineering is also commonly employed to optimize the formation of uniform perovskite films with enlarged grain sizes. However, typical solvents, such as N, N-dimethylformamide (DMF), dimethyl sulfoxide (DMSO), and γ-butyrolactone pose significant risks to human health and the environment.[62,63] The combination of DMSO and DMF solvents is generally used in the perovskite precursor solution, where DMF offers high solubility for lead iodide (PbI_2), and DMSO functions as a coordinating ligand, forming

stable complexes with Pb^{2+} ions owing to its strong coordination ability.[63] Among the solvents commonly used in the fabrication of PSCs, DMF is the most hazardous, because it can be readily absorbed through the skin or inhaled, posing serious health risks. Continued exposure to DMF can lead to liver toxicity, dermatological irritation, and neurological symptoms such as migraine attacks, distress, and nausea.[64,65] The implementation of environmentally friendly solvents is necessary to reduce the toxicity during the fabrication process, contributing to safer working conditions. Xie *et al.*[66] replaced DMF with green solvent γ-valerolactone in the preparation of quasi-two-dimensional Dion–Jacobson (quasi-2D DJ) PSCs. Remarkably, despite replacing the primary solvent with a green alternative, the fabricated devices demonstrated a record 17.99% PCE for quasi-2D DJ PSCs.

2.4.2 Scalability

Fabricating high-efficiency PSCs requires accurate control of the morphology and crystal structure of the absorber layer. Lab-scale devices with small active areas have achieved PCEs exceeding 25% in controlled environments, but scaling up to large-area modules frequently results in significant performance losses. The current manufacturing technologies, such as spin-coating, are effective for small-scale PSCs; however, their low reproducibility and incompatibility with industrial roll-to-roll processes make them unsuitable for mass production.[67] Thus, successful device scaling and commercialization necessitate further advancements, to ensure consistent film coverage over large areas, material compatibility with various substrate types, and reproducibility. This has prompted research into scalable techniques such as slot-die coating,[68] vapor deposition,[69] and hybrid solvothermal methods that produce uniform single-crystalline titanium dioxide layers. Figure 2.6 demonstrates solution-based fabrication techniques:

a) Spin-coating[70] is the most prevalent method for depositing high-quality, uniform thin films in research and small-scale manufacturing. In this process, a small volume of precursor solution is dropped at the center of a substrate, which is then rotated at a specific

speed. Centrifugal forces drive the liquid outward, producing a smooth and self-leveling film. The film thickness is defined by the spinning rate and solution viscosity.

b) Doctor blade coating[70] represents a highly efficient deposition method suitable for large-area and flexible substrates, and is compatible with high-throughput, continuous manufacturing. First, the precursor solution is distributed on the substrate. Then, the blade coater moves across the surface and spreads the solution to create a wet film, the thickness of which depends on the gap between substrate and blade, the deposition speed, and the coating material characteristics.[71]

c) Screen printing[72] offers a cost-effective, rapid, and adaptable method for depositing films onto nearly any surface. The method employs a mesh screen resembling a stencil into which the desired pattern is inscribed. A precursor solution is poured to the top of the mesh, and a rubber blade, known as a squeegee, is swept across the screen multiple times, forcing the material through the mesh apertures onto the substrate. This technique is primarily used in the deposition of Ag electrodes in c-Si solar cells, where its precision and throughput enable robust contact definition over large areas.[72] Additionally, mp-TiO_2 has been screen-printed to obtain a uniform film in DSSCs.[72]

d) Slot-die coating[73] is a continuous deposition method suitable for large areas and roll-to-roll manufacturing. In this method, a controlled flow of precursor solution is injected through a narrow slit onto a moving substrate, creating a uniform wet film whose thickness can be adjusted by varying the flow rate, substrate speed and slit configuration. The slot-die coating method is efficient, offering maximal material utilization and minimal solution waste compared with spin-coating and screen printing deposition techniques.[73]

e) Inkjet printing is a digitally controlled deposition technique that creates high-resolution patterns up to 1200 dpi.[74] The print head produces tiny droplets of precursor solution and deposits them onto the substrate. This printing method can be classified into three categories: continuous inkjet, drop-on-demand (DOD), and field- or flow-induced tip

streaming techniques.[75] DOD is suitable for the fabrication of solar cells. The working principle[74] includes the formation of each droplet by mechanical compression of the ink through the piezoelectric nozzle or by transiently heating the ink, after which it is electrically charged and directed toward the surface via an applied field. Compared with other deposition techniques, inkjet printing has emerged as a leading solution-processing method for scalable PSC fabrication, mainly owing to its versatility with diverse substrates and solvent chemistries.[76] Additional advantages include high production speed, affordability, and material efficiency.[77]

f) Spray coating enables uniform, large-area deposition of functional thin films on various substrates. A precursor solution is deposited onto a substrate by atomizing it into droplets with an inert carrier gas.[78] The techniques can be categorized based on the atomization method, including thermal spray, plasma jet, flame spray, and arc discharge spray.[78] The resulting wet-film thickness depends on the spray speed, nozzle opening (or piezoelectric head area), ink consistency, and solvent volatility.

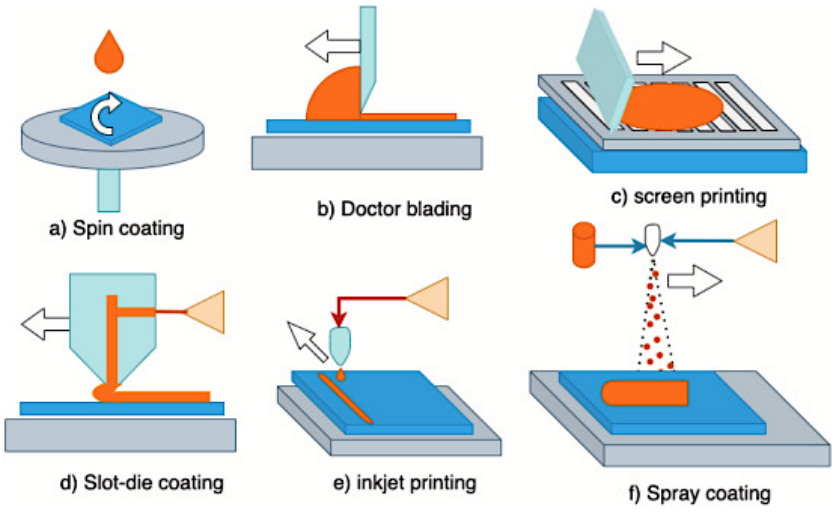

Figure 2.6 The main solution-based deposition techniques used for preparing perovskite absorber layers. Reproduced from Ref.[79] under CC BY 4.0

2.4.3 Factors Affecting the Long-Term Stability of PSCs

The degradation of device performance can be attributed to intrinsic and extrinsic fragility. Intrinsic factors[80] include the chemical and structural vulnerabilities of the perovskite material. Ion migration, thermal decomposition, and phase transitions, especially under

prolonged exposure to high temperature, light, and electric fields, negatively affect the operational stability and PSC performance. For instance, $MAPbI_3$ decomposes under heat stress into its primary components: PbI_2 and MAI.[81] In $CH_3NH_3PbI_3$-based PSCs, decomposition occurs at temperatures between 100 and 140 °C, which further intensifies with increasing temperature.[82] The sensitivity of organic-inorganic perovskites to illumination leads to significant photodegradation. In $MAPbI_3$ illumination with white light initiates a series of chemical reactions, some irreversible, that promote the release of volatile byproducts, including CH_3I, NH_3, and PbI_2, as well as reversible reactions producing MA^+, PbI_2, and HI.[83] In contrast, mixed halide perovskites undergo halide segregation, resulting in the formation of iodine-rich and bromine-rich domains.[84] Although this segregation may be reversible in a controlled environment, it disturbs the crystal lattice, facilitates ion migration, and reduces charge carrier transport efficiency, ultimately compromising the performance and stability of the device.

Extrinsic factors[80] encompass environmental stressors (e.g., moisture, oxygen, and UV light) and device-level imperfections such as interfacial defects and the properties of CTLs. Poor-quality interfaces can introduce energy mismatches and trap states[85], whereas hygroscopic or UV-sensitive CTLs (e.g., Spiro-OMeTAD and TiO_2) may act as pathways for moisture ingress or ion diffusion. These extrinsic vulnerabilities accelerate degradation mechanisms, further reducing device stability and performance.

2.5 Strategies for Enhancing the Stability of PSCs

Given the wide range of intrinsic and extrinsic factors that reduce the stability of PSCs, significant research efforts have been devoted to developing effective mitigation strategies, including compositional engineering, interfacial engineering, and encapsulation techniques.

2.5.1 Compositional Engineering

One key approach is compositional engineering, which focuses on modifying the intrinsic

characteristics of the perovskite material by selecting and substituting A-, B-, or X-site ions.[84] The A-site cation in halide perovskites is critical in determining the stability of PSCs and optoelectronic performance. For instance, MA^+-based perovskites offer strong optoelectronic properties but are limited by thermal instability. To address this, the substitution of MA^+ with FA^+ improves thermal stability and narrows the bandgap. However, this improvement is constrained by the weak structural stability of the black α-phase, which can spontaneously transform into the non-photoactive yellow δ-phase at room temperature which is accelerated by exposure to ambient humidity.[86] The incorporation of small ions (e.g., Cs^+, MA, and Br) contributes to the stabilization of α-phase $FAPbI_3$ and improves thermal and moisture resistance.[86,87] However, such mixed perovskites are susceptible to phase segregation, negatively affecting durability. B-site cations often comprise Pb and Sn components. Pb-based PSCs have high PCEs but raise significant environmental and toxicity concerns. Sn-based perovskites represent an environmentally friendly Pb-free alternative, but their susceptibility to oxidation limits their practical applications.[84] Compositional modification of the X-site anions influences the band gap and phase stability.[83] For instance, partial or full substitution of iodide with bromide or chlorine results in a wider band gap, which is advantageous for use in tandem solar cells.[84] Overall, compositional engineering often involves significant trade-offs, where each modification may enhance specific properties while simultaneously revealing new weaknesses in the material.

2.5.2 Interfacial Engineering

CTLs and interfaces play pivotal roles in determining the performance of solar cells because they directly impact both efficiency and overall device functionality. When the perovskite layer absorbs photons, it generates electron-hole pairs. The interface between the absorber layer and CTL facilitates efficient exciton separation, enabling effective charge extraction and transport within the device. For this reason, interfaces are carefully engineered to suppress charge carrier recombination, enabling electrons and holes to efficiently reach the

ETL and HTL. In addition, careful selection of CTMs is important for enhancing the quality of heterojunction contacts. Interface engineering provides four primary benefits to PSCs.

(I) Defect Passivation

First, interfacial engineering effectively passivates defects at the interfaces between the CTLs and the perovskite absorber. Usually acting as trap states, these interfacial defects include under-coordinated metal sites and oxygen or halide vacancies.[88] Such trap states promote trap-assisted recombination, significantly reducing the efficiency and stability of PSCs. Therefore, interfacial engineering mitigates these recombination pathways by reducing the number and impact of these defects. The thermal and operational stability of devices is also greatly improved by adding passivation layers, which operate as protective barriers and successfully shelter perovskite materials from environmental factors like moisture, oxygen, and UV radiation. Moreover, defect passivation is a promising strategy for effectively enhancing the V_{oc} and J_{sc} parameters. In 2023, Sun *et al.*[89] studied the effect of choline chloride (CHCl) passivation on Pb^{2+} ion defects at the buried interface of the absorber layer. The CHCl-modified device achieved a V_{oc} of 1.121 V, J_{sc} of 24.18 mA cm^{-2}, FF of 81.53%, and PCE of 22.10%. In comparison, the reference device exhibited lower performance, with a V_{oc} of 1.088 V, J_{sc} of 23.51 mA cm^{-2}, FF of 78.35%, and PCE of 20.04%.

Self-assembled monolayers (SAMs) serve as effective passivation layers, enhancing device stability and performance. SAMs are organic molecules that spontaneously organize into ordered, uniform monolayers on substrate surfaces.[90] This self-assembly provides a controllable interface between the perovskite absorber and adjacent functional layers, enabling optimized interfacial properties and reduced interfacial defects. Dai *et al.*[91] incorporated an iodine-terminated SAM at the interface between the absorber layer and ETL. This treatment resulted in a 50% increase in interfacial adhesion toughness, significantly improving the mechanical reliability of the device. Moreover, the treatment increased the PCE from 20.2% to 21.4% by efficiently reducing hysteresis. SAMs are also widely used for tandem PSCs. Al-Ashouri *et al.*[92] introduced SAMs in monolithic CIGSe/perovskite

architecture, reaching 23.26% PCE. This approach demonstrated a cost-effective strategy for fabricating all-thin-film tandem solar cells.

(II) Energy Level Alignment

Second, interface optimization is key in aligning the energy levels at the CTL/absorber layer interface to enable efficient charge extraction and transfer. When the interfacial energy barrier exceeds 0.1 eV, it hinders carrier extraction.[93] Furthermore, the barrier can lead to charge accumulation at the interface, thereby increasing recombination losses. Proper interface modification ensures favorable band alignment, thereby facilitating smooth charge transport across the CTL/perovskite junction and improving overall device performance. For example, Lee *et al.*[94] applied interfacial engineering to improve the band alignment of the ETL/perovskite layer interface. The authors deposited dual-coated SnO_2 on the mixed halide perovskite, decreasing the band gap from 4.38 eV (single-coated SnO_2) to 4.03 eV. Furthermore, the device with dual-coated ETL demonstrated an increased PCE from 18.07% to 19.23%.

Ionic liquids (ILs) are characterized by high optical transparency and excellent electron mobility. Yang *et al.*[95] incorporated an IL on the ETL surface through spin-coating, adjusting the WF of TiO_2 from 4.26 to 4.01 eV. Meanwhile, Xiao *et al.*[96] introduced hydrophobic metal-organic frameworks (MOFs) as interfacial layers between the absorber and HTL layers. Rich in carboxylic groups, the tailored MOFs effectively passivated interfacial defects, suppressed non-radiative recombination, and improved energy level alignment for efficient carrier transport. As a result, CsFAMA-based PSCs (1.63 eV) reached a PCE of 23.06%, whereas FA-based PSCs (1.55 eV) achieved 24.81% with an outstanding FF of 84.3% and minimal voltage loss (0.386 V).

(III) Enhanced Quality of Perovskite Film

Third, interfacial engineering improves the morphological quality of the perovskite film. Introducing a buffer layer enhances the surface wettability of the CTM, resulting in more uniform, dense perovskite films with fewer defects.[93] Wang *et al.*[97] incorporated a sodium

dodecyl benzene sulfonate (SDBS) film between the absorber and NiO_x HTL, confirming a positive impact on the surface wettability. Additionally, they demonstrated the formation of uniform, fully covered perovskite films with enhanced crystallinity and enlarged grain sizes. SDBS-passivated devices reached a champion PCE of 20.15% and V_{oc} of 1.124 V. In another paper, Han *et al.*[98] passivated a ZnO ETL using SAMs and effectively regulated the wettability of the perovskite precursor solution on the ETL, leading to improved crystallinity of the perovskite film. The reference sample demonstrated a 135 nm average perovskite grain size. In contrast, the SAM-passivated sample demonstrated a significantly larger particle size of approximately 180 nm.

2.5.3 Encapsulation Techniques

Encapsulation is used to protect PSCs from environmental degradation caused by humidity, oxygen, and light exposure. The following approaches are the most commonly employed for encapsulating PSCs:

(I) Thin-film Encapsulation[99]

This approach involves depositing ultra-thin protective layers directly onto the PSC surface to form an effective barrier against environmental deterioration. Standard deposition methods are outlined here.

- ***Atomic Layer Deposition (ALD):*** Highly dense and pinhole-free encapsulation layers can be fabricated by accurately regulating the film thickness and homogeneity.[99] Al_2O_3 is the most commonly used encapsulation material.[99,100]
- ***Chemical Vapor Deposition:*** Conformal coatings can be deposited on complex and irregular surfaces, presenting a promising approach for encapsulating flexible PSCs. Silicon nitride (Si_3N_4) and silicon dioxide (SiO_2) are widely applied.
- ***Solution-processed Thin Films:*** Solution processing offers a cost-effective encapsulation approach, where barrier layers are deposited from solution-based precursors using spin-coating or printing methods.[101]

(II) Edge Encapsulation[84,102]

Although thin-film encapsulation effectively protects the top surface of PSCs, the device edges often remain exposed to environmental contaminants. For this reason, edge-sealing techniques have been developed to prevent moisture and oxygen ingress from the sides, which can significantly compromise device stability.

- ***UV-curable Epoxies:***[84,103] These materials are applied along the edges of the device and cured under UV light to form a robust and moisture-resistant seal.
- ***Glass Frit Sealing:***[84,104] The device edges are coated by a glass frit paste, which is then melted through thermal processing to form a hermetic seal. Although this encapsulation method provides an effective barrier, high processing temperatures make it less suitable for flexible substrates.
- ***Laser Sealing:***[84] Localized laser energy is used to melt and bond sealing materials at the device edges with high precision. This method enables fine control over sealing dimensions and is suitable for both rigid and flexible substrates, making it a versatile choice for modern PSC designs.

(III) Other Encapsulation Strategies

- ***Monolithic Encapsulation:***[84] Fabrication complexity is reduced by integrating the encapsulating layer into the device architecture during the fabrication process. Thus, the encapsulation does not involve additional steps.
- ***Thin Glass Encapsulation:***[99,100,102] Thin glass sheets are used to create a barrier against environmental stresses. Glass is considered an efficient and industrially attractive encapsulation material because it is easy to clean. However, the device edges may remain partially vulnerable because imperfect sealing can allow moisture ingress.[100]
- ***Barrier Films and Desiccants:***[84] Incorporating both barrier films and desiccants into the encapsulation package provides an effective strategy to protect PSCs from moisture. Barrier films prevent external moisture from entering the device, while the desiccants absorb any remaining humidity that may still penetrate, offering an added layer of

protection.

- ***Grain Encapsulation:***[101] Polystyrene-co-polyacrylonitrile is employed as an effective polymer-based encapsulation material to coat perovskite grain boundaries. Encapsulated $MAPbI_3$ devices demonstrated high stability and maintained 95% of their initial efficiency after 24 h of aging at 100°C.[105]

CHAPTER 3: METHODOLOGY AND CHARACTERIZATION TECHNIQUES

3.1 Materials

FTO-coated glass substrates (2 × 2 cm) were supplied by OPV Tech, China. Methylammonium chloride (MACl, ≥ 99%) was purchased from Merck, Germany. Zinc oxide ink solution (ZnO ink, 2.8%) was purchased from Infinity PV, Denmark. Acetone (≥ 99.5%, ACS grade), PCBM, and Spiro-OMeTAD (> 99.5%) were supplied by Lumtec, Taiwan. Glacial acetic acid was supplied from Fisher Scientific, USA. Special Cleaning Concentrate Hellmanex™ III, tin (IV) chloride pentahydrate ($SnCl_4 \cdot 5H_2O$, 98%), sodium bromide (NaBr), 2-methoxyethanol ($CH_3OCH_2CH_2OH$, 99.3%), magnesium acetate tetrahydrate ($(CH_3COO)_2Mg \cdot 4H_2O$, 99%), ethanolamine (ETA, 99%), tin (II) chloride dehydrate ($SnCl_2 \cdot 2H_2O$, ≥ 99.995%), cesium iodide (CsI, 99.9%), lead (II) iodide (PbI_2, 99.999%), lead (II) bromide ($PbBr_2$, 99.999%), potassium iodide (KI), 4-tert butylpyridine (TBP, 98%), bis(trifluoromethane)sulfonimide lithium salt (Li-TFSI, 99.95%), CB (99.8%, anhydrous), isopropanol (IPA, 99.5%, anhydrous), DMSO (99.9%), and DMF (99.8%), were purchased from Sigma Aldrich, USA. Formamidinium iodide (FAI), methylammonium bromide (MABr) were purchased from Greatcell Solar Materials, Australia. Silver conductive paint was supplied by Electrolube, UK. SnO_2 colloidal dispersion (15 wt% in H_2O) was purchased from Alfa Aesar, UK.

3.2 Device Fabrication

The device fabrication procedures are highly tailored to each experiment. Differences in material choice, layer structure, and device architecture require specific processing conditions, including deposition, thermal treatment, and interface engineering variations. Given that this thesis focuses on the interface between the ETL and the perovskite layer, the HTL deposition procedure was kept consistent across all experiments. The cleaning process was also standardized to ensure a reproducible and contaminant-free initial surface. The

detailed experimental protocols for the PSC structures investigated in this work are presented in Chapters 4 and 5.

3.2.1 Cleaning Procedure

The substrate cleaning procedure is the first step in device fabrication. FTO-coated glass substrates were gently wiped with a disposable wiper soaked in IPA, followed by drying under a nitrogen stream. Subsequently, the substrates were immersed in a detergent solution consisting of 2 vol% Hellmanex III diluted in deionized (DI) water and sonicated in an ultrasonic bath for 15 min. Following this, the substrates were periodically immersed in fresh DI water baths, followed by sequential ultrasonic cleaning in acetone and then in IPA solution, each for 15 min. This acetone/IPA cycle was repeated once more time to ensure the complete removal of organic and particulate contaminants. The cleaned substrates were dried with nitrogen and sent to the UV-ozone cleaning system for 30 min to remove residual surface impurities and enhance wettability.

3.2.2 HTL Deposition

The preparation of the HTL precursor solution involved two main steps. First, 80 mg of Spiro-OMeTAD was dissolved in 1 mL of CB and stirred for 10 min. Subsequently, 29 μL of TBP and 18 μL of Li-TFSI were added to the solution, followed by an additional 10 min of mixing. The HTL was deposited on a perovskite film by spin-coating at 3000 rpm for 30 s.

3.2.3 Au Contact Evaporation

Gold electrodes were deposited using a Kurt J. Lesker thermal-evaporation system with a base pressure of 1×10^{-7} Torr. Substrates were mounted on a rotating stage and masked to define active areas of 0.06 cm^2. Deposition continued until a nominal thickness of 70 nm was reached.

3.3 Material Deposition Equipment

During sputter deposition atoms or molecules are ejected from a solid target and subsequently transported through a low-pressure gas and condensed onto a substrate. Sputtering was performed using a Kurt J. Lesker magnetron sputterer, Germany (Figure 3.1). The operating principle involves applying a high voltage across two disks: a negatively biased target (cathode) and a substrate (anode), separated by a few centimeters.[106] An inert gas is introduced at pressures ranging from 1 to 100 mTorr between the electrodes[106]. Electrons liberated from the target surface initiate a cascade ionization in the gas, creating a dense plasma of electrons and positive ions. The plasma remains electrically neutral and conducts electricity well, resulting in a minimal voltage drop across it. The voltage drop occurs across the narrow "dark space" areas between the plasma and each electrode.[106] The negatively charged target draws positive ions from the plasma boundary, causing them to collide with the target with enough energy to dislodge neutral atoms or molecules through energy transfer. As atoms are ejected from the target toward the substrate, they collide with many gas atoms or molecules that redirect them and result in a loss of energy.[106] By calibrating the distance between the target and substrate, the atoms arrive at the substrate surface from randomized angles, leading to a consistent film thickness over a nonplanar surface.[106]

In this work, an SnO_2 thin film was sputtered using a 99.99 % pure SnO_2 ceramic target. The deposition procedure was conducted in a pure argon atmosphere at a working pressure of 5×10^{-3} Torr, reaching uniform film thicknesses of approximately 10 nm.

Figure 3.1 Magnetron sputtering instrument

Thermal evaporation is an established and cost-effective technique for applying high-quality thin films in a vacuum environment. Common materials like aluminum, nickel, tin, iron, silver, gold, and platinum are often evaporated using this method.[107] In this work, gold contacts were deposited using a Kurt J. Lesker thermal evaporator, Germany (Figure 3.2).

Evaporation begins when the source material atoms or molecules acquire sufficient kinetic energy to break their intermolecular bonds and enter the vapor phase. Elevating the material temperature raises its vapor pressure, which increases the evaporation rate. The chamber is evacuated to high vacuum (approximately 10^{-6} Torr) using a turbomolecular pump supported by an oil-sealed roughing pump.[108] Sample loading and unloading are performed manually, while material deposition can be conducted in either automatic or manual mode.

Figure 3.2 Thermal evaporator

3.4 General Characterization Techniques

Characterization methods for PSCs are categorized based on the properties they are designed to evaluate. Employing a combination of various techniques provides a comprehensive understanding of how material properties and interface quality influence the efficiency and stability of PSCs.

3.4.1 Morphological and Topographical Characterization

Prior to morphological analysis, sputter coating of the samples is required to improve surface conductivity and prevent charging during imaging. The Q150T Plus sputter coater (Figure 3.3) is optimized for use with a turbomolecular pump and achieves a low vacuum level down to 5×10^{-5} mbar. This high-vacuum environment enables the uniform deposition of oxidizable metals with small grain sizes, which is ideal for high-resolution imaging.

The working process[109] of the sputter coater starts by leaking argon into the chamber. When a high voltage is applied between the target (cathode) and the chamber walls (anode), the argon gas is ionized, generating a plasma composed of positively charged argon ions (Ar^+) and electrons. Ar^+ ions are accelerated toward the magnetron head with the target material. After striking the target, Ar^+ ions transfer energy and physically dislodge atoms from the target surface, which is referred to as the sputtering process. The ejected target atoms travel through the vacuum and deposit as a thin, conductive coating onto the surface of the sample.

In this work, ETL-coated and perovskite-coated substrates were coated with 4 nm of gold. The sputter coater equipment is supplied by Quorum, UK.

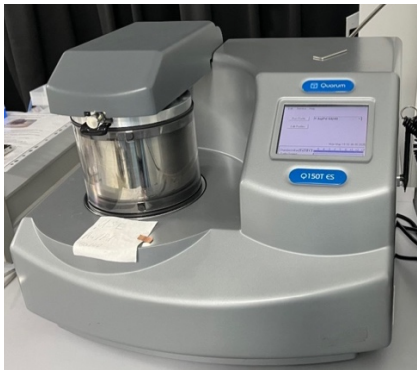

Figure 3.3 Q150T Plus sputter coater

Scanning electron microscopy (SEM) provides high-resolution images of sample surfaces, including top-view and cross-sectional images. A Zeiss SEM Crossbeam 540 instrument (Figure 3.4a) was used for evaluating morphology, uniformity, and crystallite size. The equipment was purchased from Zeiss, Germany.

SEM relies on a series of precisely coordinated components [110] as illustrated in Figure 3.4b. A thermionic emission gun generates electrons by heating the tungsten filament. When the thermal energy overcomes the WF of the source material, electrons are released and accelerated down the column. The electron column operates under a high vacuum to avoid interacting with air molecules, preventing electron source contamination and enabling precise electron manipulation. The positively charged anode generates an electric field that draws in and speeds up the released electrons. The SEM instrument focuses the beam using multiple electromagnetic lenses.

- ***Condenser Lens****:* This lens narrows the electron beam and controls its current and diameter, effectively determining how small the beam spot is when it hits the sample.
- ***Objective Lens****:* This lens focuses the electron beam onto the sample surface with high precision. It also helps determine the depth of field and working distance. The tighter the focus, the sharper the image.

Before reaching the sample surface, the beam travels through scan coils in a raster pattern and moves across the entire sample area, creating a whole image. Finally, when the focused electron beam hits the surface of a sample, it interacts with the sample atoms,

penetrating only a few nanometers. As a result, different signals are released:

- ***Secondary Electrons**:* Low-energy electrons (less than 50 eV) are ejected from the top surface of the material. Because they originate very close to the surface, they provide high-resolution information about the surface topography.
- ***Backscattered Electrons***: Higher-energy electrons give information about the composition, where heavier elements appear brighter on the image
- ***Characteristic X-rays**:* These signals are used in techniques like energy-dispersive spectroscopy (EDS) integrated within the SEM system to assess material purity, determine the sample elemental composition, and detect the presence of contaminants.

a) b)

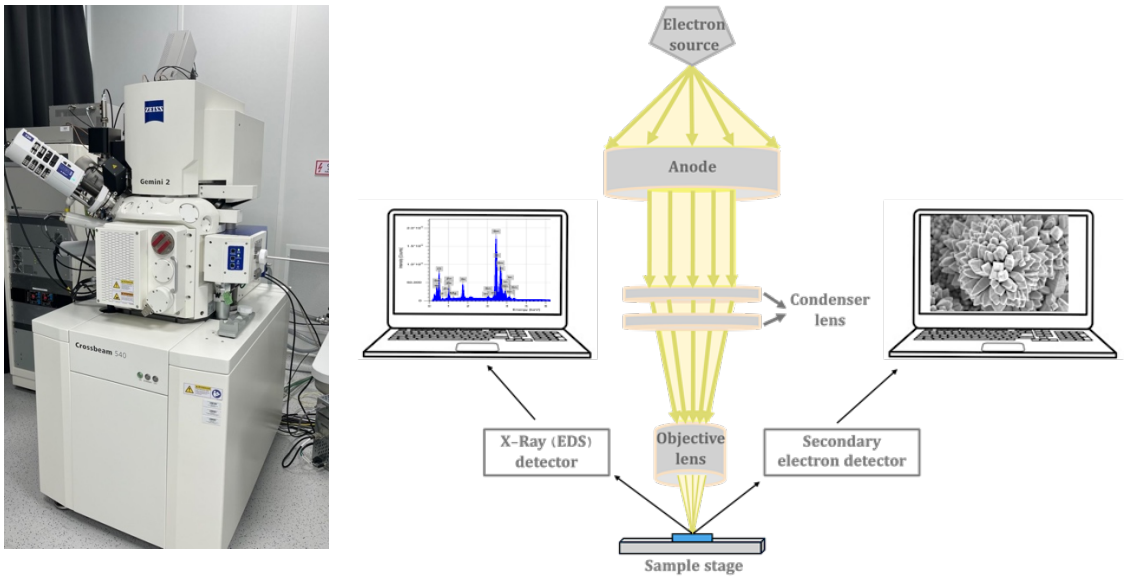

Figure 3.4 a) SEM Crossbeam 540, b) illustration of the SEM working principle

Scanning probe microscopy[111] (SPM) is employed for various types of high-resolution surface analyses. The SmartSPM-1000 instrument and integrated software support standard techniques, such as atomic force microscopy (AFM), and an extensive suite of advanced modes. The instrument was purchased from Advanced Integrated Scanning Tools for Nano-Technology, USA.

The equipment includes two main components:[111] a base and a measuring head. The base consists of a scanner, sample holder, tip-to-sample approach mechanism, and a sample

positioning stage. Figure 3.5a illustrates the working principle. The measuring head comprises a cantilever probe holder, a laser for beam deflection detection, and a photodiode to capture the reflected laser signal. It operates by bringing a sharp probe tip close to the sample surface and measuring interactions between the tip and surface to extract structural, electrical, and mechanical information. The vertical and lateral movement of the AFM tip during surface scanning is detected using a laser beam reflected from the cantilever.[112] This reflected beam is directed onto a position-sensitive photodetector, which precisely monitors the tip deflection in both axes.

There are three main modes of AFM: contact, non-contact, and tapping (Figure 3.5b).

- ***Contact Mode:***[113] The probe tip remains in continuous contact with the sample surface during the scanning process. When the scanner moves the tip across the sample surface, changes in height result in the cantilever deflecting due to contact forces. Feedback adjusts the vertical position of the tip to maintain constant deflection. This movement is recorded to create a topographic image of the surface. Contact mode is ideal for hard materials but can damage soft or delicate samples.
- ***Non-contact Mode:***[113] A stiff cantilever is vibrated close to its resonant frequency from 100 to 400 kHz, with oscillation amplitudes ranging from several tens to hundreds of angstroms.[114] Thus, the tip remains a short distance above the sample surface and does not physically touch it. Instead, it detects the attractive van der Waals forces. The surface topography is mapped by tracking variations in the cantilever resonance frequency or vibration amplitude. This mode is especially useful for imaging materials that are soft, delicate, or loosely bound because it lowers the chance of surface damage by minimizing tip-sample interaction.
- ***Tapping Mode:***[113] The cantilever vibrates at or near its resonant frequency, making brief contact of the tip with the surface of the sample. When the tip gently taps against the surface, fluctuations in oscillation amplitude are observed in relation to the changes in surface topography. This mode reduces the harmful lateral forces present in contact mode

while providing enhanced sensitivity compared with non-contact mode, making it suitable for irregular or fragile samples.

In this work, AFM tapping mode was used to measure ETL- and perovskite-coated substrates, with a scan area of 5 μm × 5 μm. Figure 3.5c shows the AFM instrument employed in the measurements.

Surface potential measurements were performed using The NanoWizard® 4 XP AFM equipment, integrating high-speed scanning capabilities (up to 150 lines/s) with atomic resolution and an extensive scanning range of 100 μm, all within a single versatile system. Kelvin probe force microscopy (KPFM) measures the local surface potential by detecting electrostatic forces between a conductive AFM tip and the sample. The probe tip oscillates above the surface, similar to the AFM tapping mode. The operating principle of KPFM exploits Fermi-level equilibration: when tip and sample with different WFs make electrical contact, electrons flow until their Fermi energies align, establishing the contact potential difference (CPD) that KPFM measures.[115] An alternating current (AC) voltage is introduced between the tip and sample, generating an oscillating electrostatic force proportional to the CPD. A direct current (DC) bias is continuously adjusted through a feedback loop to cancel out the electrostatic oscillation and make the applied DC bias equal to the CPD:[115]

$$V_{CPD} = \frac{\phi_{sample} - \phi_{tip}}{e} \tag{3.1}$$

where ϕ_{sample} and ϕ_{tip} are the WFs of the sample and the tip with the elemental charge e. The KPFM measurements were performed using a scan area of 3 μm × 3 μm. Bruker Corporation, Germany, supplied the JPK Nanowizard 4XP AFM equipment (Figure 3.5d).

a) b)

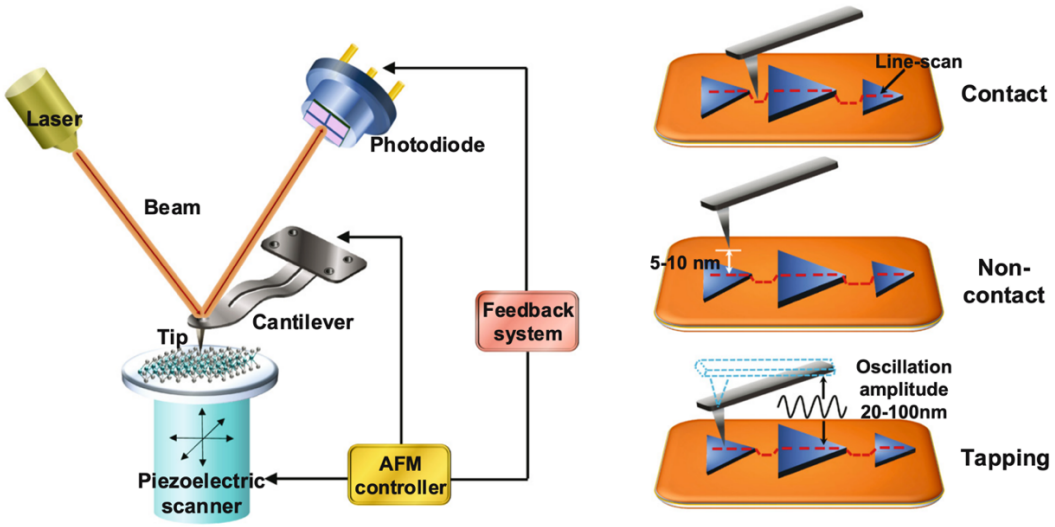

c) d)

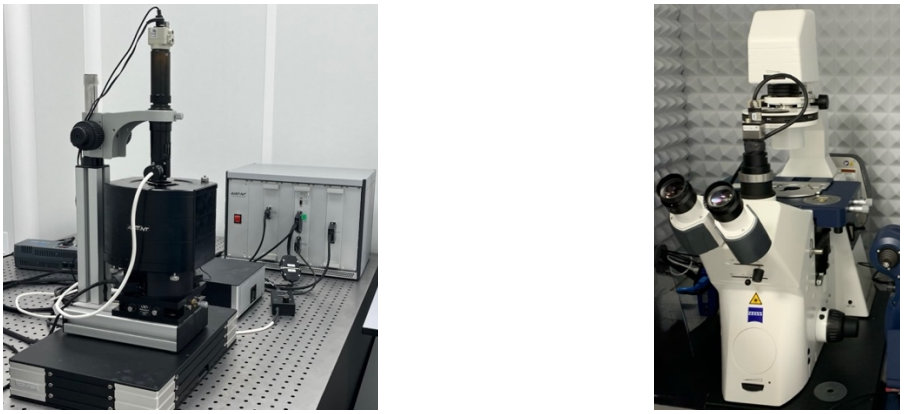

Figure 3.5 a) Schematic of the AFM operating mechanism; reproduced from Ref.[113] under CC BY 4.0. b) Common AFM modes; reproduced from Ref.[113] under CC BY 4.0. c) SmartSPM-1000. d) JPK Nanowizard 4XP AFM

3.4.2 Optical Characterization

The PerkinElmer LAMBDA 1050+ spectrophotometer[116] (Figure 3.6a) is a high-performance analytical instrument designed for precise optical characterization across various sample types. This equipment measures the intensity, transmittance, absorbance, and reflectance of a sample based on the wavelength of the incident light. For this work, transmittance and absorbance were measured. The fraction of light that passes through a sample is defined as transmission T[117] and can be defined as the ratio of the transmitted intensity to the incident intensity:[117]

$$\%T = \frac{I_T}{I_0} \times 100\% \tag{3.2}$$

where I_T indicates the transmitted intensity, and I_0 is the incident intensity.

Absorbance is a scaled transmission ratio that quantifies how much light a sample absorbs:[117]

$$A = -log_{10}\left(\frac{I_T}{I_0}\right) \tag{3.3}$$

If all the light is completely transmitted, $I_T = I_0$, then $A = 0$ indicates no absorption. Thus, if $I_T < I_0$, $A > 0$, where higher values of A correspond to greater absorption.

The measurement principle of a spectrophotometer is based on a continuous comparison of the intensities of two light beams, one of which is a reference while the other passes through the sample. The relation of these intensities results in the transmission %T as a function of wavelength, from which the absorbance can be derived, as described above.

The instrument can perform spectral measurements from 175 to 3300 nm.[116] Figure 3.6b illustrates of the optical pathway. To produce the light of these wavelengths, two lamps are used: a deuterium lamp (D_2) that emits light from 185 to 400 nm, covering the UV range, and a tungsten lamp (W) for the visible light (VIS) and near-infrared (NIR) region of the spectrum.[117] The light source selector allows switching between these lamps in the range from 300 to 350 nm.[118] The incoming light goes through a pair of monochromators and a slit assembly. The monochromators with holographic gratings filter the small-bandwidth light, and the programmatically adjustable slit assembly allows a resolution of at least 0.05 nm in the UV/VIS region and 0.20 nm in the NIR region of the spectrum.[119] The higher resolution in the UV/VIS region is possible owing to the four times higher number of lines per millimeter in the gratings of the UV/VIS monochromators.

Then, the light beam is masked by the common beam mask (CBM) to a spot size from 0 to 10.9 mm and depolarized through the common beam depolarizer (CBD).[120] Next, the chopper, a rotating disk with a mirror and a window, separates the light beam into the reference and sample beams.[120] Finally, the two beams go through the spectrophotometer sample compartment, where polarizing/depolarizing crystals are controlled by a drive

assembly just in front of the sample. The detector compartment is the final receiving part of the device, where different detectors can be installed.

This work used a Photo Multiplier Tube detector for the spectral range from 300 to 850 nm. Perkin Elmer, USA, supplied the spectrophotometer.

a) b)

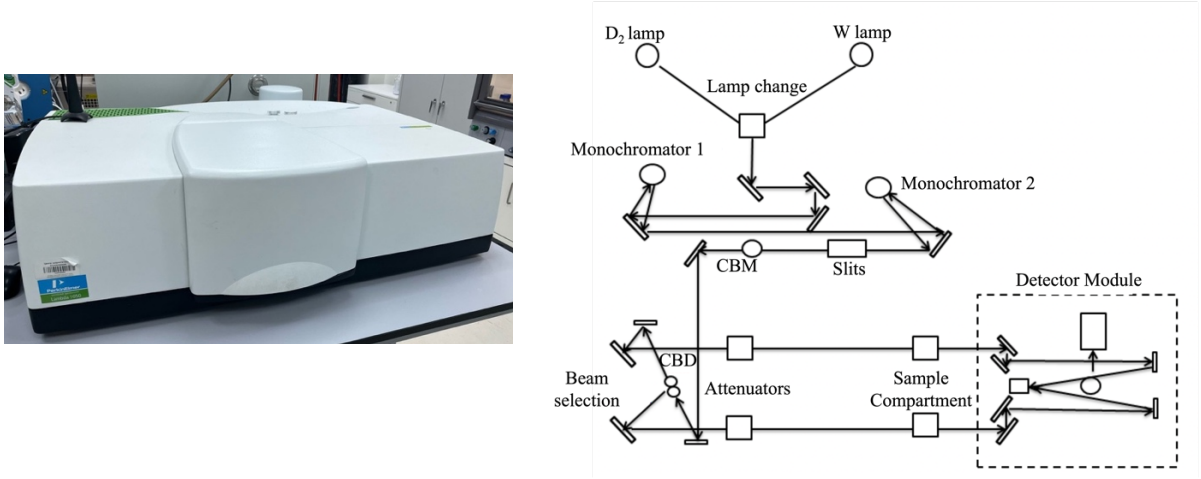

Figure 3.6 UV/VIS/NIR spectrophotometer. b) Schematic illustration of the optical beam pathway; adapted from Ref[121] with permission (Order №: 6032661500192)

The fluorescence images were obtained using a ZEISS LSM 780 confocal laser scanning microscope (Figure 3.7a) to enable spectrally selective fluorescence analysis. Figure 3.7b shows the working principle[122] of confocal microscopy. A semiconductor laser generates the excitation light, which is first collimated by a lens and then directed by a dichroic mirror into a 2D galvanometer scanner for raster scanning.[122] A pair of relay lenses expands the beam to maximize the numerical aperture of the objective before focusing it onto the sample, which is placed on a motorized XYZ stage. The emitted fluorescence travels back along the same optical path; it passes through the objective again, transmitting through the dichroic mirror, focused by a converging lens. A fast-switching filter wheel, fitted with an 840 nm band-pass filter for NIR-I or a 900 nm long-pass filter for NIR-II, selects the appropriate spectral band, while a 100 µm confocal pinhole eliminates out-of-focus light.[122] Finally, the filtered fluorescence is transmitted through an optical fiber to the detector. The collected pixel data is compiled to create an image depicting an optical section of the sample,

delivering high contrast and fine spatial resolution across all three axes (X, Y, and Z).[123] The advantage of this equipment is its ability to generate a 3D image by collecting multiple images from the measured sample. The equipment was purchased from Zeiss, Germany. The experiments were performed using excitation at 405 nm from a diode laser (30 mW) and at 633 nm from a He–Ne laser (5 mW). Fluorescence signals were collected in two detection channels with spectral windows of 410–550 nm (Channel 1) and 644–759 nm (Channel 2), respectively, using photomultiplier tube detectors.

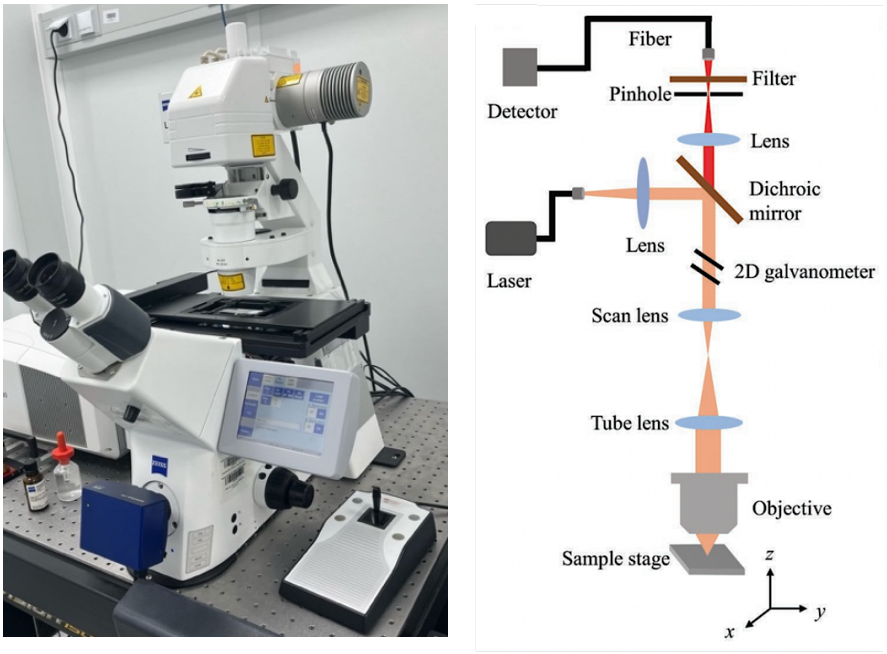

Figure 3.7 a) Confocal laser scanning microscope. b) Illustration of the working principle; reproduced from Ref.[122] under CC BY 4.0

3.4.3 Material characterization

X-ray diffraction (XRD) peaks were acquired using a Rigaku SmartLab® XRD system (Figure 3.8a). XRD is a non-destructive characterization method widely used for quantitatively analyzing crystalline phases in various materials: powders, solid crystals, and liquids. Figure 3.8b illustrates the working principle of the equipment.

The XRD instrument includes three main components: an X-ray tube, a sample holder, and an X-ray detector.[124] X-rays are generated in a cathode ray tube with a 9 kW rotating anode, typically using a Cu target. The resulting CuKα radiation (wavelength of 1.5418 Å) is then filtered using monochromators to produce the monochromatic X-rays

required for diffraction, minimizing fluorescence, and improving signal quality.[124] Next, X-ray beams strike the sample inside the sample holder and scatter off the atoms in the sample's crystalline structure. This produces diffracted ray intensities recorded by the detector that rotates around the sample and scans a 2θ range, producing a diffractogram with diffraction peaks at specific angles (2θ). The occurrence of these diffraction peaks can be explained by Bragg's Law:[125]

$$n\lambda = 2dsin\theta \tag{3.4}$$

where n represents an integer, λ denotes the characteristic wavelength of the X-rays striking the crystalline sample, d indicates the distance between atomic planes, and θ is the angle between the incoming X-ray beam and the crystal atomic planes.[125]

Upon satisfying Bragg's equation, the X-rays reflected by the atoms situated in the plane of a structured material are in phase, producing a diffraction beam at the angle θ.[124] A collection of diffracted intensities is generated along with the angles at which they are detected. The obtained X-ray peaks are considered a chemical fingerprint, enabling chemical identification through comparison with standard reference patterns available in the International Centre for Diffraction Data[126] powder diffraction files.

In this work, ETL- and perovskite-coated substrates were measured in the 2θ ranges of 25° to 70° and 10° to 70°, respectively. The XRD system was purchased from Rigaku Holdings Corporation, Japan.

a) b)

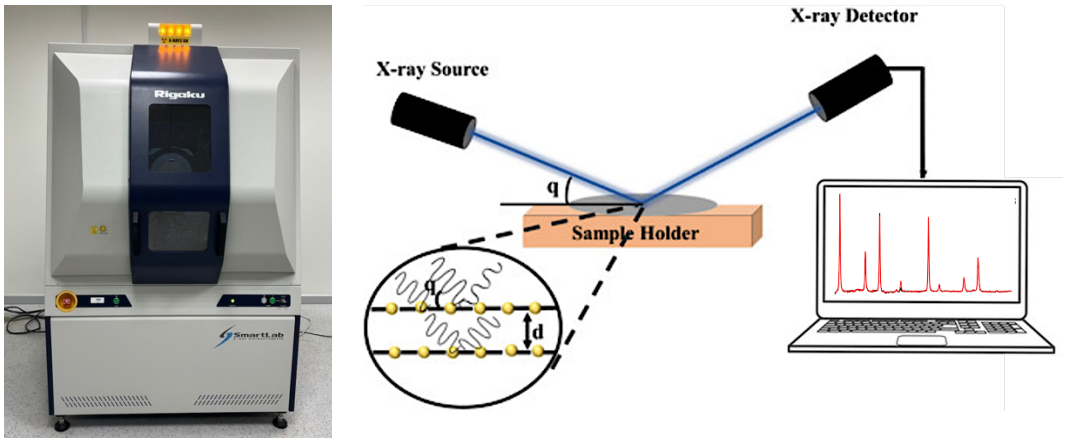

Figure 3.8 a) XRD system. b) Illustration of the XRD operation; adapted from Ref[127] with

permission (Order №: 6034850191379)

3.4.4 Surface Chemical and Electronic Characterization

X-ray photoelectron spectroscopy (XPS) (Figure 3.9a) is a surface-sensitive analytical technique for investigating a material's chemical composition and electronic structure. XPS spectra are acquired by irradiating a solid surface with a focused beam of X-rays and detecting the kinetic energy of electrons emitted from the top 1–10 nm of the material.

The work principle of XPS is based on the photoelectric effect that occurs after exposing a sample to a beam of soft X-rays.[128] The X-rays of known energy penetrate the sample surface and excite core-level electrons in the surface atoms, and the electrons are ejected if the photon energy exceeds the electron binding energy (BE) (Figure 3.9b).[129] The emitted photoelectrons are collected and directed into an electron energy analyzer, which precisely measures their kinetic energy. The corresponding BE of each electron is then determined using the photoelectric equation:[129]

$$\text{BE} = \text{Photon Energy (known)} - \text{Kinetic Energy (measured)} \quad (3.5)$$

The analyzer counts the number of photoelectrons as a function of their BE, producing a spectrum, where peaks appear from atoms emitting electrons of a particular characteristic energy.[128] The intensities of these peaks can be used to identify and quantify all elements (except hydrogen) near the surface of the sample.[128] Additionally, because the BE also characterizes the chemical environment of the parent atom, XPS enables quantification of the chemical composition.

As photoelectrons escape from the solid sample, they may undergo inelastic scattering events that reduce their characteristic kinetic energy. This limits the effective sampling depth of XPS to approximately 10 nm, making it a surface-sensitive technique.[128] Despite this shallow probing depth, XPS remains highly effective, given that the most chemically relevant interactions, such as oxidation, adsorption, and surface modification, typically occur within the top few nanometers of a material surface. The XPS equipment was purchased from Thermo Fisher Scientific, USA.

UV photoelectron spectroscopy (UPS) operates based on XPS principles. The main difference is that UPS uses ionizing radiation with energies in the range of tens of eV to induce the photoelectric effect, whereas XPS uses higher-energy photons, exceeding 1 keV.[130] In research laboratories, a helium discharge lamp usually generates UV photons at energies of 21.2 eV (He I) and 40.8 eV (He II).[130] In our experiments, a He I lamp was used.

a) b)

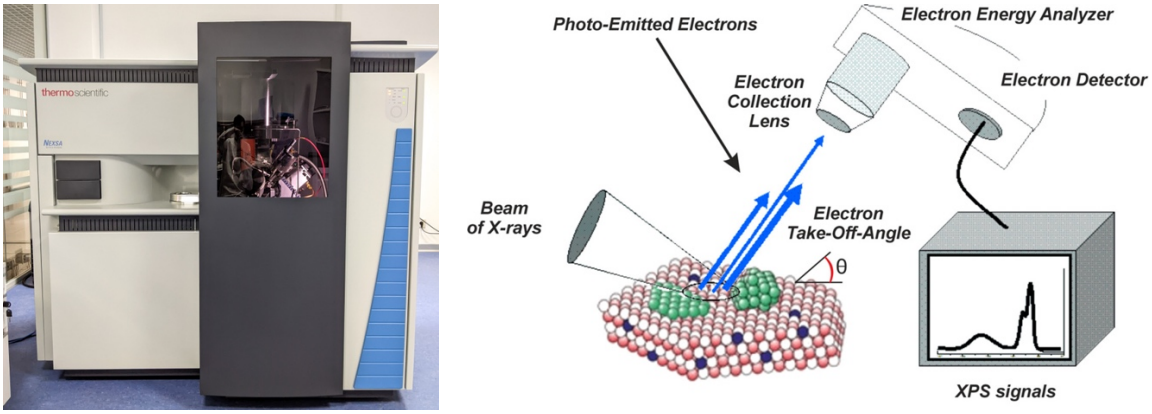

Figure 3.9 a) XPS system. b) Illustration of the photoemission process in XPS; adapted from Ref.[131] under CC BY 4.0

3.4.5 Device Performance Characterization

An Oriel Sol3A solar simulator (Figure 3.10a) was used to measure the device performance of PSCs under air mass (AM) 1.5G standard illumination conditions. The solar simulator was supplied by Newport Corporation, USA.

Figure 3.10b demonstrates the working principle of the instrument. The xenon arc lamp mounted within an ellipsoidal reflector is designed to capture and redirect most of the lamp output into a tightly focused beam.[132] After reflecting from a mirror, the beam passes through an optical integrator. This monolithic integrator, which is precisely aligned with the lamp optics, ensures that beam homogenization keeps spatial non-uniformities below 2%[132], meeting the standards for PV testing. Further along, the beam passes through an AM spectral-correction filter, adjusting the simulator spectrum to achieve a conformity of 0.7%–1.25% with the target standard. Newport Corporation supplies a variety of filters to support various testing conditions.[132] Then, the mirror redirects the optical path to the collimating lens, which

converts the homogenized light into an aligned (collimated) beam, with all the rays oriented parallel to each other.

The AM quantifies the optical path length that sunlight passes through Earth's atmosphere, adjusted to the length at the zenith. The AM is described by the following equation:[133]

$$AM = \frac{1}{cos\theta} \tag{3.6}$$

where θ indicates the solar elevation angle above the horizon.

As the angle of the Sun changes, the thickness of the atmosphere effectively varies, which impacts the spectral distribution of the incoming radiation.

Different spectral filters are employed to simulate solar irradiation under distinct atmospheric conditions:

- AM0[133] represents the solar spectrum from extraterrestrial sources, effectively the Sun's black-body radiation at 5800 K, captured above Earth's atmosphere. This "zero-atmosphere" spectrum serves as the benchmark for PV systems located in space, like those that power satellites.
- AM1[133] describes the sea-level solar spectrum when the Sun is at its zenith.
- AM1.5[133] corresponds to a solar zenith angle of 48.2°, indicating that sunlight travels through 1.5 times the thickness of the atmosphere. In this scenario, the standard illuminance reaches 109,870 lux, resulting in an integrated irradiance of approximately 1000 W m^{-2}. AM 1.5G is the most commonly used testing spectrum for terrestrial PV, offering a realistic average for mid-latitude areas.

a) b)

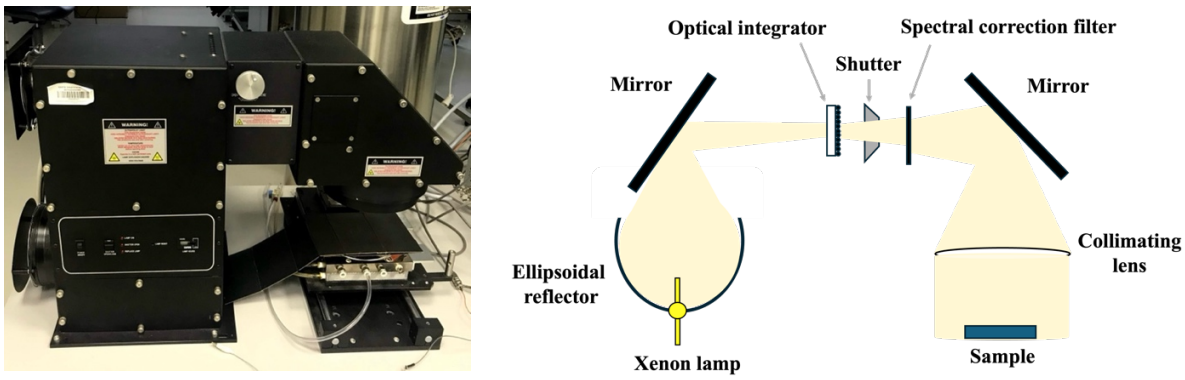

Figure 3.10 a) Oriel Sol3A solar simulator. b) Schematic of the working principle

The four primary metrics that characterize the device's PV performance are V_{oc}, J_{sc}, FF, and PCE. These parameters are experimentally determined using the Oriel Sol3A solar simulator. J_{sc} refers to the maximum current per unit area generated by the cell when the external circuit is shorted[134] and depends on various factors such as the optical absorption efficiency of the active layer, its thickness, and the mobility of generated charge carriers.[135] V_{oc} indicates the maximum voltage produced by the device when no current flows. FF is a metric used to assess the "squareness" of a PV cell J-V curve (Figure 3.11), reflecting the device performance in real operating conditions[135]. A higher FF reflects greater device's efficiency. It is affected by factors such as series and shunt resistances, the built-in electric field, and the charge recombination dynamics.[135] The FF[136,137] is defined by the following equation:

$$FF = \frac{P_{max}}{J_{sc} \times V_{oc}} \tag{3.7}$$

$$P_{max} = J_{mpp} \times V_{mpp} \tag{3.8}$$

where P_{max} indicates the maximum output power, whereas J_{mpp} and V_{mpp} are the maximum power point of the current and voltage.[137]

PCE is the primary metric used to evaluate the effectiveness of PSCs. It represents the maximum proportion of incident solar energy that can be converted into usable electrical power:[137]

$$\eta = \frac{J_{mpp} \times V_{mpp}}{P_{in}} = \frac{J_{sc} \times V_{oc} \times FF}{P_{in}} \quad (3.9)$$

where P_{in} is the power of the incident light.[136]

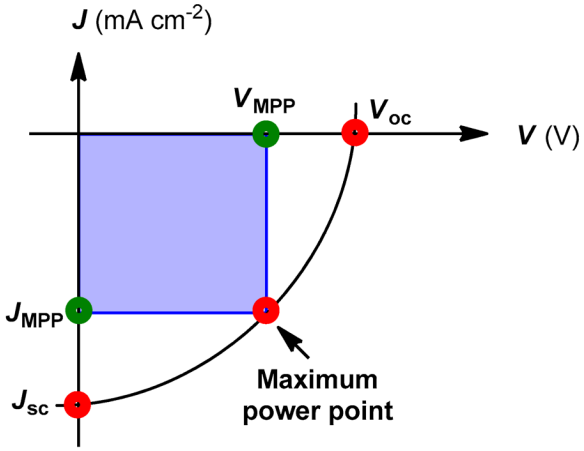

Figure 3.11 The characteristic *J-V* curve of a solar cell; reproduced from Ref.[134] under CC BY 4.0

The external quantum efficiency (EQE) spectra were obtained using an Oriel IQE-200[138] instrument (Figure 3.12a). The system operates by illuminating the device with monochromatic light and measuring the resulting photocurrent (Figure 3.12b). Typically, a xenon gas discharge lamp is employed as the light source, which provides a wide spectrum encompassing all the wavelengths essential for solar cell testing.[137] Simultaneously, the light intensity at each wavelength is monitored using a calibrated reference photodetector. Lock-in amplifiers are leveraged to improve the signal-to-noise ratio.

The EQE is calculated as the ratio of collected electrons to incident photons at a specific wavelength:[137]

$$EQE(\lambda_0) = \frac{I_{ph}(\lambda_0)}{e\Phi_{ph}(\lambda_0)} \quad (3.10)$$

where λ_0 is the wavelength, I_{ph} indicates the photocurrent, e denotes the elementary charge, and Φ_{ph} represents the photon flux incident on the device.[137]

EQE measurements provide wavelength-dependent insight into the device's light absorption and charge extraction efficiency. The devices were measured in the wavelength range of 300–800 nm. The equipment was purchased from Newport Corporation, USA.

a) b)

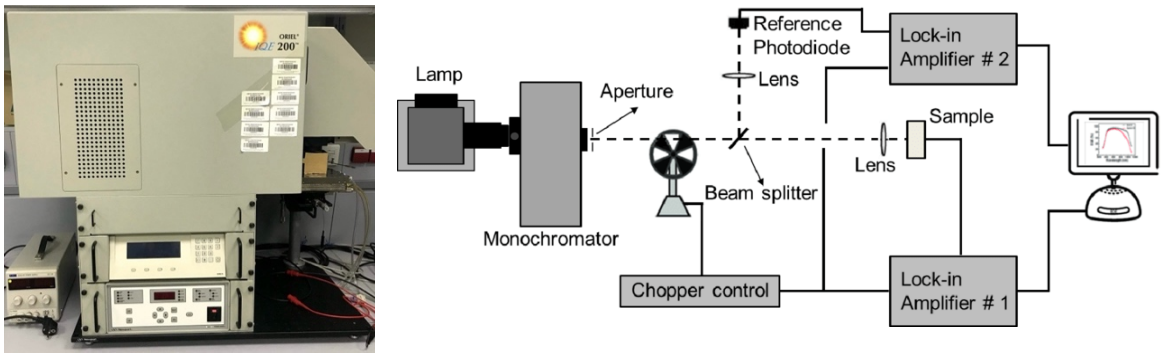

Figure 3.12 a) EQE instrument. b) Illustration of the experimental setup used for EQE measurements; reprinted from Ref with permission (Order №: 6036691359493)

3.4.6 Stability Testing

The operational stability of the PSCs was evaluated by monitoring the evolution of the photocurrent density under continuous illumination. Electrical measurements were performed using a Keysight B1500A semiconductor device analyzer (Figure 3.13), which enables high-precision characterization of semiconductor devices, including current–voltage (*I–V*), capacitance–voltage (*C–V*), and other measurements.

Prior to the stability test, a standard current density–voltage (*J–V*) scan was conducted to determine the voltage at the maximum power point. The device was subsequently biased at the maximum power point voltage, and the photocurrent density was continuously recorded for 10,000 s with a sampling interval of 2000 s under simulated AM 1.5G illumination. The stabilized power output was calculated by multiplying the steady-state current density by the applied bias voltage, thereby confirming the reliability of the photovoltaic performance.

Figure 3.13 Keysight B1500A semiconductor device analyzer

3.4.7 Proton Irradiation

Proton irradiation (PI) tests were conducted using an i-NURA (Nazarbayev University's Research Accelerator) high-voltage (HV_1) pulsed generator-based ion accelerator (Figure 3.14a). Figure 3.14b illustrates the accelerator's operating principle. Upon activation of switch S_1, the energy that has accumulated in the capacitive storage C_1 is delivered to the Blumlein (V_{max}: 180–200 kV) via a step-up Tr_1 pulse transformer. The high voltage initiates a self-triggered breakdown of the nitrogen-filled spark gap (SG), discharging the Blumlein. Under the applied high-voltage pulse, energy propagates along the transmission lines (TL) and through the induction voltage adder (IVA) before reaching the B-applied ion diode. Once the pulse impinges on the Cu anode coated with a polymer dielectric material, a surface flashover discharge is initiated. This voltage pulse then extracts ions from the resulting plasma, accelerating them across the anode-cathode gap of the magnetically insulated ion diode. The instrument operates in single-pulse mode, with a 2 min interval between successive shots. During the experiment, the vacuum chamber is maintained at a working pressure of 0.8 kPa.

The HV_2 generator activates a pulsed current through the diode magnetic field coils. By energizing these coils, HV_2 establishes an external magnetic field that inhibits electron flow, which is spontaneously emitted from the cathode across the anode-cathode gap.

During experiments, the ion beam pulse duration was approximately 150 ns (total temporal width), with a full width at half maximum of ~95 ns, as determined from the Figure 3.14c. The resulting pulsed ion beam was produced with a peak current density of about 4 A

cm^{-2} (Figure 3.14c). Beam fluence was determined by integrating the current density, yielding 2×10^{12} cm^{-2}. The ion beam was primarily composed of protons. All devices were irradiated inside the accelerator vacuum chamber, maintained at ~5×10^{-5} Torr, and each sample was exposed to a single ion-beam pulse. Prior to PI, the beam was triggered by firing ≥10 pulses into a collimated Faraday cup with a magnetic cut-off to remove residual gas species adsorbed on the anode surface and to ensure stable, reproducible proton beam generation.

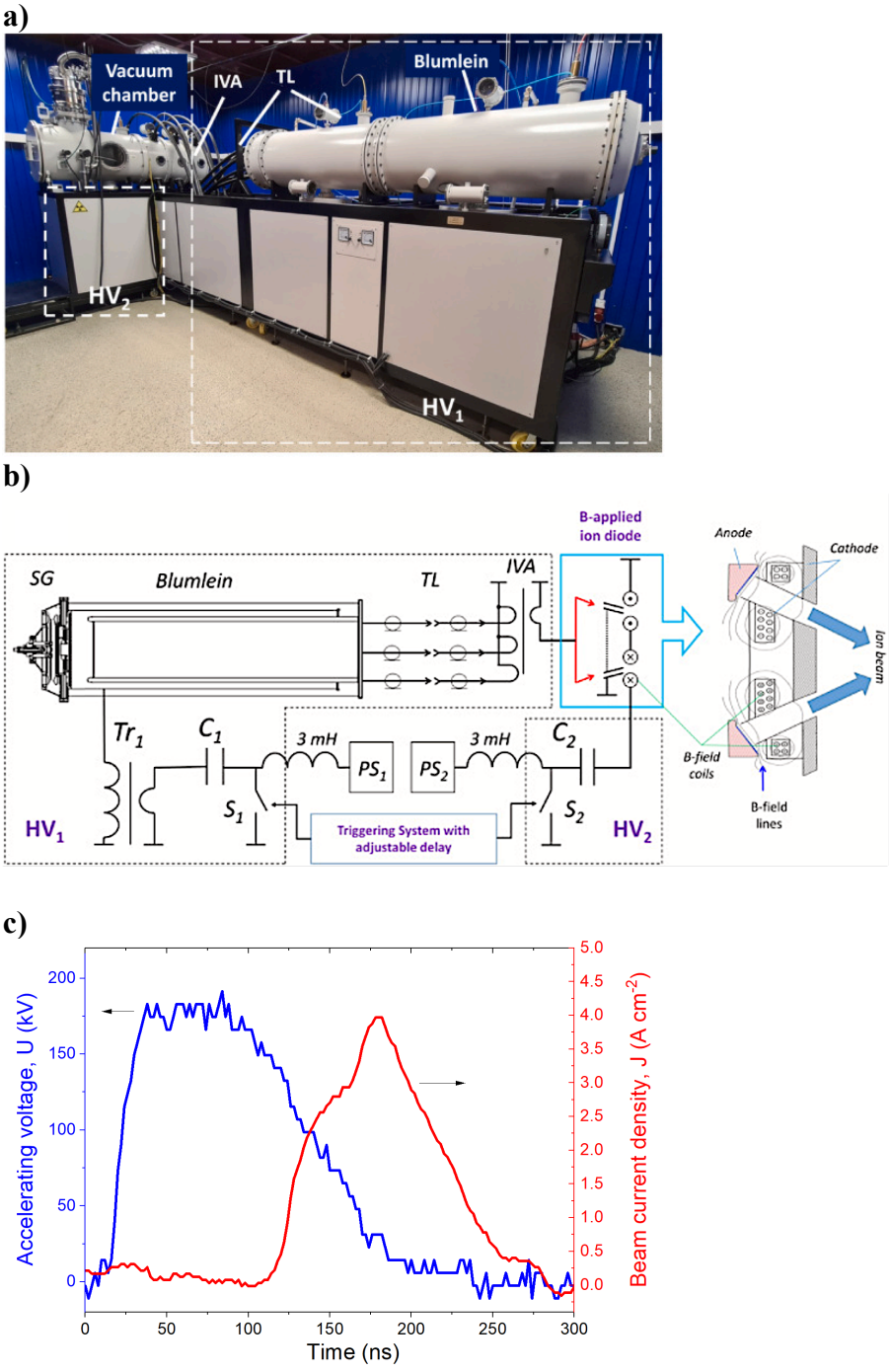

Figure 3.14 a) I-NURA accelerator, b) illustration of the primary subsystems and operating

principle, where PS_1 and PS_2 are the DC power feeds for HV_1 and HV_2; reproduced from Ref.[139] under CC BY 4.0. c) Representative oscillograms showing the pulsed accelerating voltage and ion beam current density

3.5 Technique Development for Cross-sectional AFM Imaging

Characterization techniques play a vital role in the comprehensive analysis of material characteristics, interface integrity, and general device performance. By independently evaluating every layer and combination of layers (i.e., ETL films, perovskite absorbers, CTL/perovskite interfaces, electron-only devices (EOD), and complete devices), the fabrication parameters are systematically defined and optimized to guarantee the repeatability of the results. Among all techniques, I became particularly interested in the AFM tool and dedicated time to independently learning its operation and capabilities. I explored the application of cross-sectional imaging, which is not commonly used because of the technical challenges associated with sample preparation and measurements. Achieving high-resolution AFM cross-sectional images requires careful sample handling to prevent damage to the delicate and sensitive perovskite thin films. Moreover, precise control over the AFM tip and sample surface interaction along the exposed edge is important to avoid tip and sample rapprochement and prevent breakage of the expensive AFM tip.

3.5.1 Sample Preparation

To obtain reliable AFM cross-sectional images, it is essential to physically split the sample into two parts to expose the vertical cross-section of the device. Meticulous attention must be paid to both sample cleanliness and surface quality. The glass substrate must be thoroughly cleaned to prevent any residual contaminants from obscuring the structure of the sample. Surface smoothness is equally critical, given the nanometer-scale proximity between the tip and the sample.

Different methodologies were applied to cut the sample using liquid nitrogen and systematically categorized based on the timing and nature of the cuts. Initially, the samples

were grouped into three main categories based on whether cutting was performed before or after device fabrication.

- ❖ Uncut: The samples were immersed in liquid nitrogen without any precutting. This method was intended to observe the natural fracture behavior under thermal stress.
- ❖ Precut: Samples were scored using a glass cutter before the cleaning procedure. Multiple variations of this method were tested, including vertical and horizontal cuts, to evaluate whether introducing stress points can guide the fracture more predictably. These cuts were performed before perovskite deposition to avoid damaging the active layers after fabrication.
- ❖ Post-cut: Cutting was performed after the deposition of the perovskite absorber layer, carefully avoiding the top surface, to evaluate whether post-deposition scoring leads to cleaner breaks or less disruption in the vertical layer arrangement.

In addition, different cutting geometries were investigated.

- ❖ Full cuts were made through the backside of the substrate, avoiding the front surface to minimize structural damage to the active layers.
- ❖ Partial cuts were made at the top and bottom edges only, leaving the central portion untouched, with the hypothesis that upon immersion in liquid nitrogen, the thermal shock would propagate fractures preferentially along the pre-scored lines, thus achieving a clean break through the active area.

Figure 3.15 presents images of samples subjected to liquid nitrogen-assisted cracking under two distinct conditions: precut and post-cut. In the precut series, the uncut sample remained unchanged after immersion in liquid nitrogen; therefore, it was not included in the post-cut experiments. The resulting fractures lacked directional control and produced unpredictable crack paths, regardless of whether the samples were partially cut before immersion. For this reason, these methods were unsuitable for creating well-defined cross-sectional samples, as evidenced by the fracture patterns observed in the SEM images.

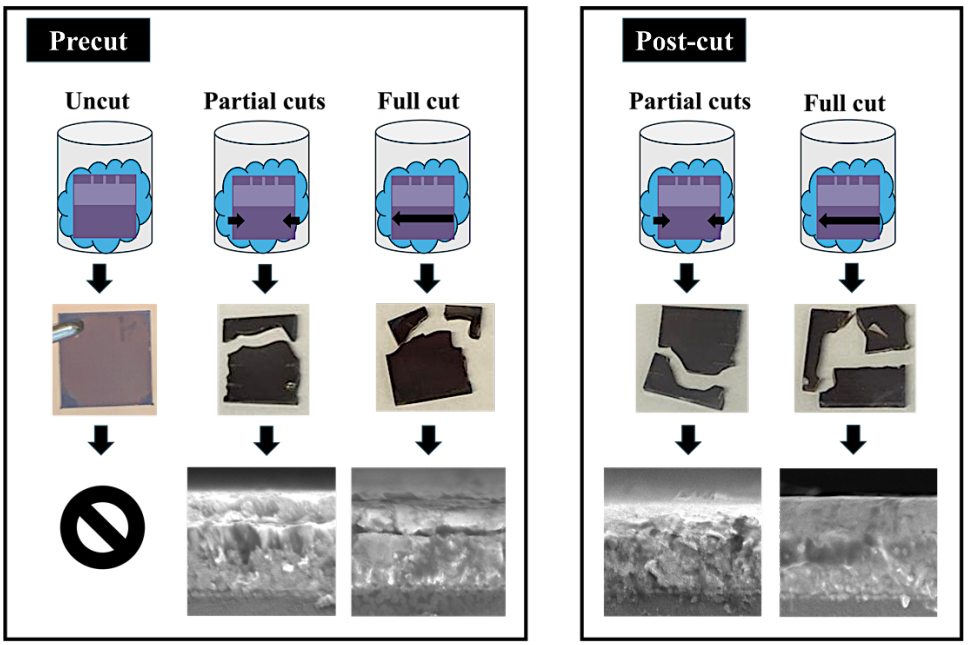

Figure 3.15 Comparison of precut and post-cut strategies used for liquid nitrogen-induced fracturing

Then, a manual cleaving technique was applied. Creating a smooth vertical surface suitable for AFM remained challenging, considering that even minor defects or sharp edges may interfere with tip movement and potentially damage the probe. However, introducing partial cuts after perovskite deposition provided the most representative cross-section images with a distinguishable perovskite layer (Figure 3.16). Therefore, this method was used to prepare all samples for subsequent characterization techniques.

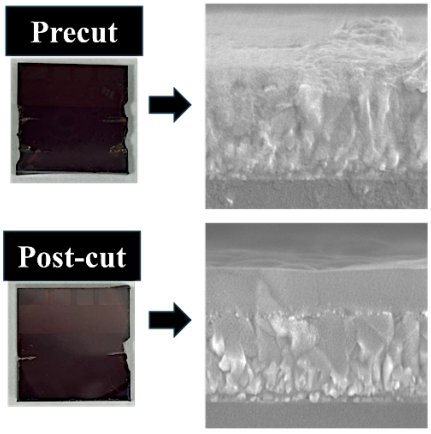

Figure 3.16 Comparison of the manual precut and post-cut methods

3.5.2 Development of a Sample Holder for Cross-sectional AFM Measurements

Owing to the lack of cross-section sample holders in the AFM system, a suitable adaptation

had to be developed to enable proper sample mounting and measurement. The AFM tip is notably sensitive, and even minor surface vibrations or instabilities can negatively affect measurement accuracy. Consequently, a robust and stable holder is essential to hold the sample securely in place during scanning. To enable cross-sectional AFM imaging, an existing holder, originally designed for SEM measurements, was repurposed. This holder was initially equipped with a rear screw mechanism used to fix it onto the SEM stage. In order to adapt it for the AFM system, the screw was carefully removed, allowing the holder to fit into the AFM sample stage without obstruction. Figure 3.17 illustrates the obtained holder. This adjustment made it possible to use the same sample mounting approach for cross-sectional AFM imaging, despite the system not being equipped with a dedicated cross-section sample holder. This practical solution allowed for stable sample positioning and the successful acquisition of cross-sectional AFM images.

Figure 3.17 Adapted cross-section sample holder for the AFM instrument

3.5.3 AFM Cross-sectional Images

Two representative device architectures, namely FTO/hybrid perovskite and FTO/ZnO ink/$CsPbI_2Br$/Spiro-OMeTAD, were measured to investigate their cross-sectional morphology. Height and phase modes were employed to assess the topography and material contrast within the multilayer structures. Figure 3.18 shows the results.

In the FTO/hybrid perovskite sample, the AFM height image shows a relatively

compact and uniform perovskite layer on top of the FTO substrate. Furthermore, the cross-sectional AFM image for the FTO/ZnO ink/$CsPbI_2Br$/Spiro-OMeTAD device shows distinct and well-defined layers. The ZnO interlayer is a compact region between the FTO and $CsPbI_2Br$ layers. The top Spiro-OMeTAD layer appears smoother and more uniform.

It is important to note that AFM phase contrast does not directly reflect an intrinsic property of a bulk material, but instead arises from the local interaction between the AFM tip and the exposed surface.[140,141] This interaction is influenced by interfacial structure, surface roughness, adhesion, and viscoelastic energy dissipation.[141–144] Consequently, phase imaging is effective for distinguishing between different local regions of a material, evaluating coating uniformity, and identifying structural defects such as cracks or degradation features.[142]

In the FTO/hybrid perovskite structure, the exposed FTO region is relatively uniform and mechanically homogeneous, resulting in a consistent phase response. In contrast, in the FTO/ZnO/$CsPbI_2Br$/Spiro-OMeTAD device, multiple layers are located on the FTO and exhibit increased mechanical heterogeneity at the fracture plane. Such interfacial complexity alters local tip–sample interactions and energy dissipation during AFM, resulting in a different phase response compared to the FTO/ hybrid-perovskite sample.

In addition, the FTO region in this cross-section may be affected by cross-contamination originating from the adjacent $CsPbI_2Br$ layer, which is known to be sensitive to prolonged measurement conditions in air (30% RH). Partial degradation of perovskite can introduce inhomogeneities and soft degradation byproducts, which increase viscoelastic damping and tip–sample adhesion. Thus, these effects further alter the measured phase signal. Overall, the observed differences in phase contrast arise from interface- and measurement-condition effects, rather than from any modification of the intrinsic properties of the FTO layer itself.[141]

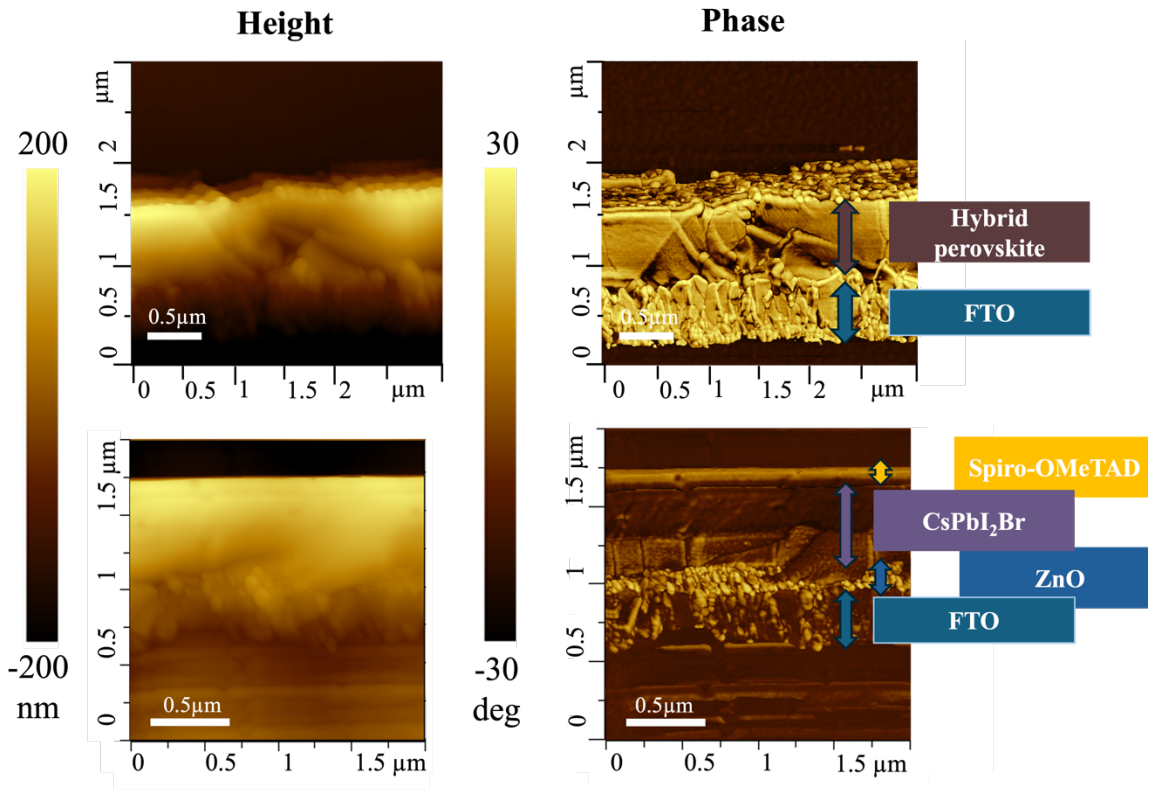

Figure 3.18 Cross-sectional AFM height and phase images of two PSC architectures: FTO/hybrid perovskite and FTO/ZnO ink/$CsPbI_2Br$/Spiro-OMeTAD

3.5.4 Holder Development for Flexible Substrates

In addition to height and phase imaging modes used for morphological assessment, AFM provides access to a range of advanced measurement techniques, including conductive AFM (c-AFM) for mapping local current pathways and studying electrical behavior at buried interfaces. Such techniques may offer further insights into interface quality and local conductivity variations within PSC architectures.

However, adapting c-AFM for FTO glass-based devices is technically demanding, primarily because of the need for a specialized conductive holder compatible with high-resolution scanning and current collection. As a result, attention shifted toward developing a tailored holder for flexible polyethylene terephthalate (PET) substrates coated with ITO, which offers easier handling and integration with compact AFM systems. Moreover, this innovation is timely, considering that flexible PVs are in high demand across various applications owing to their low weight and mechanical compatibility. Foldable solar panels are especially attractive for high-altitude systems, communication satellites, and space

applications. Moreover, adaptable modules may be incorporated into different vehicles, such as airplanes or electric cars, to capture available light and reduce onboard energy usage.

The designed holder enables c-AFM analysis of interfaces within flexible cells, establishing a foundation for precise interfacial engineering. Cross-sectional views of flexible cells reveal interfacial defects. Based on the results, engineering strategies can be applied to mitigate these flaws and improve device performance. Figure 3.19a demonstrates a custom holder and holder platform, which were designed and fabricated using 3D printing.

The holder was developed explicitly for ITO-coated PET substrates with the following features:

- ❖ The ITO-coated PET substrate was positioned into conical semicircle grooves and secured with a conical ring to ensure stability.
- ❖ For c-AFM, an electrical contact for current collection was provided via a screw-based connector (Figure 3.19b).
- ❖ The holder was fixed to the sample stage using an additional screw, ensuring alignment and mechanical stability (Figure 3.19c).

a) b) c)

Figure 3.19 a) 3D-printed holder design, b) holder platform, and c) holder with a sample, used for cross-sectional c-AFM analysis

3.5.5 Summary

Cross-sectional AFM has a high potential for deep nanoscale investigation of interfaces between buried layers, including the assessment of adhesion, mechanical properties, and

defect distribution. These characteristic techniques pave the way for studying and improving the structure and performance of each layer involved.

Achieving high-quality cross-sectional AFM images necessitates smooth, sectioned surfaces and stability during scanning. For this reason, several sample-preparation procedures were assessed for FTO substrates. Manual cutting after perovskite deposition was the most suitable technique, providing a high-quality interface without cracks. To achieve stability during the measurement, a sample holder was developed, which tightly fixes the substrate. This prevents any movements that could potentially damage the AFM tip or degrade the image resolution. After extensive experiments, two different architectures were measured, successfully identifying each constituent layer of the sample.

The secondary objective involved the development of a specialized holder for flexible substrates, enabling c-AFM analysis. By employing 3D printing technology, a substrate holder and holder platform with a screw-driven base were designed. This tailored holder secures thin ITO-PET films within the instrument's limited space and ensures strong electrical contact for dependable current mapping.

Overall, the developed methodology and sample preparation protocols for cross-sectional AFM images can be readily implemented in future studies.

CHAPTER 4: SOLVOTHERMALLY SYNTHESIZED TIN OXIDE NANOSTRUCTURES FOR INTERFACIAL OPTIMIZATION OF HYBRID PSCs

4.1 Introduction

Interfacial engineering has become a crucial strategy in advancing PSCs, focusing on the intentional modification of chemical, structural, and electronic characteristics at material interfaces to reduce non-radiative recombination and enhance charge extraction. Moreover, an optimized ETL/perovskite interface acts as a robust barrier against environmental stressors, thereby significantly enhancing device stability.

Nanostructures provide an advantageous platform for interface modification because of their high surface area, adjustable morphology, and beneficial charge transport properties. In the context of ETLs, incorporating nanostructures like nanorods,[145–148] nanowires,[149–153] and nanotubes,[154–156] has enabled enhancements in charge extraction and reduced recombination at the ETL/perovskite layer interface. Depending on the desired properties, different materials can be engineered into nanostructures.

In recent years, TiO_2 has become the most popular electron transport material (ETM) owing to its improved thermal and chemical stability. Furthermore, the broad range of available synthesis techniques for TiO_2 has enabled the exploration of various nanostructured forms, including nanorods,[145,157–168] nanopyramids,[169] nanosheets,[170,171] nanowires,[150,172–174] nanotubes,[154,175] nanograss,[176] and more complex architectures such as nanoflowers.[177] For example, Yu *et al.*[178] investigated the electron extraction characteristics in PSCs incorporating single-crystal TiO_2 nanorods as the ETL. More effective and directional electron transport, in addition to minimal trap-assisted recombination, was obtained by substituting traditional polycrystalline TiO_2 films with vertically aligned single-crystalline nanorods. The structure of the nanorods offered a direct and uniform pathway for electrons generated by light, leading to a significant reduction in hysteresis and improved device stability. The findings demonstrated that the crystallinity and orientation of the TiO_2

nanorods were crucial in reducing interfacial defects and enhancing charge collection. This technique increased the PCE from 9.13% for devices with planar TiO_2 to 15% for devices with TiO_2 nanorods.[178] Huh *et al.*[179] also employed TiO_2 as a nanostructured ETL, developing optically long and electrically short nanorods for hybrid PSCs. These vertically oriented nanorods facilitated better electron-hole separation and allowed for thicker perovskite layers without creating electrical losses. The fabricated PSCs demonstrated enhanced PV parameters: V_{oc} of 1.120 V, J_{sc} of 23.13 mA cm^{-2}, PCE of 19.86%, and FF of 76.69%.[179] Although TiO_2-based ETLs have enabled devices with high efficiency, their photocatalytic behavior under UV light raises concerns regarding long-term durability. Upon UV exposure, TiO_2 can strip the electrons from iodide ions in the $CH_3NH_3PbI_3$ absorber material, driving its irreversible decomposition into PbI_2 and MAI.[180] At the same time, photogenerated holes within the TiO_2 migrate to surface oxygen vacancies, where they react with adsorbed O_2, which exacerbates charge carrier recombination at the interface.[180] Furthermore, the elevated processing temperatures necessary for TiO_2 increase their manufacturing costs.

ZnO has emerged as a highly attractive ETM alternative to TiO_2. ZnO exhibits superior charge mobility (100–200 $cm^2\ V^{-1}s^{-1}$)[181] and requires substantially lower fabrication temperature, thereby reducing energy consumption and manufacturing expenses. Additionally, ZnO can be engineered into diverse nanostructures: nanoparticles,[182] nanorods,[183–190] and nanowires.[181,191] For instance, Li *et al.*[187] used ZnO nanorods as ETL for $MAPbI_3$ PSCs. The nanostructures were synthesized via a hydrothermal self-assembly method and demonstrated superior electron mobility and low temperature processability. In addition, ultrathin Al_2O_3 passivation layers were deposited on the ZnO nanorods by ALD. This architecture significantly improved device efficiency, increasing the PCE from 10.33% to 15.06%.[187] Despite its superior charge-transport characteristics, ZnO-ETL PSCs underperformed relative to TiO_2-ETL devices in PCE. This performance gap can be explained by two interrelated factors: (i) a high density of surface defects in ZnO, which act

as non-radiative recombination centers,[192] and (ii) the tendency of ZnO to deprotonate MA cations at the perovskite interface.[193] Together, these phenomena impose stricter limits on both the maximum annealing temperature and thermal treatment duration, often yielding incompletely converted precursors and perovskite films with poor crystallinity. Consequently, successful implementation of ZnO as an ETM demands careful pairing with compatible perovskite materials such as all-inorganic variants. Moreover, developing optimized processing protocols can effectively mitigate defect formation and promote high-quality perovskite crystallization.

Despite receiving less attention than TiO_2 and ZnO, SnO_2 exhibits superior electronic performance and chemical stability, effectively overcoming many of the drawbacks associated with those metal oxides. Notably, SnO_2 demonstrates electron mobilities in the range of 100–250 $cm^2\,V^{-1}\,s^{-1}$, outperforming ZnO (100–200 $cm^2\,V^{-1}\,s^{-1}$) and significantly surpassing TiO_2, which typically exhibits mobilities below 1 $cm^2\,V^{-1}\,s^{-1}$.[194] This high electron mobility enables efficient and rapid charge extraction with minimal resistive losses. Furthermore, the wide bandgap of SnO_2 (~3.6 eV),[195] compared with TiO_2 (~3.0 eV)[195] and ZnO (~3.37 eV),[196,197] allows more visible light to transmit through the device. The SnO_2 deep-lying conduction band minimum is also well-matched to perovskite absorber levels, thereby elevating the V_{oc} parameter. Similar to ZnO, SnO_2 ETMs can be synthesized through various low-temperature processing methods, which benefits the advancement of flexible PSCs. Crucially, the material's inherent lack of photocatalytic activity prevents deleterious interfacial reactions, enhancing the chemical robustness of the active layer and extending the operational lifespan of perovskite devices. SnO_2 has also been investigated and utilized in various nanostructured forms: nanoparticles,[198–200] nanorods,[201–204] nanocrystals,[205] and nanosheets.[206–208] For example, Zhang *et al.*[201] grew vertically aligned SnO_2 nanorod arrays (NAs) through a hydrothermal process in an acidic solution. Structural characterization techniques confirmed the formation of highly crystalline tetragonal rutile SnO_2. Mixed perovskite compositions of $(FAPbI_3)_{0.85}(MAPbBr_3)_{0.15}$ were infiltrated into the

nanostructured ETL, resulting in improved electron transport and reduced interfacial recombination. This interface engineering strategy significantly increased the average PCE from 11.54% in the control device to 14.9%, demonstrating the beneficial impact of nanostructured SnO_2 on charge extraction processes.[201] Xu *et al.*[204] conducted a comparative study on nanorod-based ETLs composed of both TiO_2 and SnO_2 materials. The nanostructures were synthesized via a solution-based method, employing oleic acid (OA) as a surface-capping ligand to control morphology and ensure uniform dispersion. The findings demonstrated that OA-capped SnO_2 nanorods led to superior PV performance compared with their TiO_2 counterparts. Devices based on SnO_2 NAs achieved an V_{oc} of 1.115 V, J_{sc} of 22.66 mA cm^{-2}, FF of 71.66%, and PCE of 18.09%, whereas those based on TiO_2 NAs showed a V_{oc} of 0.98 V, J_{sc} of 19.88 mA cm^{-2}, FF of 63.42%, and PCE of 12.39%[204]. Moreover, SnO_2-NRs-based devices exhibited reduced hysteresis owing to the diminished trap-state density of the perovskite material.

Although SnO_2 nanostructures have been successfully integrated into PSCs, the reported PV performance has significantly varied across the literature. The wide range of different results is primarily attributed to the sensitive dependence of SnO_2 nanostructure morphology on the synthesis parameters, such as the precursor concentration, solvent composition, temperature, reaction time, etc. These factors critically influence the resulting nanostructure's size, orientation, crystallinity, and surface quality, complicating the development of consistent and optimized processing protocols.

To address these challenges, the solvothermal synthesis of SnO_2 NA-based hybrid PSCs was investigated herein, aiming to establish precise control over the morphological properties and improve reproducibility. A systematic study was conducted to analyze the impacts of key growth parameters, namely (i) growth pressure, (ii) substrate orientation, (iii) DI water-to-ethanol ratio, (iv) type of seed layer, (v) concentration of acetic acid, and (vi) growth time. The resulting SnO_2 NAs were comprehensively characterized to assess their structural and morphological quality. These findings provide valuable insights into the

optimal growth conditions for high-quality, reproducible SnO_2 nanostructures, thereby advancing their integration as efficient and stable ETLs in PSCs.

4.2 Device Fabrication

The cleaning of FTO-coated substrates was performed according to the procedure described in Chapter 3.2.1. The device architecture was fabricated in the following order: FTO glass/ ETL seed layer/SnO_2 NA/hybrid perovskite/HTL/Au contacts, where the HTL layer was deposited according to the protocol detailed in Chapter 3.2.2, and the Au contacts were evaporated as described in Chapter 3.2.3.

4.2.1 Synthesis of the SnO_2 NAs

The solvothermal synthesis of SnO_2 NAs was carried out in two steps. First, 0.15 mmol of NaBr was dissolved in 0.75 mL of DI water. Separately, a solution with 0.05 mmol of $SnCl_4 \cdot 5H_2O$ in 6 mL of glacial acetic acid was stirred for 10 min to ensure complete dissolution. Then, the two solutions were thoroughly mixed, followed by the addition of 0.75 mL of ethanol to the mixture. The precursor solution was poured into a Teflon-lined autoclave reactor, and the pre-cleaned FTO-coated substrates were vertically positioned within the reactor, ensuring they were fully immersed in the solution. The reactor vessel was sealed and heated in a muffle furnace at 200 °C for 12 h to initiate the solvothermal growth of SnO_2 nanorods. After cooling, the substrates were removed and gently rinsed with DI water and ethanol in an ultrasonic bath to eliminate any residual byproducts.

4.2.2 Optimization of the SnO_2 NA Growth by Varying the Synthesis Parameters

(I) Growth Pressure

The influence of growth pressure on the formation of SnO_2 NAs was investigated by introducing a fixed volume of precursor solution (7.5 mL) into Teflon-lined autoclaves of varying capacities: 25, 50, and 100 mL (Figure 4.1). The autoclave reactors were filled to

30%, 15%, and 7.5% of their total volume, respectively. As expected, the internal pressure generated during solvothermal processing was proportional to the filling ratio, with higher ratios leading to increased built-up pressure. In a separate set of experiments, a constant filling ratio of 7.5% was maintained across all autoclave volumes by adjusting the amount of synthesis solution added into all reactors accordingly. This approach allowed for the decoupling of the reactor volume from internal pressure effects.

Figure 4.1 Teflon-lined autoclaves of 100, 50, and 25 mL capacity employed for solvothermal synthesis

(II) Substrate Orientation

Three geometrically distinct orientations of the ETL-coated substrates were examined to evaluate the effect of substrate orientation on SnO_2 nanorod growth. The samples were positioned with the conductive FTO side facing downward at 0° (horizontal), 45°, and 90° (vertical), relative to the bottom surface of the Teflon-lined autoclave. Poly(tetrafluoroethylene) sample holders were employed during the experiments to ensure stability and consistent positioning during the solvothermal process. The filling ratio was fixed at 7.5%, using 100 mL autoclaves for all three orientation conditions to maintain a consistent internal pressure and reaction volume.

(III) DI Water-to-ethanol Ratio

The influence of solvent composition was investigated for five different DI water-to-ethanol ratios: 1:9, 3:7, 1:1, 7:3, and 9:1. For the 1:1 condition, a total of 1.5 mL of mixed solvent was prepared using 0.75 mL of DI water and 0.75 mL of ethanol. For the remaining ratios,

the volume of each solvent component was adjusted accordingly to maintain a constant total solvent volume of 1.5 mL. Across all experimental conditions, the concentrations of the other precursor components were kept constant: 6 mL of glacial acetic acid, 0.05 mmol of $SnCl_4 \cdot 5H_2O$, and 0.15 mmol of NaBr.

(IV) Different Seed Layers

To facilitate the subsequent solvothermal growth of SnO_2 NAs, three different types of seed layers—thin films, nanoparticles, and QDs—were deposited onto FTO-coated substrates to enable a comparative evaluation of their effectiveness in promoting high-quality nanorod growth. The fabrication methods are detailed below:

- SnO_2 thin films were deposited using radio frequency (RF) magnetron sputtering, employing a SnO_2 ceramic target with 99.99% purity and a diameter of 50.8 mm. Deposition was carried out under a pure argon atmosphere while maintaining a working pressure of 5×10^{-3} Torr, yielding SnO_2 films with uniform thicknesses of approximately 10 nm.
- SnO_2 QD seed layers were prepared by dissolving 3.99 mol of $SnCl_2 \cdot 2H_2O$ in DI water. The precursor solution was continuously stirred for 3–4 h under an oxygen flow of 1 L min^{-1} and filtered using a 0.45 μm syringe filter to remove any particulates or undissolved residues. The FTO substrates were coated with the QD solution by spin-coating at a speed of 3000 rpm for 30 s. Following deposition, the QD-coated substrates were annealed at 200 °C for 1 h.
- SnO_2 nanoparticles layers were prepared by diluting a colloidal dispersion of 15% SnO_2 in DI water using a 1:5 volume ratio. The precursor solution was deposited by spin-coating onto FTO substrates at 3000 rpm for 30 s. Then, substrates were placed onto a hotplate at 150 °C for 30 min.
- The procedure used for preparing the SnO_2 NA solution is described in the 4.2.1 section, with the exception that 6.75 mL of glacial acetic acid (instead of 6 mL) was added to the mixture. Thus, the filling ratio of the Teflon-lined reactor for this condition was

maintained at 8.3%.

(V) Glacial Acetic Acid Concentration

The impact of glacial acetic acid concentration on the growth of SnO_2 nanostructures was investigated by varying its volume to 6, 6.5, and 9.75 mL**,** corresponding to reactor filling ratios of 7.5%, 8%, and 11.3%**,** respectively. Throughout the experiments, a 1:1 volume ratio of DI water to ethanol was maintained in the precursor solution to ensure consistent solvent composition.

(VI) Growth Time

The growth time parameter was studied by applying different times in a muffle furnace. SnO_2 thin film-coated substrates were immersed in the SnO_2 NAs precursor solution with a slight modification: 6.75 mL of glacial acetic acid was used instead of 6 mL. The growth process was conducted at 200 °C for 6, 12, and 24 h to study the effect of growth time on nanorod morphology. An additional growth condition was also established: using an initial duration of 12 h, then substituting the original precursor with a freshly synthesized solution and continuing for an extra 12 h of growth.

4.2.3 Perovskite Layer Deposition

The hybrid perovskite precursor solution includes a mix of solutes 1.2 M PbI_2, 1.1 M FAI, 0.2 M $PbBr_2$, 0.2 M MABr, 0.4 M MACl in DMSO, and 1 mL of DMF using 1:4 volume ratio. Next, the precursor solution was stirred for 5 h and subsequently filtered through a 0.45 μm syringe filter. Then, 28 μL of a 1.5 M cesium iodide (CsI) solution in DMSO and 28 μL of a 1.5 M rubidium iodide (RbI) solution in a DMF:DMSO (4:1) solvent mixture were added to 940 μL of the filtered precursor solution, yielding a triple-cation mixed halide perovskite formulation. The perovskite precursor solution was deposited onto the optimized SnO_2 NAs, which had been pretreated with oxygen plasma for 15 s at 70 W. The deposition process involved a two-step spinning procedure, first at 1000 rpm for 10 s, followed by 5000 rpm for 30 s. During the final 10 s of the spin-coating, a CB antisolvent was carefully dropped

onto the spinning substrate. Following deposition, the perovskite films were annealed on a hotplate at 105 °C for 75 min.

4.3 Morphological Study of the SnO_2 Nanostructure

Understanding the influence of individual growth parameters on the morphology of SnO_2 NAs is essential for achieving precise control over structural features. Notably, some parameters are interdependent, and their interactions can affect the growth outcome. For instance, modifying the glacial acetic acid concentration affects the total volume of the SnO_2 NA solution, which modifies the autogenous pressure within the sealed autoclave during solvothermal treatment. Even when the molar ratios of precursors are held constant, such volumetric changes impact both the reaction dynamics and the absolute concentration of growth species. Therefore, a comprehensive experimental study is necessary to assess each parameter's influence and clarify their combined effects on the morphology of the formed nanostructures. Such an approach is crucial for achieving the reproducible synthesis of high-quality SnO_2 nanostructures for PSC applications.

4.3.1 Effect of Pressure

The investigation of the pressure effect was conducted using various-sized Teflon-lined autoclave reactors: 25, 50, and 100 mL. Despite different sizes, a constant precursor solution volume and composition were maintained. The solvothermal procedure was conducted at 200 °C for 12 h. A pressure gauge was connected to the autoclave during the reaction, enabling real-time monitoring of the internal pressure. The internal pressure generated during the reaction is expected to be inversely related to the reactor volume but directly proportional to the filling ratio. The measured pressures corresponding to filling ratios of 30%, 15%, and 7.5% were approximately 130.0, 87.0, and 72.5 psi, respectively.

The SEM analysis presented in Figure 4.2 demonstrates a clear dependence of SnO_2 NA morphology on the internal pressure developed during the solvothermal process.

Although the chemical composition and volume of the precursor solution remained identical across all samples, varying the size of the Teflon-lined autoclave reactors significantly influenced the internal pressure and, consequently, the resulting nanostructure. A notable trend was observed; increasing the internal pressure, achieved by using smaller reactor volumes with the same precursor volume, led to substantial changes in morphology. The nanorods tended to develop into larger and denser clusters, and the overall thickness of the layers of grown nanorods increased accordingly (Figure 4.2a,b). In contrast, SEM images of samples prepared using the 100 mL reactor volume displayed more distinguishable nanorods (Figure 4.2c). Cross-sectional SEM images (Figure 4.2d–f) confirmed that the average thicknesses of the NAs were approximately 425 ± 21, 319 ± 19, and 131 ± 12 nm for the 25, 50, and 100 mL reactors, respectively. These observations were further supported by statistical measurements of the bundle diameters and lengths, which are summarized in Table 4.1. The morphological differences can be attributed to the alterations in Gibbs free energy. An increase in pressure promoted faster nucleation and crystal growth rates, which resulted in larger crystallites and thicker films. Additionally, elevated pressure encourages the coalescence of individual nanorods into bundles.

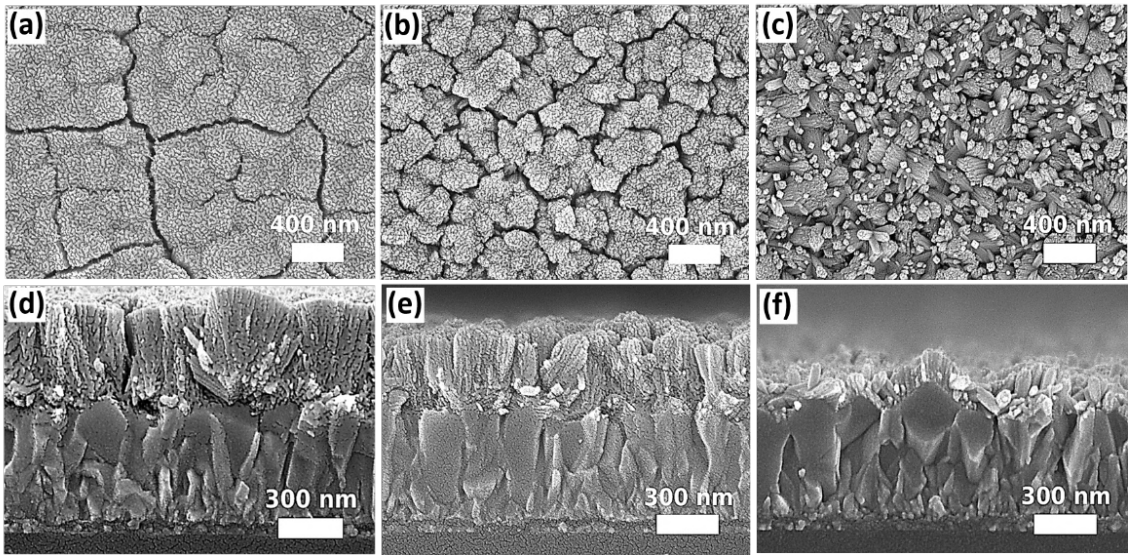

Figure 4.2 SEM top-view and cross-sectional images of SnO_2 nanostructures grown in autoclaves of varying volumes: (a,d) 25 mL, (b,e) 50 mL, and (c,f) 100 mL; reproduced from Ref[209] under CC BY 4.0

Table 4.1 Summary of the nanostructure lengths and bundle diameters obtained under different pressures. Adapted from Ref[209] under CC BY 4.0

Condition	Length of nanostructure			Diameter of SnO_2 bundle		
	Min (nm)	Max (nm)	Mean ± SD	Min (nm)	Max (nm)	Mean ± SD
25 mL (130 psi)	383	478	425±21	1092	1484	1220±140
50 mL (87 psi)	278	349	319±19	244	572	389±82
100 mL (72.5 psi)	108	156	131±12	40	112	60±21

Achieving precisely tailored SnO_2 nanostructures requires control over the internal pressure, which is governed by the precursor filling ratio relative to the reactor volume. However, varying the filling ratio also changes the total solute quantity, introducing a secondary variable that may affect morphology. To decouple these effects, the same filling ratio (and thus identical pressure) was maintained in all reactors, despite differing absolute solute amounts. The pressure-driven morphology control was validated by adjusting the precursor volumes in the 25, 50, and 100 mL autoclaves to maintain a uniform 7.5 % filling ratio, providing identical internal pressures during 12 h of solvothermal growth. The 7.5% filling ratio was strategically chosen to engineer SnO_2 NAs with ample inter-rod voids and, hence, reduced density. Thus, perovskite material infiltrated the spaces between the SnO_2 nanorods, enhancing interfacial contact for improved charge transport. Figure 4.3 shows top-view and cross-sectional SEM images of SnO_2 NAs grown under isobaric conditions of 72.5 psi across the three different reactor volumes (25, 50, and 100 mL). Their similar morphologies confirm that maintaining the same pressure ensures reproducible nanostructure formation, revealing that pressure, rather than precursor volume, is the decisive factor governing SnO_2 nanostructure growth.

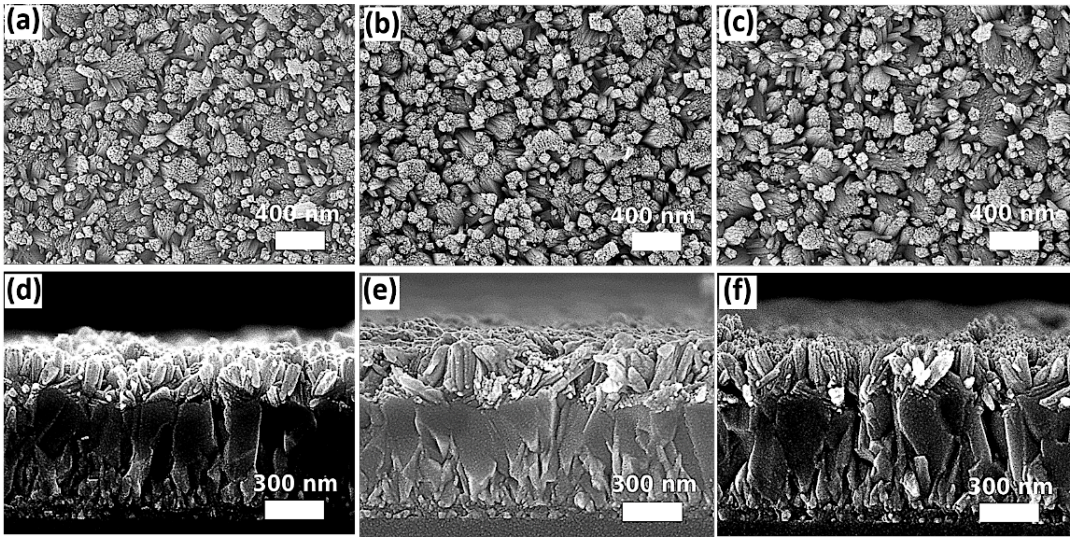

Figure 4.3 SEM top-view and cross-sectional images of SnO_2 nanostructures grown at identical pressure by adjusting the precursor solution volume to the same filling ratio in three autoclave reactors with different sizes: (a,d) 25 mL; (b,e) 50 mL; and (c,f) 100 mL; reproduced from Ref[209] under CC BY 4.0

4.3.2 Effect of Substrate Orientation

Substrate alignment within the solvothermal autoclave significantly influences the SnO_2 nanostructure. FTO substrates were mounted face down at three inclinations (0°, 45°, and 90°) inside the 100 mL Teflon-lined reactors under identical thermal and pressure conditions. Figure 4.4 presents SEM images of these orientation-dependent samples. When the sample is positioned face downward (0°), uniform precursor flux to the whole sample promotes a high density of vertically oriented nanorods (Figure 4.4c). In contrast, tilting the substrate to 45° or 90° disrupts this flux, producing NAs with multiple growth orientations and a lower density of upright rods (Figure 4.4a,b). The crystallographic orientation of nanorods plays a critical role in device performance. Poor alignment can result in nanorod overlap and bundling. Consequently, an optimized SnO_2 nanorod ETL should exhibit well-controlled interrod spacing to promote uniform perovskite grain growth and intimate interfacial contact.[209] Vertically aligned NAs are particularly advantageous because they provide direct, continuous pathways for electron transport, suppressing carrier recombination.[201,209,210] Also, Zhang *et al.*[201] reported that vertical alignment of nanorod structure reduces hysteresis.

According to the Table 4.2, the vertically inclined configuration results in markedly

larger bundle diameters (91 ± 41 nm) and shorter nanorod lengths (116 ± 21 nm) compared with those obtained at 0° (diameter, 64 ± 14 nm; length, 132 ± 13 nm) and 45° (diameter, 69 ± 28 nm; length, 135 ± 30 nm). The nanorods obtained under the 0° condition exhibit a higher aspect ratio, defined as AR = length/diameter[211] (AR ≈ 2.06), compared with those grown under the 90° condition (AR ≈ 1.27). A higher aspect ratio increases the effective interfacial area at the SnO_2/perovskite interface, providing more electron extraction sites and facilitating more efficient charge transfer. The broader diameter distribution (±41 nm) observed for the thicker nanorods in this work is expected to introduce interfacial nonuniformity, potentially increasing recombination losses. Moreover, the thicker nanorods create narrow and irregular inter-rod gaps that can hinder perovskite precursor penetration and lead to interfacial void formation.

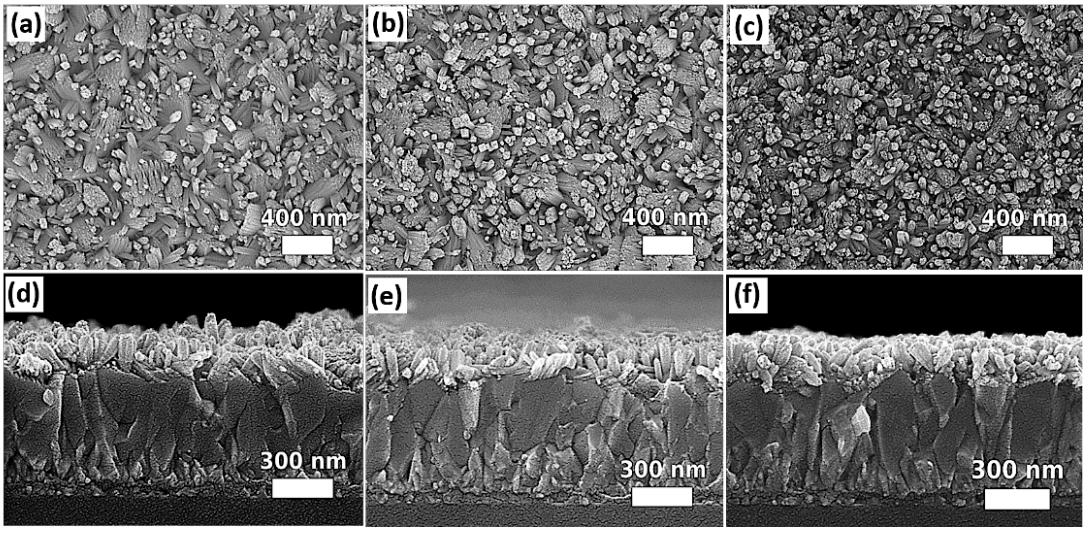

Figure 4.4 SEM top-view and cross-sectional images of SnO_2 samples grown under the same solvothermal conditions but with substrates oriented at (a,d) 45°, (b,e) 90°, and (c,f) 0°; reproduced from Ref[209] under CC BY 4.0

Table 4.2 Summary of the nanostructure lengths and bundle diameters obtained under different substrate orientations. Adapted from Ref.[209] under CC BY 4.0

Condition	Length of nanostructure			Diameter of SnO_2 bundle		
	Min (nm)	Max (nm)	Mean ± SD	Min (nm)	Max (nm)	Mean ± SD
45°	87	178	135±30	42	156	69±28
90°	86	154	116±21	42	185	91±41
0°	105	152	132±13	46	91	64±14

Owing to the pronounced morphological differences observed at various substrate angles, AFM tool was employed to further characterize the surface topography. Figure 4.5 presents the AFM-derived root mean square (RMS) roughness values, showing 0.09, 0.04, and 0.07 µm for the SnO_2 films grown with substrates inclined at 45°, 90°, and 0°, respectively. In this study, positioning the substrate face down (0°) is more effective than other angles because those orientations impose more limitations on the substrate dimensions owing to the design of the Teflon-lined autoclaves. Given the impracticality of inclined configurations, larger substrates cannot be completely submerged in the precursor solution, leading to uneven growth of the SnO_2 nanostructures. Consequently, for subsequent investigations of other growth parameters, the substrates were placed horizontally (0°) for the solvothermal growth process.

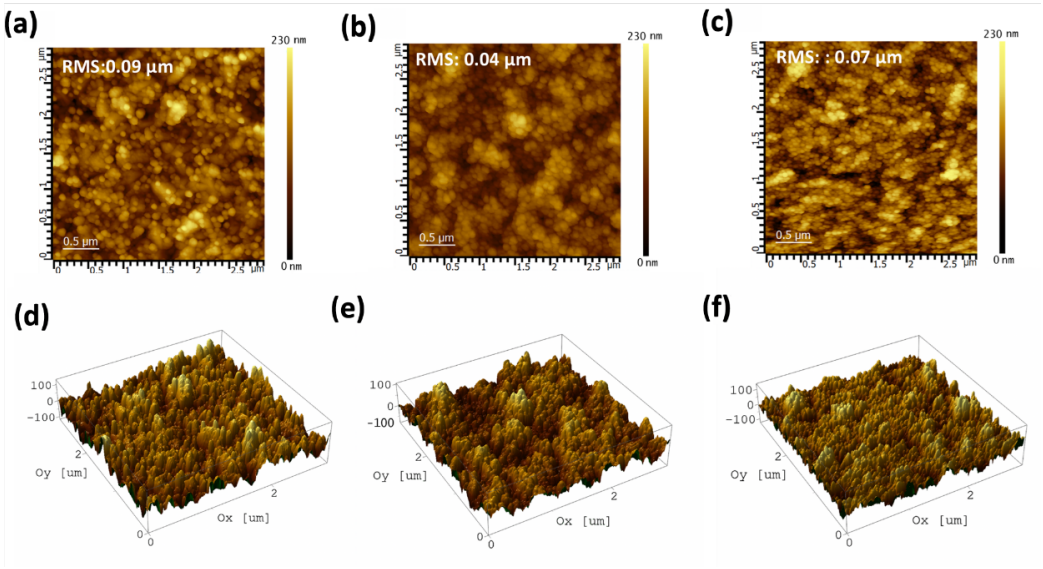

Figure 4.5 AFM images of SnO_2 nanostructures grown under solvothermal conditions with substrates inclined at (a,d) 45°, (b,e) 90°, and (c,f) 0°; reproduced from Ref[209] under CC BY 4.0

4.3.3 Effect of DI Water-to-ethanol Ratio

Accurate regulation of the solvent conditions is essential for guiding the nucleation and directional growth of SnO_2 nanorods during solvothermal synthesis. Chen *et al.*[212] showed that acetic acid, ethanol, and DI water must be mixed in exact volumetric ratios to drive uniform nanorod formation on Ti substrates. In this study, the recipe of the SnO_2

nanostructure, as described by Chen *et al.*[212], was adjusted to fit the dimensions of the autoclave reactors and the specific established experimental conditions.

The complex interdependence of DI water, ethanol, and acetic acid makes ternary solvent optimization especially challenging. Consequently, the influence of solvents on the SnO_2 NAs was separately examined by varying the DI water-to-ethanol ratio (1:9, 3:7, 1:1, 7:3, or 9:1) while the other components of the precursor solution were held constant within a 100 mL reactor, with a total mixture volume of 1.5 mL. Figure 4.6 shows SEM images of the samples obtained under these conditions.

The hydrolysis of $SnCl_4 \cdot 5H_2O$ occurs in the presence of DI water, and ethanol aids in creating an oriented array of SnO_2 nanorods. Consequently, modulating the water content influences the hydrolysis rate; at a low water content (Figure 4.6a,b), hydrolysis proceeds at a rate that balances nucleation, yielding sharply defined SnO_2 NAs. According to Chen *et al.,*[212] insufficient water content leads to slow hydrolysis, thereby growing cube-shaped nanoparticles following a 24 h solvothermal procedure. Contrary to that work, the water content in our ternary solvent system remains above the critical hydrolysis threshold, thus forming well-defined Nas, even at the lowest DI water fraction.

The different concentrations of ethanol show a notable effect on the morphology of SnO_2 nanostructures. For example, a minimal quantity of ethanol (Figure 4.6 i,j) results in a thin layer of nanoparticles. These findings align with data presented by Chen *et al.,*[212] where reduced ethanol concentration favors the formation of SnO_2 nanoparticles over nanorods. Meanwhile, our results also show a shift from nanoparticles to clearly defined nanorods. The 1:9, 3:7, 1:1, and 7:3 conditions demonstrate that incremental increases in ethanol content progressively shift the nucleation growth balance toward one-dimensional nanorods.

Note that a high ethanol concentration induces pronounced SnO_2 bundles, as shown in Figure 4.6a, compared with the 3:7 and 1:1 ratio images. For the DI water-to-ethanol ratio of 7:3, the nanostructure becomes almost indistinguishable from the top view (Figure 4.6g). In contrast, the cross-sectional SEM image (Figure 4.6h) demonstrates a packed assembly of

clusters and rod segments, reflecting the synergistic effect of elevated DI water content combined with a moderately low ethanol proportion.

It is important to recognize that different solvents exhibit varying molecular weights and boiling points, whose distinct volatilities may affect the autogenous pressure during solvothermal synthesis. For instance, DI water has a molecular weight of approximately 18 $g \cdot mol^{-1}$[1213] and boils at 100 °C,[213] whereas ethanol's molecular weight is roughly 46 $g \cdot mol^{-1}$[1214] with a boiling point of 78 °C.[214] To investigate the combined effect of these solvents, the autogenous pressure generated within the autoclave was monitored using a pressure gauge for three DI water-to-ethanol ratio (1:9, 1:1, and 9:1).

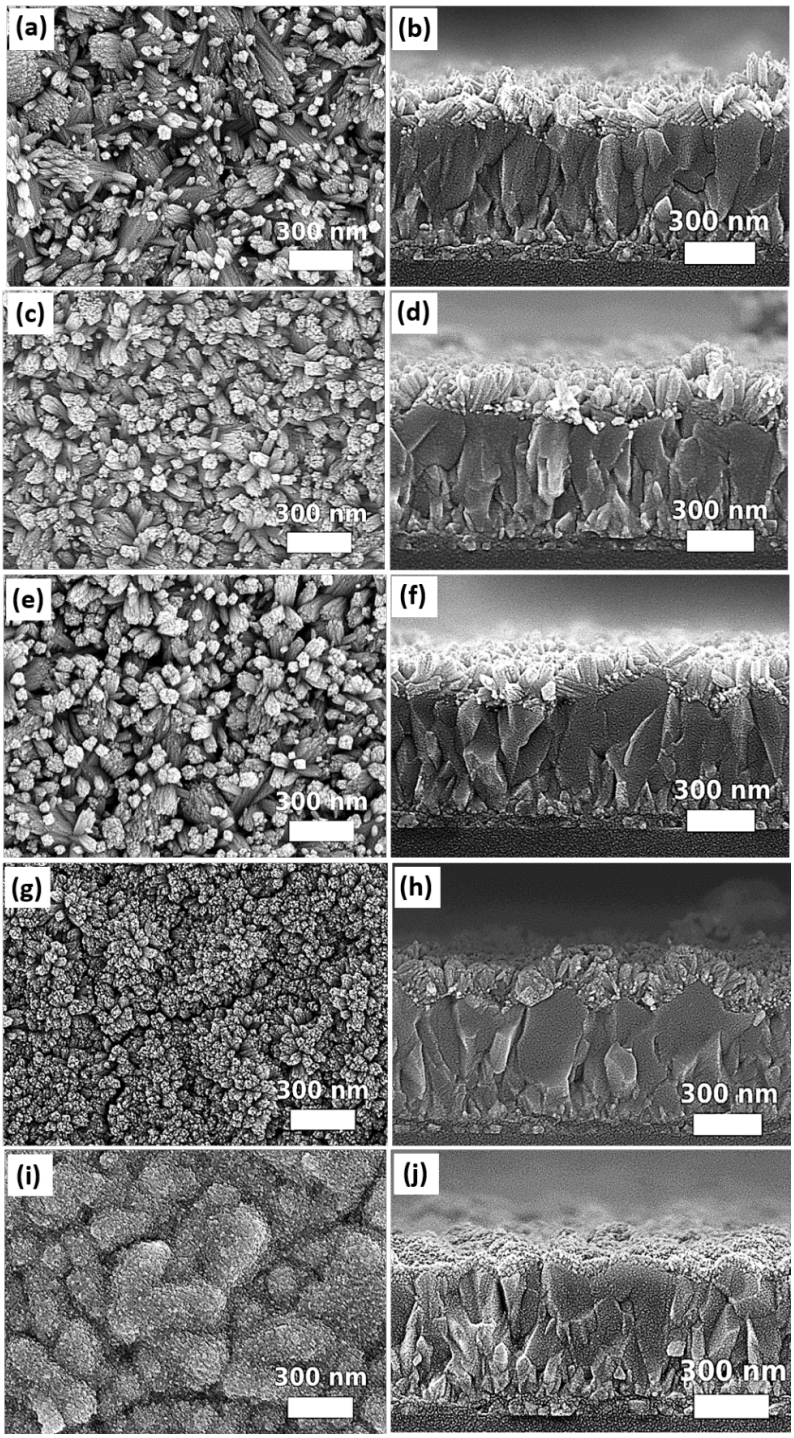

Figure 4.6 Top-view and cross-sectional SEM images of the SnO_2 NA morphology obtained by varying the DI water-to-ethanol ratio: (a,b) 1:9, (c,d) 3:7, (e,f) 1:1, (g,h) 7:3, and (i,j) 9:1; reproduced from Ref[209] under CC BY 4.0

Notably, all three formulations stabilized at approximately 72.5 psi, demonstrating that in a high-temperature environment (200 °C) with constant headspace (7.5% filling ratio), the total vapor pressure remains effectively unchanged by variations in the solvent ratio. The results suggest that changes in the pressure related to the varying ratio of DI water to ethanol have a minimal impact on the alterations of SnO_2 nanostructures.

Table 4.3 shows a summary of the obtained nanostructure dimensions. A reduced DI water content slows the hydrolysis of $SnCl_4 \cdot 5H_2O$, whereas higher ethanol content encourages nanorod clustering. The slower hydrolysis rate decreases nucleation density, increasing the precursor flux available to each rod, thereby promoting axial elongation and radial thickening. For the further investigation of other solvothermal growth parameters, the DI water-to-ethanol ratio of 1:1was chosen.

Table 4.3 Summary of the nanostructure lengths and bundle diameters obtained under different DI water-to-ethanol ratios. Adapted from Ref[209] under CC BY 4.0

Condition	Length of nanostructure			Diameter of SnO_2 bundle		
	Min (nm)	Max (nm)	Mean ± SD	Min (nm)	Max (nm)	Mean ± SD
1:9	111	188	149±22	57	126	82±23
3:7	103	178	136±18	50	98	73±15
1:1	102	154	131±16	45	83	61±11
7:3	69	129	100±19	26	70	41±12
9:1	30	77	48±14	NA	NA	NA

4.3.4 Effect of Different Seed Layers

Typically, a compact ETL seed layer serves as a scaffold for the nanostructure, to prevent perovskite from completely penetrating the nanostructure and reaching the FTO, where electrical shorting occurs. In this study, three seed layer configurations were fabricated, including dense magnetron-sputtered SnO_2 thin films (10 nm), uniform spin-coated SnO_2 nanoparticle coatings (10 to 15 nm), and conformal sol-gel[215] deposited SnO_2 QD films (approximately 5 nm), to identify the optimal ETL template for subsequent nanostructure growth. Figure 4.7 presents SEM images of the SnO_2 nanostructures synthesized on each of the three seed layer templates, illustrating how the underlying interlayer influences rod alignment, packing density, and bundle morphology.

Compared with the SnO_2 nanostructure samples developed on FTO without a seed layer, it is evident that all three seed layer templates promoted the vertical alignment of nanorods and markedly increased array density. However, such structures need appropriate inter-rod void volume to guarantee uniform perovskite penetration. The arrangement of

perovskite grains incorporated within SnO_2 NAs enhances the interfacial surface, allowing the efficient transport of photogenerated electrons between the ETM and perovskite material before carrier recombination occurs. Among all three seed layers, only the magnetron-sputtered SnO_2 thin film enabled the growth of nanorod architectures with ample free volume (Figure 4.7 a,b).

Furthermore, compared with the other seed layers, the magnetron-sputtered sample produces SnO_2 nanostructures with larger diameters, merging in thick bundles. Meanwhile, the SnO_2 QD sample acts as uniformly dispersed nucleation sites, driving the formation of densely packed, ultrathin nanorods that maximize structural density (Figure 4.7 e,f). Figure 4.7c,d shows the SEM image of the sample with the SnO_2 nanoparticle seed layer, exhibiting a larger diameter with reduced compactness. It is posited that the dimensions of the SnO_2 seed particles dictate the nucleation density of the nanostructures. Nonetheless, it is necessary to further vary the concentrations of SnO_2 QDs and nanoparticles in the seed layer to explore their effect on the morphology of the nanomaterial.

The collected data on nanostructure length is presented in Table 4.4. Among the evaluated templates, the magnetron-sputtered SnO_2 seed layer proved the most advantageous variant, with vertically aligned nanostructures and inter-rod void volume.

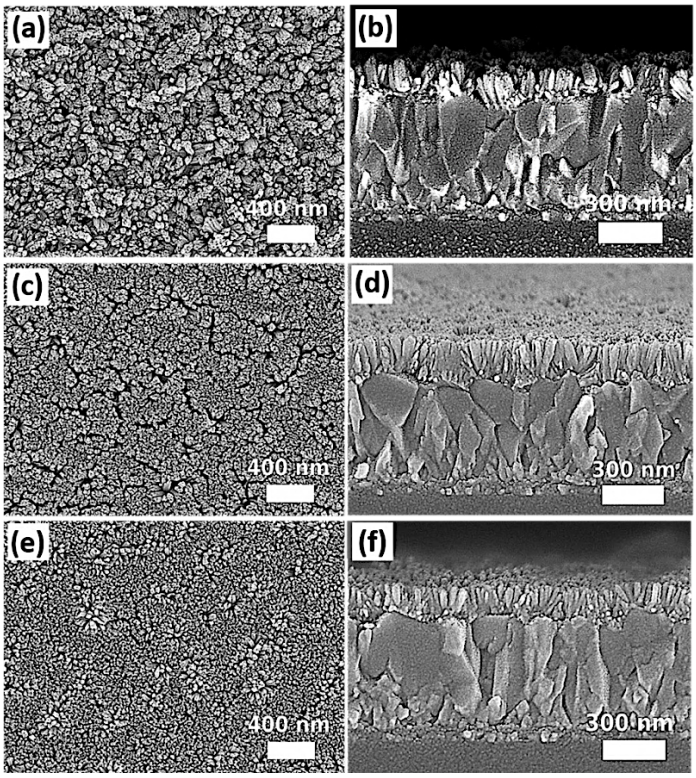

Figure 4.7 Top-view and cross-sectional SEM images of SnO_2 nanostructures grown on different seed layers: (a,b) magnetron-sputtered SnO_2 thin film, (c,d) spin-coated SnO_2 nanoparticle layer, and (e,f) sol-gel-deposited SnO_2 QD film; reproduced from Ref[209] under CC BY 4.0

Table 4.4 Summary of the nanostructure lengths and bundle diameters obtained using different seed layers. Adapted from Ref[209] under CC BY 4.0

Condition	Length of nanostructure		
	Min (nm)	Max (nm)	Mean ± SD
Magnetron-sputtered SnO_2	104	155	128±14
SnO_2 nanoparticle coating	102	200	164±26
SnO_2 QD film	72	136	109±16

4.3.5 Effect of Glacial Acetic Acid

The impact of acetic acid on the nanostructure morphology was assessed using the magnetron-sputtered seed layer and different concentrations of CH_3COOH: 6, 6.5, and 9.75 mL. Figure 4.8 illustrates that lower acetic acid concentrations promote the growth of larger, elongated nanorod bundles. Acetic acid functions as a ligand; CH_3COO^- ions coordinate with Sn^{4+} centers, hindering hydrolysis and nucleation. During solvothermal growth, both acetic acid and its byproduct, ethyl acetate, serve as organic ligands that facilitate the formation of

well-defined tetragonal SnO_2 nanorods and help prevent the bundling of these nanorods. Thus, our findings are consistent with the previously proposed mechanism[212]. The SEM images (Figure 4.8) reveal that the lengths of SnO_2 nanorods synthesized with 6 or 6.5 mL of acetic acid are considerably longer than those produced using 9.75 mL of acetic acid, which is likely due to a higher hydrolysis rate during solvothermal growth resulting from the lower acetic acid concentration. Conversely, when 6 mL of acetic acid was used, the SnO_2 nanorods clustered together to create larger bundles, as shown in Figure 4.8a,b. Increasing the acetic acid volume from 6 to 6.5 mL considerably reduced the size of the SnO_2 bundles, creating more available space between the nanostructures (Figure 4.8c,d). Further increasing the amount of acetic acid to 9.75 mL led to a clearer distinction between the SnO_2 nanorods, which became more separated from one another, and their lengths were the shortest (80 ± 17 nm) compared with those obtained using lower acetic acid concentrations.

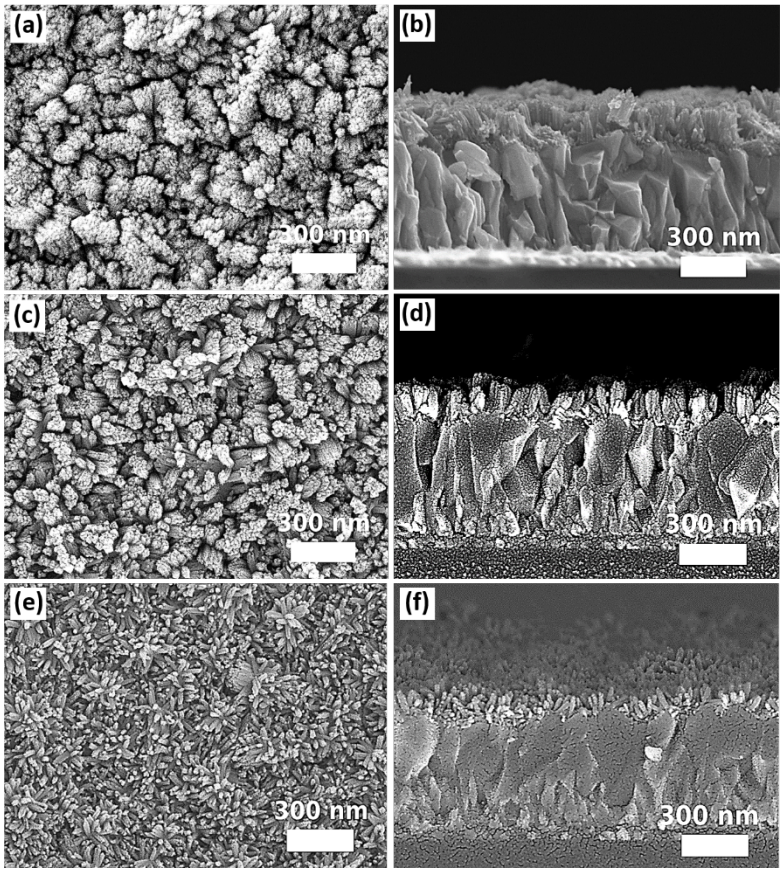

Figure 4.8 Top-view and cross-sectional SEM images of SnO_2 nanostructures synthesized using different acetic acid contents: (a,b) 6 mL, (c,d) 6.5 mL, and (e,f) 9.75 mL; reproduced from Ref[209] under CC BY 4.0

Table 4.5 presents length data for the SnO_2 nanostructures obtained using different acetic acid concentrations. Beyond its direct impact on rod morphology, the acetic acid also alters the total volume of the precursor solution, thereby affecting the pressure. However, the associated pressure shift between 6 and 9.75 mL acid has a negligible impact on morphology relative to the substantial pressure-driven changes observed in our reactor-volume study. Consequently, the acetic acid concentration emerges as the primary lever for fine-tuning morphology under constant thermal and pressure conditions.

Table 4.5 Summary of the nanostructure lengths and bundle diameters obtained using different acetic acid concentrations. Adapted from Ref[209] under CC BY 4.0

Condition	Length of nanostructure		
	Min (nm)	Max (nm)	Mean ± SD
6 mL	91	151	119±16
6.5 mL	105	153	128±13
9.75 mL	55	119	80±17

4.3.6 Effect of Growth Time

The impact of growth time on SnO_2 nanorod formation was evaluated by performing isothermal synthesis at 200 °C for 6, 12, and 24 h. A supplementary experiment comprised an initial 12 h growth period, followed by replacement of the spent precursor with fresh solution and an additional 12 h reaction period. Comparative analysis of the SEM images (Figure 4.9a–f) shows that prolonged reaction times do not alter the general array architecture or average rod length. Conversely, when a two-step approach (12h+12h) is employed with precursor renewal, the resulting SnO_2 nanostructures become denser, featuring larger bundles of nanorods. Additionally, the length of the nanostructure shows an approximate increase of 1.7 times (219 ± 49 nm), in contrast to one-step approaches (~120–130 ± 15 nm). Table 4.6 lists the data of the nanorod structures obtained using different growth times.

SnO_2 nanostructures grown via a single solvothermal cycle exhibit negligible length variation beyond 6 h. It is thought that the lack of sensitivity of SnO_2 nanostructures to variations in growth duration during the one-step solvothermal growth process is influenced

by other limiting factors, such as the overall concentration of various solutes in the precursor solution. The experiments indicate that it is difficult to adjust the length of the nanorods independently while maintaining the required density and dimensions of the SnO_2 nanorods/bundles.

From a device fabrication perspective, this tunability is particularly important, as SnO_2 nanorod length plays a critical role in determining photovoltaic performance. Consistent with the observations reported by Lv et al.,[202] device performance shows a non-monotonic dependence on SnO_2 nanorod length, as controlled by reaction time. The photovoltaic performance initially improves with increasing nanorod length and subsequently deteriorates at longer growth times. The champion device, based on uniform one-dimensional SnO_2 nanorod arrays with an average length of approximately 150 nm, achieves a peak PCE of 16.7%. This enhancement is attributed to increased perovskite loading and improved interfacial contact, which facilitate efficient charge extraction. However, further elongation of the nanorods to ~200 nm (diameter ~70 nm) leads to a reduction in PCE. Excessively long nanorods increase the electron transport distance within the ETL and enlarge the interfacial area exposed to defect states, thereby enhancing trap-assisted recombination. In addition, prolonged growth results in nanorod bundling and non-uniform perovskite infiltration, creating local voids and poorly contacted regions that further increase recombination losses.

Future research should focus on exploring various combinations of experimental conditions. Despite these complexities, these findings establish a robust baseline for correlating solvothermal conditions with the resulting SnO_2 nanorod architecture, thereby guiding the rational design of ETL morphologies for high-quality PSCs.

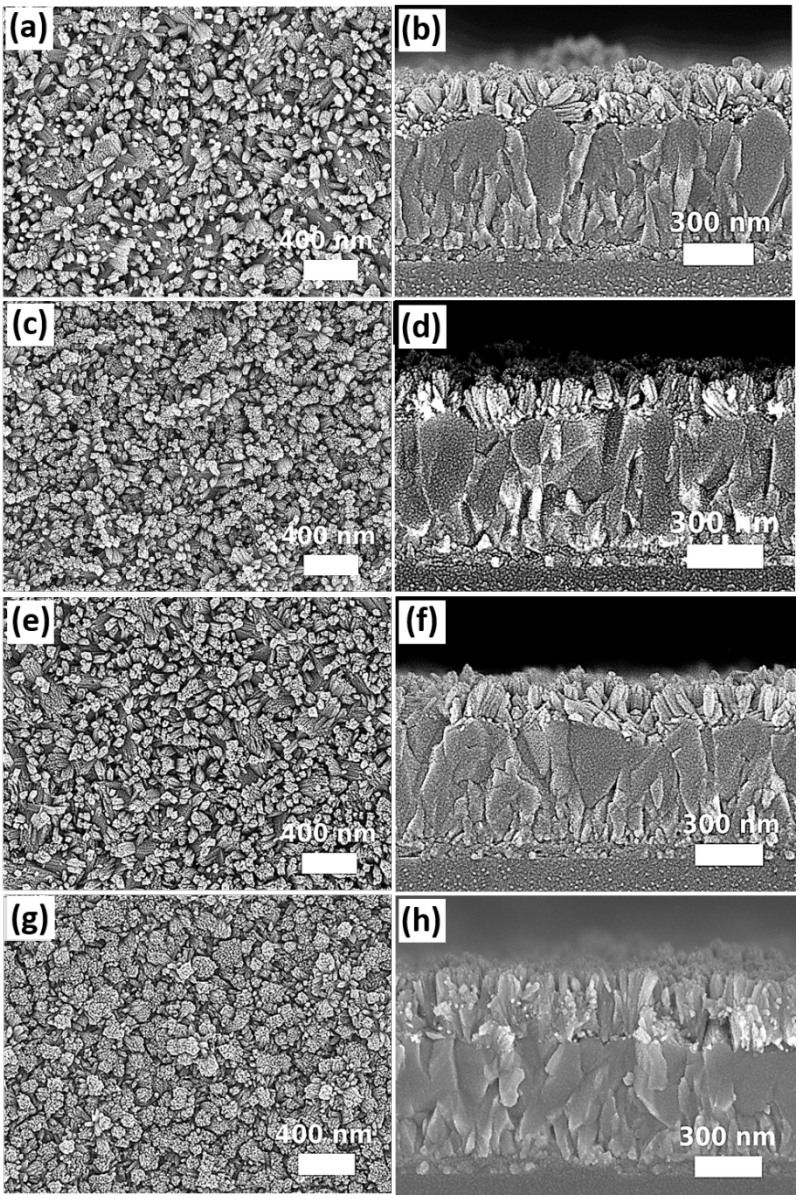

Figure 4.9 Top-view and cross-sectional SEM images of SnO_2 nanostructures synthesized using different growth durations: (a,b) 6 h, (c,d) 12 h, (e,f) 24 h, and (g,h) 12 + 12 h (two-step approach); reproduced from Ref[209] under CC BY 4.0

Table 4.6 Summary of the nanostructure lengths and bundle diameters obtained using different growth durations. Adapted from Ref[209] under CC BY 4.0

Condition	Length of nanostructure			Diameter of SnO_2 bundle		
	Min (nm)	Max (nm)	Mean ± SD	Min (nm)	Max (nm)	Mean ± SD
6 h	83	138	119±14	37	109	62±22
12 h	101	153	129±16	45	91	65±11
24 h	97	154	130±15	39	146	79±33
12+12 h	131	312	219±49	56	202	109±40

4.4 Structural and Photovoltaic Characterization

Prior to integrating the SnO_2 NAs as an ETL in PSCs to evaluate device performance, XRD

analysis was performed to confirm the crystallographic phase and purity of the solvothermal-grown structures. The diffraction patterns (Figure 4.10a) display peaks corresponding to the SnO_2 material and are consistent with the reference.[216] Figure 4.10b shows that PSCs incorporating oxygen plasma-treated SnO_2 ETLs exhibit notably improved PV characteristics compared with untreated devices; the V_{oc} rises from 0.96 to 1.11 V, and PCE increases from 13.3% to 16.6%. The improvement in device performance is attributed to the elimination of organic residues from the surface of SnO_2 nanostructures. This observation underscores the significance of using appropriate surface treatments on solvothermal synthesized SnO_2 nanostructures for the development of PSCs. Figure 4.11 illustrates the device architecture with the nanostructured ETL.

a) b)

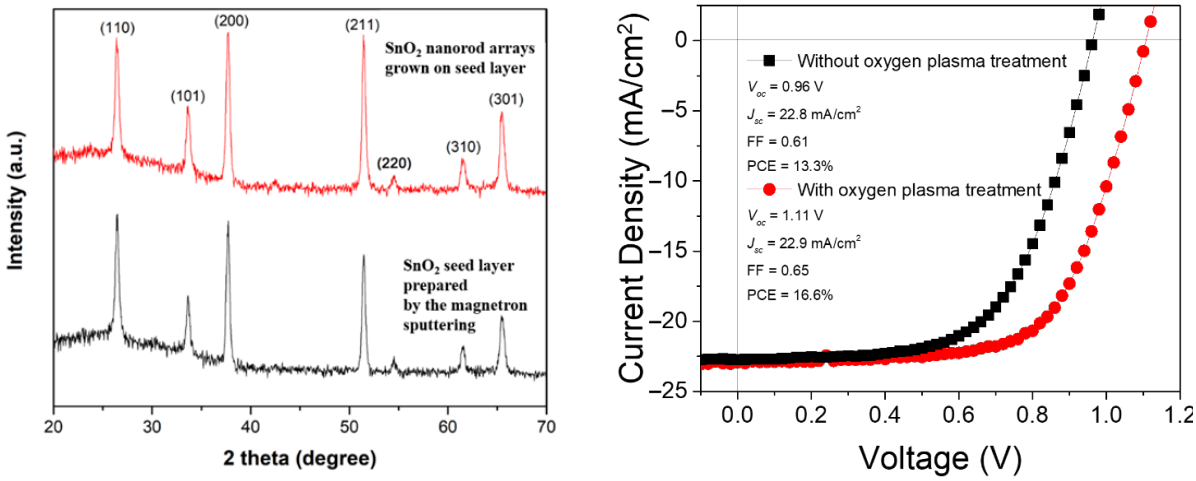

Figure 4.10 a) XRD patterns of the magnetron-sputtered compact ETL and SnO_2 nanostructure and the b) *J-V* characteristics of devices prepared with and without oxygen plasma-treated ETLs; reproduced from Ref[209] under CC BY 4.0

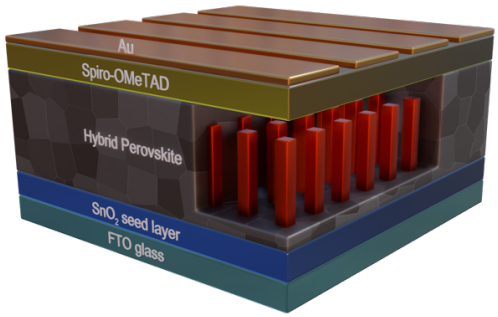

Figure 4.11 The fully assembled device with the nanostructured ETL

The intimate interaction between SnO_2 nanostructured ETL morphology and perovskite crystallization dynamics is critical. It necessitates tailored adjustment of perovskite formulation, deposition parameters, and interfacial engineering for each nanorod configuration to achieve optimal charge extraction and long-term stability. Advanced interfacial treatments, such as SAMs, ultrathin passivation coatings, or selective ligand exchange, can further enhance band alignment and suppress interfacial recombination. Although these targeted interface engineering strategies are essential for maximizing device efficiency and operational stability, their systematic exploration lies beyond the scope of this thesis and represents a compelling avenue for future research.

4.5 Summary

In conclusion, the role of interfacial engineering in SnO_2 nanostructure morphology has been systematically investigated for PSCs. Morphological features such as nanorod length, diameter, alignment, and surface area influence key factors like charge extraction, interface quality, and recombination dynamics. For this reason, precise control of the SnO_2 nanorod architecture is essential for effective device performance. A comprehensive investigation of the solvothermal growth conditions, namely autogenous pressure, substrate orientation, DI water-to-ethanol ratio, seed layer architecture, acetic acid concentration, and growth time, provided a framework for tailoring SnO_2 NAs. For example, several solvothermal growth parameters govern the diameter of SnO_2 nanorods. Increased pressure during solvothermal synthesis promotes crystallite growth, leading to larger grain sizes. The characteristics of the seed layer strongly influence nanorod morphology, with SnO_2 quantum-dot seed layers producing nanorods with the highest density and the smallest diameters due to enhanced nucleation. Solvent composition also plays an important role, as a high ethanol content in the DI water–ethanol mixture leads to lateral aggregation and bundle formation. The orientation was primarily controlled by the seed layer. SnO_2 nanorods grown on three different seed layers tend to align along a single direction perpendicular to the substrate, indicating that the

seed layer provides crystallographic guidance for vertical growth.

Thus, this work furnishes a set of actionable guidelines for the rational design of SnO_2 nanorod ETLs in PSCs. Differing reactor volumes with a fixed precursor volume generated distinct internal pressures and altered the SnO_2 nanorod morphologies. Equalizing the filling ratio across all reactors standardized the pressure and produced identical structures, confirming that pressure is the primary growth parameter. Substrate orientation plays a supporting role, with a horizontal face-down configuration guaranteeing complete precursor coverage and uniform vertical growth. Solvent engineering is also critical; using an equal ratio of DI water to ethanol optimizes hydrolysis kinetics, and a compact magnetron-sputtered interlayer seeds tight, vertically aligned rod assembly. The strategic modulation of acetic acid levels coupled with a sequential solvothermal approach further enhances the nanorod length and bundle spacing. Crucially, post-growth oxygen plasma cleaning removes organic residues, passivates interfacial traps, and improves the V_{oc} and efficiency, offering a robust blueprint for high-performance perovskite device fabrication. Overall, these findings establish practical design principles for the application of SnO_2 NAs in ETLs and offer a clear roadmap for future researchers aiming to optimize ETL/perovskite interfaces and boost device performance.

CHAPTER 5: ENGINEERING A MAGNESIUM OXIDE INTERLAYER TO ENHANCE THE STABILITY OF ALL-INORGANIC PSCs

5.1 Introduction

All-inorganic perovskites offer key advantages over their organic-inorganic counterparts, including enhanced thermal stability at elevated temperatures and improved moisture tolerance afforded by fully inorganic A-site cations. In contrast, organic cations such as MA^+ begin to volatilize and decompose at ~80 °C, highlighting their limited thermal stability.[217–219] Meanwhile, the bulkier FA^+ cation induces significant lattice strain, elevating the defect density and accelerating halide ion migration. Compounding this, pure α-$FAPbI_3$ transitions to its non-photoactive δ-phase with a wide bandgap (~2.4 eV) at a temperature below approximately 150 °C, thereby losing its PV activity.[220,221] Moreover, exposure to environmental stressors such as heat, humidity, and light, accelerates the degradation of hybrid PSCs.

Consequently, significant research has been devoted to replacing organic A-site cations with Cs to develop fully inorganic perovskite-based solar cells. These PSCs exhibit lower photosensitivity, conferring greater stability under continuous 1-sun illumination, and a wider bandgap enables higher V_{oc} values.[218] Cubic α-$CsPbI_3$ has attracted considerable interest owing to its optimal bandgap of 1.73 eV,[217,218] which provides strong absorption across the visible spectrum. Unfortunately, this phase only remains thermodynamically stable above ~300 °C,[222] when the room-temperature yellow δ phase (E_g = 2.82 eV[218,222]) irreversibly converts into a black perovskite form. Upon cooling, the structure does not revert directly to δ but instead passes through two intermediate black phases: a β phase at 260 °C[223] and an orthorhombic γ phase at 175 °C.[223] Notably, the yellow δ phase recovers after several days at room temperature.[223] Efforts to address the thermal and structural instabilities of $CsPbI_3$ have led to the development of cesium bromide and mixed halogen perovskites,

particularly $CsPbBr_3$ and $CsPbIBr_2$. $CsPbBr_3$ exhibits stable perovskite structures at ambient conditions and resists phase transitions; however, the wide bandgap (2.37 eV)[224,225] limits the absorption of low-energy photons from the solar spectrum, thereby restricting the maximum current density and overall efficiency of single-junction solar cells. Although $CsPbIBr_2$ has a narrower bandgap (~2.05 eV)[226] than $CsPbBr_3$, its thin films are susceptible to moisture-driven conversion from the photoactive cubic-phase to a non-perovskite orthorhombic phase.[227] This phase transition undermines the film integrity, charge transport, and long-term device stability. Among these inorganic absorbers, $CsPbI_2Br$ exhibits an intermediate bandgap of approximately 1.9 eV, ensuring extensive solar absorption and an elevated V_{oc}. Advancements in deposition methodologies, defect passivation, and interfacial engineering have enhanced $CsPbI_2Br$ device performance, increasing the PCE from an initial 9.8%[228] to a record 17.5%.[229]

Despite marked advances in phase stabilization, $CsPbI_2Br$ remains susceptible to stability issues, underscoring the need for innovative interfacial engineering strategies. First, the choice and optimization of a suitable ETL is crucial. Although TiO_2 is the most commonly used ETM, these devices suffer from photocatalytic degradation of perovskites during extended exposure to light, high recombination rates caused by low electron mobility (<1 $cm^2\ V^{-1}s^{-1}$),[194] and energy-demanding high-temperature sintering processes. Meanwhile, ZnO combines high chemical and mechanical stability with non-toxicity and natural abundance.[197] Given the significant optical transmission in the visible light spectrum, ZnO has garnered attention for various technological uses. For example, ZnO is a compelling ETL alternative, with a band gap of approximately 3.37 eV[196,197] and significantly high electron mobility of 100–200 $cm^2\ V^{-1}s^{-1}$. Additionally, the low-temperature production of ZnO lowers energy consumption during manufacturing and is compatible with flexible substrates. Despite its extensive use in OPV,[230–234] researchers seldom focus on ZnO in PSCs because it can deprotonate[235] the MA^+ and FA^+ cations, leading to the degradation of hybrid PSCs. However, in all-inorganic perovskite devices, the absence of organic ions eliminates this

degradation pathway, allowing ZnO to be leveraged for effective charge extraction while maintaining the integrity of the material.

The CTL/absorber interface significantly influences carrier extraction and transport. Misaligned energy levels at these junctions create potential barriers to charge flow, resulting in heightened recombination and a diminished photocurrent. To counteract these effects, interfacial layers are incorporated to enhance energy alignment,[236–238] promoting efficient charge transfer[239] and reducing energy losses.[238] Additionally, interfacial modifiers act as protective coatings, shielding the perovskite from moisture and oxygen and thereby enhancing device stability.[240] For example, Deng *et al.*[236] and Wang *et al.*[238] enhanced the energy level alignment by employing interfacial engineering; alkali hydroxide and polyethylenimine ethoxylated interlayers were incorporated at the SnO_2/$CsPbI_2Br$ interface, resulting in PCEs of 11.78%[236] and 11.2 %,[238] respectively. Yan *et al.*[239] deployed a sequential SnO_2/ZnO bilayer ETL to reduce energy loss and increase the V_{oc} for high-efficiency $CsPbI_2Br$-based PSCs. Uniform grain morphology and complete substrate coverage of high-quality perovskite films were obtained on the SnO_2/ZnO surface. The higher conduction-band minimum of ZnO creates a cascade energy level alignment with SnO_2 and the $CsPbI_2Br$ absorber, which enhances electron extraction and minimizes trap-assisted recombination.[239] The bilayer ETL devices achieved a V_{oc} of 1.23 V and a PCE of 14.6% and maintained 80% of their initial efficiency after 300 h of annealing at 85 °C, showcasing remarkable thermal stability.[239] Bahadur *et al.*[241] also enhanced the stability by introducing a fluorinated IL, namely 3-(trifluoromethyl) benzylamine molecule to passivate the perovskite surface. The unencapsulated PV cells treated with this molecule exhibited markedly enhanced operational stability, retaining 86.23% of their starting PCE over a prolonged 1440 h aging period at 85 °C in a dry box, compared with just 48.26% for the control device without encapsulation.[241]

Although ZnO is a highly promising ETL for all-inorganic PSCs, its interfacial imperfections, such as inherent defect sites within ZnO and nonuniform coverage of the

perovskite layer, limit performance.[242] These flaws induce deep-level traps and exacerbate interfacial recombination, thereby constraining device efficiency. Modifying the device architecture by introducing ultrathin interlayers or doping can effectively passivate interfacial defects, suppress non-radiative recombination, and enhance overall PV performance. For example, Li *et al.*[243] developed devices utilizing a $PbCl_2$-ZnO hybrid nanocomposite as the ETL, achieving a record PCE of 17.46%; $PbCl_2$ effectively tuned the energy bandgap of ZnO and reduced the defects at the ZnO/$CsPbI_2Br$ interface.[243] These impressive findings underscore the significance of interfacial engineering in enhancing device performance. Meanwhile, Li *et al.*[244] fabricated bilayer ZnO/$Mg_xZn_{1-x}O$ ETLs and replaced traditional Spiro-OMeTAD HTM with poly[(2,6-(4,8-bis(5-(2-ethylhexyl-3-fluoro)thiophen-2-yl)-benzo[1,2-b:4,5-b′]dithiophene))-alt-(5,5-(1′,3′-di-2-thienyl-5′,7′-bis(2-ethylhexyl)benzo[1′,2′-c:4′,5′-c′]dithiophene-4,8-dione))]. The obtained architecture raised the conduction band minimum to more closely match $CsPbI_2Br$, while PM6 aligned energetically with the valence band maximum, streamlining the charge extraction at both interfaces. This dual modification also improved the perovskite crystallinity on the bilayer ETL and reduced interfacial trap densities, reaching a high V_{oc} of 1.34 V and PCE of 16.04%.[244]

The application of MgO has demonstrated significant benefits for interfacial engineering because of wide bandgap (7.8 eV[245]) and chemical stability, though most studies have focused on hybrid PSCs. For example, Cao *et al.*[246] used protonated ethanolamine and a MgO layer as a passivating agent for ZnO in $(CsFAMA)Pb(BrI)_3$-based PSCs. The hysteresis was reduced, and the champion PCE was increased from 18.31 % with a bare ZnO ETL to 21.08% in the optimized device.[246] Meanwhile, Dagar *et al.*[247] achieved 19% PCE for SnO_2/MgO/$CH_3NH_3PbI_3$ compared with 15.2% for SnO_2/$CH_3NH_3PbI_3$, attributing the gain to MgO's effective hole-blocking ability and the subsequent reduction in interfacial recombination.

Although MgO interlayers have markedly improved hybrid PSCs, their integration

into fully inorganic architectures has rarely been investigated. One of the few investigations was conducted by Wang *et al.*[248] They incorporated a MgO interfacial layer at the SnO_2/$CsPbIBr_2$ interface, achieving reduced hysteresis and a notable enhancement in device performance: the V_{oc} increased from 1.25 to 1.36 V while the PCE increased from 10.29% to 11.04%.[248]

While the study by Wang et al.[248] demonstrates the potential of MgO interlayer in SnO_2-based inorganic PSCs, ZnO exhibits fundamentally different electronic structure, surface chemistry, etc. These differences strongly influence interfacial energetics, defect formation, and chemical compatibility with inorganic perovskites, making it inappropriate to directly generalize interfacial engineering methods developed for SnO_2 to ZnO-based systems. Despite ZnO offering favorable cascade energy alignment with $CsPbI_2Br$, the role of MgO at the ZnO/perovskite interface has not been systematically explored. Consequently, the present study fills this knowledge gap by systematically exploring the incorporation of MgO at the ZnO/$CsPbI_2Br$ interface. $CsPbI_2Br$, which possesses a slightly narrower bandgap than $CsPbIBr_2$, is particularly attractive for practical all-inorganic PSCs and for tandem configurations with narrow-bandgap absorbers. Furthermore, the findings of this study reinforce earlier report[249] indicating that a sufficiently large conduction-band offset at the ETM/Cs-based perovskite interface is decisive for efficient electron extraction and simultaneously improves device efficiency and stability. In that work,[249] the authors investigated primarily TiO_2- and SnO_2-based $CsPbI_{1.8}Br_{1.2}$ devices. More importantly, this work goes beyond performance enhancement by analyzing interfacial properties together with systematic assessments of storage stability, operational stability, and PI resistance under conditions relevant to low Earth orbit (LEO). Shelf-life testing showed that the MgO-modified cells maintained 70% of their original efficiency value after 49 days of storage in the glovebox, compared with only 55% retention for the control devices. We exposed both device types to low-energy PI tests to evaluate the durability under extreme radiation conditions. Notably, the optimized MgO-incorporated devices exhibited markedly high-

performance retention, maintaining 100% of their initial PCE for 77 days, whereas the efficiency of the control cells dropped to 47% of its original value. The results clearly show that MgO modification substantially improves both material durability and device stability, even under PI exposure. In contrast to other reported interfacial engineering approaches that rely on complex or costly fabrication techniques (such as passivation layers grown by atomic layer deposition or vacuum-deposited interlayers), the MgO layer employed here is introduced through a straightforward solution-based method. This simplicity provides significant advantages for scalable and low-cost manufacturing of PSCs.

5.2 Device Fabrication

Two device configurations were fabricated: FTO/ZnO/$CsPbI_2Br$/Spiro-OMeTAD/Au and FTO/ZnO/MgO/$CsPbI_2Br$/Spiro-OMeTAD/Au. Prior to deposition, all FTO-coated substrates were cleaned according to the protocol detailed in Chapter 3.2.1. The HTL was deposited as described in Chapter 3.2.2, and Au contacts were evaporated according to the procedure outlined in Chapter 3.2.3.

5.2.1 ETL Deposition

After a 10 min of sonication, the ZnO ink solution was filtered. The deposition process was applied by spin-coating at 8000 rpm for 30 s on cleaned FTO substrates, which were subsequently annealed on a hot plate at 130 °C for 20 min.

5.2.2 MgO Interlayer Recipe

A homogeneous MgO precursor solution was obtained by dissolving 36.45 mg of magnesium acetate tetrahydrate in 1.7 mL of 2-methoxyethanol with the addition of 1 μL of ethanolamine, followed by continuous stirring for 5 h. ZnO-coated FTO substrates were exposed to UV-ozone for 10 min before deposition. MgO solution was deposited by spin-

coating at 8000 rpm for 30 s. The films were then subjected to a 30 min of annealing at 450 °C.

5.2.3 $CsPbI_2Br$ Perovskite Deposition

The $CsPbI_2Br$ precursor solution was prepared by combining 233.8 mg of CsI, 207.45 mg of PbI_2, and 165.15 mg of $PbBr_2$ in a mixed solvent system using a DMF:DMSO ratio of 800:200. For optimal film adhesion and a clean surface, ETL-coated substrates were subjected to UV-ozone treatment for 10 min. Within a nitrogen-filled glovebox, the perovskite was deposited employing a two-stage spin-coating program: 1000 rpm for 10 s, followed by 5000 rpm for 30 s to uniformly spread the solution. Additionally, 160 µl of IPA was introduced as an antisolvent 15 s before the spin-coating process concluded. The films were then heated at 40 °C for 2 min to nucleate the perovskite phase, as evidenced by a brown color, followed by an extra 10 min at 250 °C to complete the crystal growth and densify the film.

5.2.4 EOD Fabrication Methodology

To probe the electron transport independently, EODs were constructed with an ETL/perovskite/PCBM/Ag architecture. After depositing the ETL (Chapters 5.2.1, 5.2.2) and perovskite (Chapter 5.2.3) layers, a 10 mg mL^{-1} PCBM solution in CB was spin-coated at 3000 rpm for 30 s and then annealed at 100 °C for 10 min. Finally, high-purity silver electrodes (~70 nm) were thermally evaporated under high vacuum to complete the device fabrication.

5.3 Results & Discussions

5.3.1 ETL Investigation

First, the investigation started with a comprehensive analysis of the ETM layers using SEM, EDS, AFM, and KPFM characterization techniques. The morphology of ZnO- and

ZnO/MgO-coated substrates was examined by SEM, as shown in Figure 5.1a,b. Both conditions demonstrate nearly identical crystallite sizes and surface textures, suggesting that adding the MgO thin film does not alter the ZnO crystallites. Quantitative analysis of SEM cross-sections in FIJI revealed that ZnO and ZnO/MgO films maintain comparable thicknesses of 70.6 ± 14.3 and 70.2 ± 14.5 nm, respectively. Maintaining a similar ETL thickness upon MgO incorporation offers a significant advantage because an excessively thick MgO layer can act as an insulator owing to its low conductivity, thus increasing the series resistance and degrading device performance.[250] Guo *et al.*[251] reported that a thick MgO layer may also reduce the perovskite light absorption, in addition to obstructing electron transport.

EDS was used to assess material purity, identify contaminants, and analyze the elemental composition of ETL-coated substrates. Figure 5.1c,d shows the EDS spectra obtained for the two ETL samples, confirming the presence of MgO in the ZnO/MgO sample, whereas no Mg-related signal was detected for the control sample.

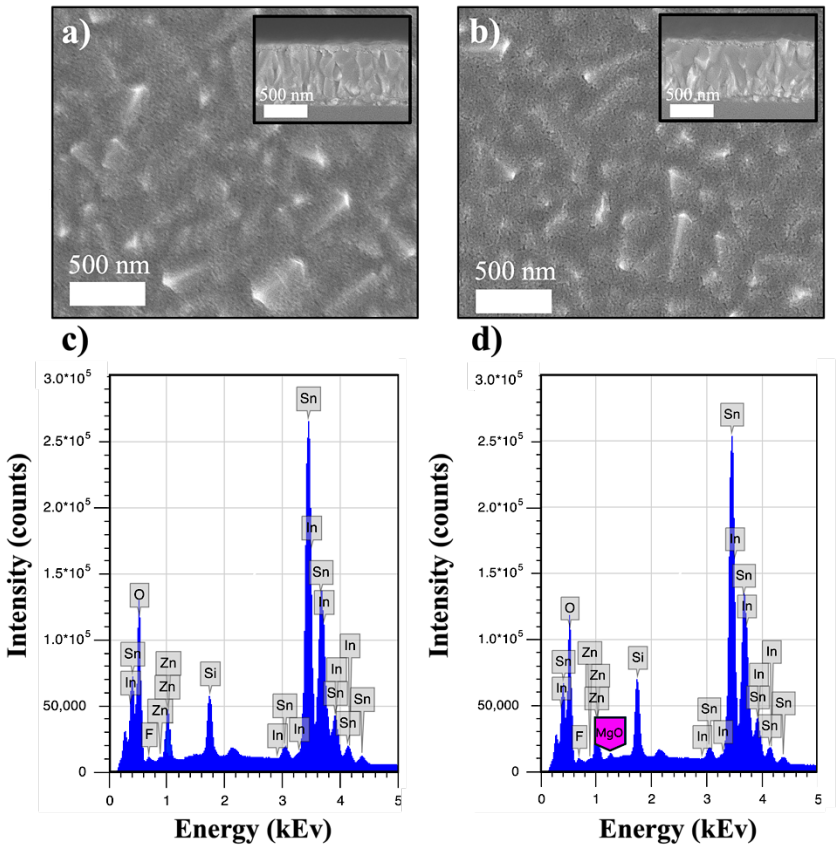

Figure 5.1 Top-view and cross-sectional SEM images of a) ZnO and b) ZnO/MgO; EDS spectra of c) ZnO and d) ZnO/MgO. Adapted from Ref[252] under CC BY 4.0

AFM scans (3 µm × 3 µm) provided quantitative surface-roughness values for the ETL films. The ZnO layer (Figure 5.2a) exhibited an RMS roughness of 15.29 ± 0.32 nm, whereas the ZnO/MgO (Figure 5.2b) was slightly higher, increasing to 18.01 ± 1.18 nm. While the KPFM tool was used to investigate the surface potential and quantify the CPD between the probe and the ETL films. Figures 5.2c,d present KPFM maps over a 3 × 3 µm scan area, with the corresponding 3D representations shown as insets.

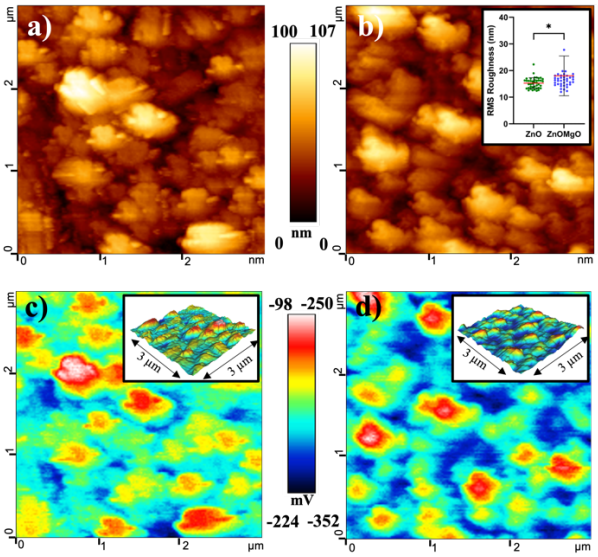

Figure 5.2 AFM height-mode surface-roughness maps for (a) ZnO and (b) ZnO/MgO ETLs, with RMS roughness statistics displayed in the inset. KPFM surface-potential images with 3D topography insets for c) ZnO and d) ZnO/MgO ETLs. Adapted from Ref[252] under CC BY 4.0

The box charts shown in Figure 5.3a–d represent the statistical data for four key KPFM-derived metrics: surface potential, peak-to-valley V_{CPD}, RMS V_{CPD}, and WF parameters. The ZnO layer exhibited a V_{CPD} of –20.46 ± 25.58 mV, whereas the ZnO/MgO sample showed a pronounced shift to –285.00 ± 10.06 mV. A considerable shift in V_{CPD} suggests that the surface electrical properties have been significantly altered following the deposition of MgO. Extensive data analysis was conducted to evaluate the significance of the differences in surface potential by analyzing peak-to-valley V_{CPD} and RMS V_{CPD} parameters. The peak-to-valley V_{CPD} (Figure 5.3b), which indicates the range of variations in surface potential, exhibits a slight increase from 120.9 ± 3.3 mV in the ZnO sample to 132.9 ± 5.5 mV in the MgO-modified sample, and the RMS V_{CPD} increases from 18.07 ±

0.49 to 20.51 ± 0.98 mV with the addition of MgO. These modest shifts suggest a slightly wider range of local surface potentials, but they remain small and statistically negligible. While incorporating MgO causes a pronounced shift in the absolute V_{CPD} by modifying the ZnO WF, it does not compromise surface uniformity, supporting uniform ETL charge transport.

The WF (Figure 5.3d) increases from 5.39 ± 0.03 eV for ZnO to 5.6 ± 0.01 eV for ZnO/MgO. The WF values were determined using the following formula:[253]

$$V_{CPD} = \frac{\Phi_{tip} - \Phi_{sample}}{e} \tag{5.1}$$

where Φ_{tip} and Φ_{sample} indicate the tip and sample WFs, and e is the elementary charge.[253]

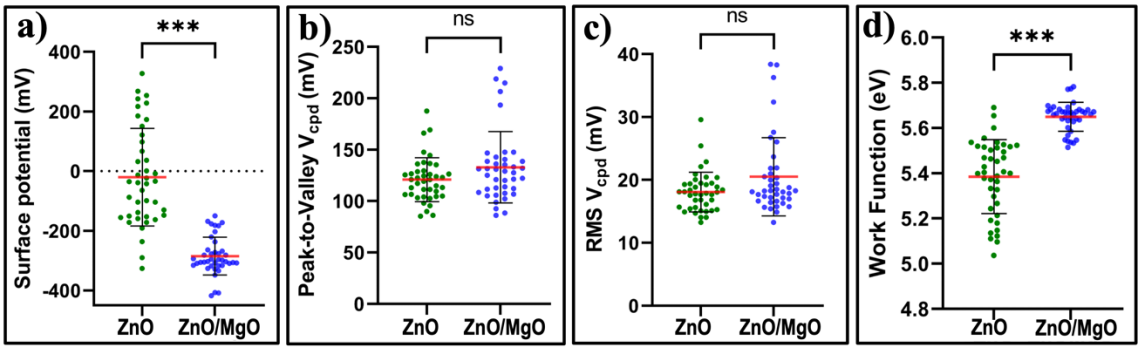

Figure 5.3 Box plots of the statistical distributions for the a) surface potential, b) peak-to-valley V_{CPD}, c) RMS V_{CPD}, and d) WF. Adapted from Ref[252] under CC BY 4.0

XRD was employed to verify the coexistence of ZnO and MgO. As shown in Figure 5.4a, both the pristine ZnO and the MgO-coated samples exhibit diffraction peaks at 34.5°, 36.0°, and 56.5°, corresponding to the (002), (101), and (110) planes[254] of typical ZnO. A pronounced diffraction peak at 44.0° is also observed for the optimized sample, which corresponds to the characteristic crystallographic plane (200)[250,255] of MgO material. It is important to note that adding MgO did not diminish the transmittance of the samples (Figure 5.4b), indicating that the MgO layer does not contribute to optical energy loss when integrated into solar cells. Corresponding absorbance spectra (Figure 5.4c) show a slight increase in absorbance of the MgO-modified sample, likely due to modified surface states. From Tauc plots, both conditions demonstrate the same E_g values of 3.2 eV.

Following structural and optical characterization by XRD and UV-Vis spectroscopy, XPS was employed to probe the chemical composition and electronic states of the ZnO and ZnO/MgO films. The Mg 1s peak observed at a BE of 1305.07 eV confirms the presence of MgO, as illustrated in Figure 5.4d. XPS analysis of the Zn 2p core levels of Zn $2p_{1/2}$ and Zn $2p_{3/2}$ located at 1044 and 1022 eV indicates a slight shift to lower BE, accompanied by a reduced peak intensity for the MgO-modified films (Figure 5.4e). This downward shift likely attributed to the MgO overlayer partially obstructing the ZnO surface signal. This change may indicate the interfacial electronic interactions between ZnO and MgO, reflecting an increased electron concentration at the ETL surface due to the MgO overlayer. Such interfacial charge redistribution could play a significant role in adjusting the energy band alignment and potentially enhancing carrier transport in PSCs. More specifically, it indicates a decrease in the electron-withdrawing effect around Zn due to changes in the local electronic environment following the substitution of Zn^{2+} with Mg^{2+}. Although both materials have comparable ionic radii, the slightly higher electropositivity of Mg^{2+} modifies the interfacial electronic structure.

Figure 5.4f presents the O 1s XPS spectrum for the ZnO sample. The O_I peak at 530.0 eV corresponds to O^{2-} ions in the stoichiometric wurtzite ZnO structure, where oxygen is coordinated within the Zn-O framework. Additionally, it encompasses fully oxidized oxygen species associated with the surrounding metal-oxygen (M-O) environment. The O_{II} peak at 531.0 eV is associated with oxygen vacancies, and the O_{III} peak at 532.0 eV corresponds to surface hydroxyl (-OH) species. Following the incorporation of MgO on the ZnO surface, all three peaks exhibited a shift, appearing at 529.8 eV (O_I), 531.6 eV (O_{II}), and 532.8 eV (O_{III}), respectively, as illustrated in Figure 5.4g. The enhancement of the O_{II} peak can be attributed to the lattice mismatch and the resulting interfacial strain between the cubic structure of MgO and the hexagonal structure of ZnO. In contrast, the reduced intensity of the O_{III} peak suggests a lower propensity for hydroxylation in optimized films, likely due to MgO's weaker affinity for -OH group adsorption. Additionally, this decrease may be

attributed to the participation of M-OH species in ZnO–MgO interfacial interactions, which reduces the number of free surface -OH groups. Moreover, the MgO-incorporated sample demonstrates the shift of the O_I peak to lower BE, reflecting alterations in the local chemical environment. The increased ionic character of Mg-O bonds diminishes the electron-withdrawing influence on neighboring oxygen atoms. This observation is consistent with the parallel shift detected in the Zn 2p core-level spectra.

UPS was performed to investigate the influence of MgO on the positions of energy levels. By linear extrapolation, the secondary electron cutoff ($E_{cut\text{-}off}$) and the valence band region ($E_{VBM} - E_f$) were determined, as presented in Figure 5.4 h,i. The Fermi energy was calculated using the formula $E_f = 21.22$ eV (He I) $- E_{cut\text{-}off}$. With E_f established, the valence band maximum (E_{VBM}) was then obtained. The conduction band minimum (E_{CBM}) was calculated by summing the valence band maximum (E_{VBM}) and the optical bandgap (E_g).

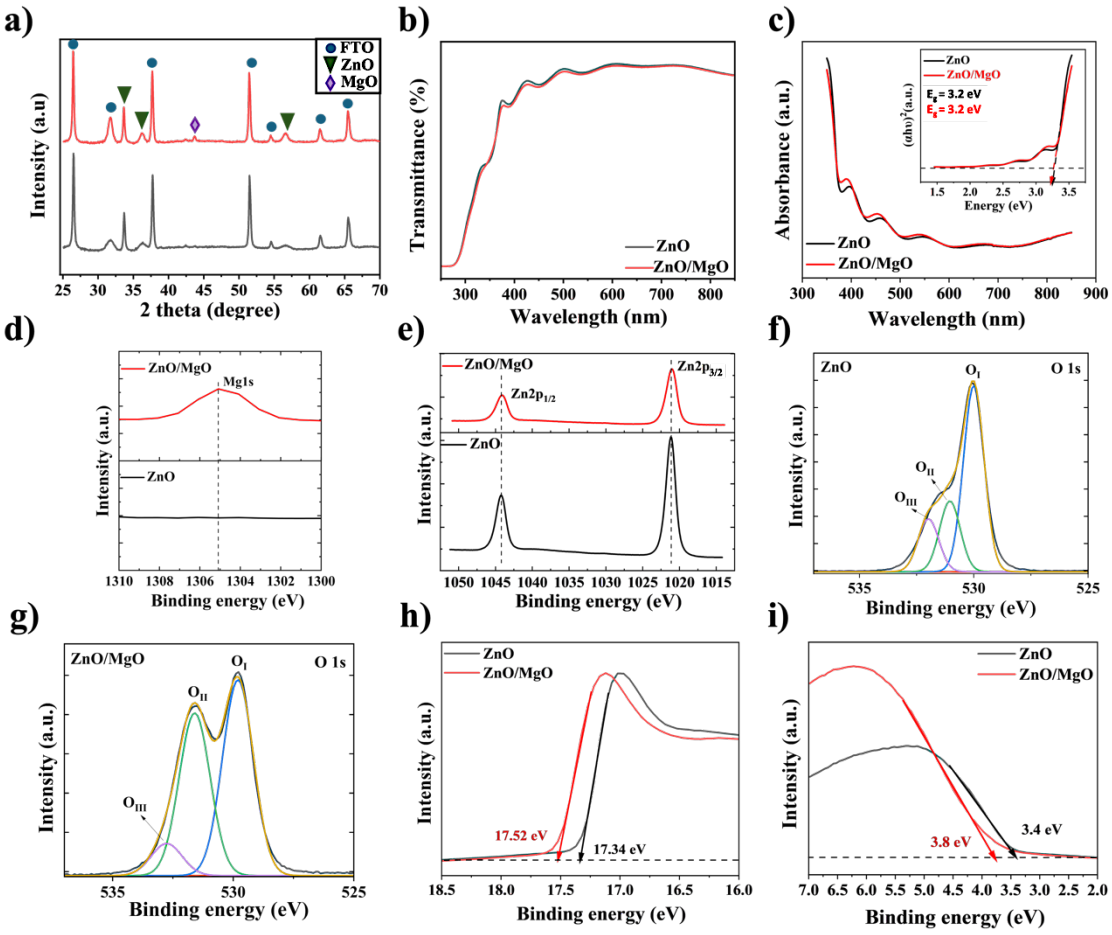

Figure 5.4 a) XRD patterns of the ZnO and ZnO/MgO thin films on FTO glass substrates; UV-Vis b) transmittance and c) absorbance spectra; high-resolution XPS spectra comparing ZnO and ZnO/MgO samples: (d) Mg 1s, (e) Zn $2p_{1/2}$ and $2p_{3/2}$, (f,g) O

1s orbitals; UPS-derived BE profiles showing the h) secondary $E_{cut\text{-}off}$ and i) valence band region for ZnO versus ZnO/MgO. Adapted from Ref[252] under CC BY 4.0

Figure 5.5 presents a schematic energy band diagram with the experimentally determined CBM and valence band maximum positions. The introduction of MgO shifts the E_{CBM} from –4.1 to –4.3 eV, thereby creating a more gradual energy-level gradient that facilitates electron transport and collection at the FTO electrode, consistent with reduced recombination according to energy band-alignment principles. Additionally, the deeper valence band position confirms the n-type character of the MgO-modified ETL, which agrees with the observed increase in electron density.[256] Furthermore, introducing MgO results in a greater CBM energy offset at the ETL/perovskite interface. Consistent with earlier studies,[249] such an offset is advantageous in Cs-based PSCs because it promotes exciton dissociation and facilitates efficient electron extraction.

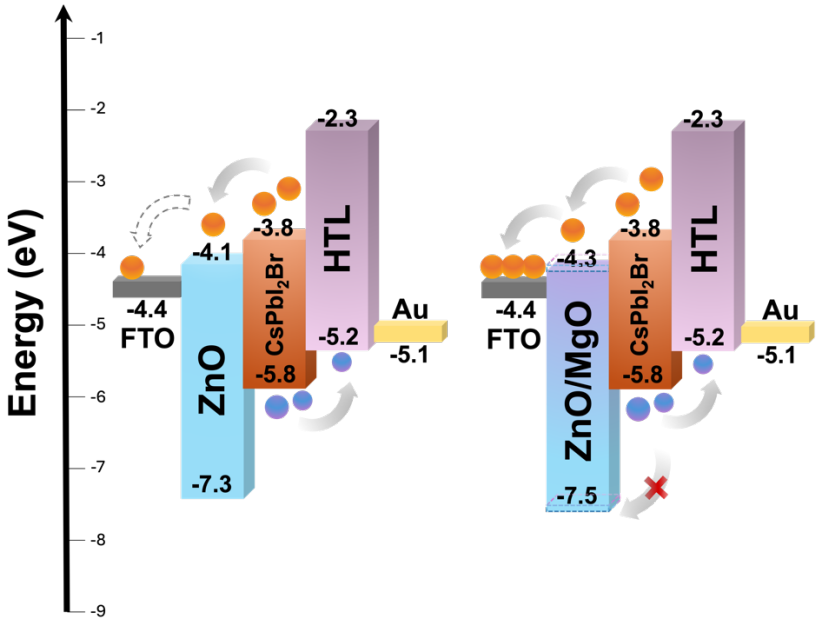

Figure 5.5 Schematic energy band diagram. Adapted from Ref[252] under CC BY 4.0

5.3.2 ETL/Perovskite Characterization

Evaluation of the MgO structural and electronic modifications to the ETL was followed by an investigation of its effects on the perovskite film. $CsPbI_2Br$ films were deposited on ZnO-

and ZnO/MgO-coated substrates by spin-coating deposition. SEM and AFM were employed to reveal differences in the grain size, surface coverage, and roughness, as shown in Figure 5.6. Top-view SEM images with grain size distribution plots as insets (Figure 5.6a,c) demonstrate a significant enhancement in the perovskite crystallite dimensions with MgO interlayer incorporation, grain sizes increase from 100–900 nm (mean ~370 nm) in the control film to 200–1600 nm (mean ~600 nm) in the optimized sample. Enhanced grain size[257] growth facilitates more efficient charge-carrier mobility and lowers non-radiative recombination–key factors in boosting PSC efficiency. Additionally, cross-sectional SEM images (Figure 5.6b,d) verify that both films maintain comparable thicknesses — 321 ± 29 nm for the ZnO and 319 ± 22 nm for the ZnO/MgO sample— and exhibit well-defined columnar morphologies.

AFM images (Figure 5.6e,f) further validate these morphological improvements, displaying an apparent increase in the surface grain size for the optimized sample. Control and MgO-modified samples exhibited RMS roughness values of 35 ± 27 and 40 ± 25 nm, respectively. A slight increase in RMS aligns with the roughness trends observed in the ETL-coated substrates, as illustrated in Figure 5.2b. The findings demonstrate that although the ultrathin MgO interlayer slightly alters surface topography, the modification does not compromise perovskite uniformity.

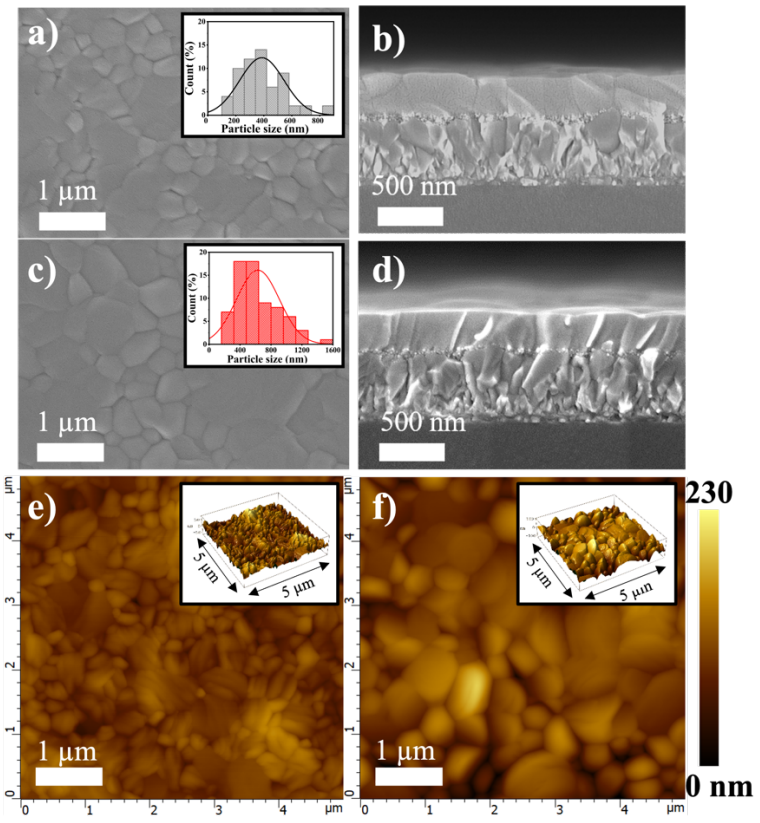

Figure 5.6 Top-view and cross-sectional SEM images with accompanying particle-size distribution histograms for (a, b) ZnO/$CsPbI_2Br$ and (c, d) ZnO/MgO/$CsPbI_2Br$ samples; AFM height-mode and corresponding 3D images for (e) ZnO/$CsPbI_2Br$ and (f) ZnO/MgO/$CsPbI_2Br$ samples, highlighting the surface-topography changes upon MgO incorporation. Reproduced from Ref[252] under CC BY 4.0

To ensure that interface engineering does not affect the intrinsic crystal structure of the absorber, XRD scans were carried out on ZnO/$CsPbI_2Br$ and ZnO/MgO/$CsPbI_2Br$ samples. The measurements were performed in the 2θ range of 10°–70° (Figure 5.7a), showing typical spectra for $CsPbI_2Br$, ZnO, and FTO, which coincide with the peaks found in the literature.[258,259] In both cases, the characteristic perovskite peaks at 14.75°, 20.95°, and 29.7° are assigned to the (100), (110), and (200) planes[260,261] of cubic $CsPbI_2Br$. The absence of any new diffraction features indicates that the MgO layer does not disturb the perovskite crystallinity or phase purity. Additionally, the MgO peak was not observed because of the overpowering signals from the perovskite material.

After XRD confirmation of the phase integrity, the stability evaluation was provided for ETL/perovskite substrates. Stability assessments were performed under two conditions: samples were stored in a controlled-atmosphere glovebox or exposed to ambient air (30 %

RH). Under inert glovebox storage, both the control and MgO-modified devices maintained their structural integrity, showing no significant degradation over the test period, as illustrated in Figure 5.7b. In contrast, samples exposed to ambient air demonstrated markedly different behavior (Figure 5.7c). The control sample exhibited rapid perovskite decomposition, underscoring the pronounced sensitivity of $CsPbI_2Br$ to moisture. The MgO-incorporated sample showed improved moisture resistance; larger grains and fewer boundaries limited moisture ingress and mitigated degradation pathways.

The sample stability was also evaluated under extreme conditions by PI test to assess their reliability more thoroughly. Protons generate atomic displacements in the PSC, effectively recreating a radiation spectrum similar to that encountered in LEO and offering a rigorous assessment of the device's resilience in extreme conditions.[262–265] Upon exposure of PSCs to PI, incoming protons lose energy through two primary mechanisms. Non-ionizing energy loss (NIEL) results from elastic collisions between incoming protons and lattice atoms, causing lattice damage.[262,266] In contrast, ionizing energy loss (IEL) arises from inelastic interactions, where protons scatter electrons, generating localized heating, that may promote partial lattice recovery within the perovskite absorber.[262,266–269] Previous investigations of proton radiation effects have predominantly focused on $CH_3NH_3PbI_3$[268,270–277] and mixed-cation/mixed-halide[262,278–280] perovskites, while Cs-based[263,281–283] inorganic PSCs remain comparatively underexplored. The work reported by Lang *et al.*[272] in 2016 revealed that under 68 MeV proton beams, perovskite films withstood cumulative doses, demonstrating approximately 1000 times the damage threshold of c-Si. Subsequent studies confirmed the resilience of PSCs to PI testing at 50 keV[276], 150 keV[284], 170 keV[280], 300 keV[279], and 1 MeV[262] with healing effect over time. Computational work by Nguyen *et al.*[263] further projected that $CsPbI_2Br$ can retain ~62% of its efficiency following 100 keV irradiation. In our experiments, the proton energies are correspondingly distributed from near 0 keV up to a maximum of ~170 keV at a total fluence of 2×10^{12} cm^{-2}. The selected proton energy and fluence are commonly used in irradiation studies of PSCs and closely match the

radiation conditions encountered in LEO, thereby enabling meaningful comparison with previously reported results. According to prior Stopping and Range of Ions in Matter simulations conducted under comparable conditions,[282] 170 keV protons are expected to penetrate and interact throughout the complete device stack. Boboev et al.[285] reported that nuclear stopping becomes more significant at lower proton energies, leading to increased vacancy formation near the surface. Conversely, at higher proton energies, ions penetrate deeper into the material while producing a lower density of displacement damage. As a result, the experimental observations presented in this work provide valuable insight into PI-induced effects in $CsPbI_2Br$ perovskites interfaced with different electron transport layers, namely ZnO and ZnO/MgO. SEM characterization was conducted before (Figure 5.7d,h) and after (Figure 5.7e,i) the irradiation tests. The results did not demonstrate notable changes in the perovskite morphology, indicating that the structural integrity of the perovskite film remains largely unaffected by the PI exposure.

Photoluminescence imaging via confocal microscopy enables direct visualization of non-radiative defect sites and charge-carrier recombination efficiency across perovskite films. Confocal maps were obtained for $CsPbI_2Br$ layers deposited on ZnO and ZnO/MgO ETLs before and after PI. The color scale represents relative emission intensity, with blue regions corresponding to low photoluminescence intensity and green to yellow/red regions indicating progressively stronger emission. The photoluminescence intensity is directly linked to the competition between radiative and non-radiative recombination pathways. Consequently, low-intensity (blue) regions are commonly associated with an increased density of trap states, which are known to facilitate non-radiative recombination pathways. These traps can capture charge carriers and dissipate their energy as phonons (heat) rather than photons. This process, known as Shockley–Read–Hall[286,287] recombination, quenches the photoluminescence intensity. For example, in the control sample (Figure 5.7f), the prevalence of deep-blue regions indicates a high density of traps and ineffective radiative recombination. Only a minor shift toward green is noted after the PI test (Figure 5.7g),

indicating some redistribution of traps but ongoing non-radiative losses. Meanwhile, the shift to green/yellow in the MgO-modified sample (Figure 5.7j) indicates successful defect passivation. By reducing the density of surface trap states, the MgO layer suppresses the non-radiative Shockley–Read–Hall pathway. After PI (Figure 5.7k), the emission intensifies further, transitioning to yellow-red colors. Consequently, charge carriers are more likely to undergo band-to-band radiative recombination, resulting in significantly higher photon emission. Notably, both ZnO and ZnO/MgO samples after PI exhibit enhanced fluorescence intensity compared with their pre-irradiation conditions. This enhancement could be explained to the defect annealing effect induced by irradiation, which helps passivate some shallow trap states and thereby promotes more efficient radiative performance. Comparable self-healing effects due to irradiation have also been documented in earlier research.[262,279,288,289]

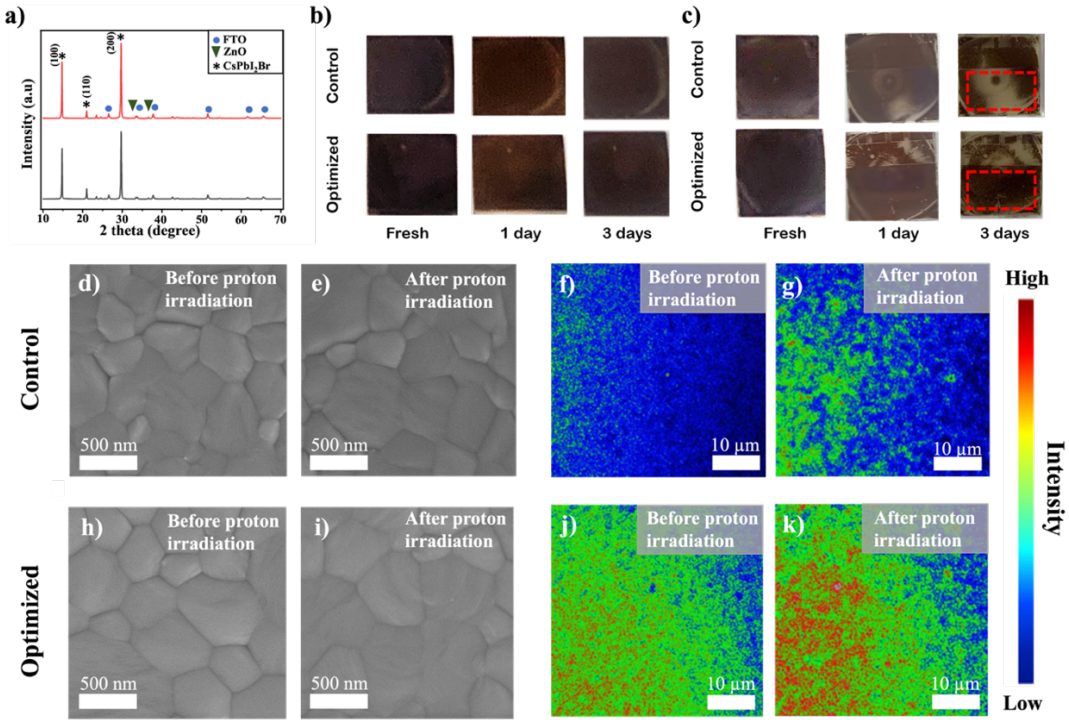

Figure 5.7 a) XRD spectra of ETL/perovskite samples; photographs of devices aging for 72 h in b) a glovebox and c) ambient air (30% RH); top-view SEM images before and after PI for the (d,e) control and (h,i) optimized samples; confocal photoluminescence maps before and after PI for the (f,g) control and (j,k) optimized samples. Reproduced from Ref[252] under CC BY 4.0

5.3.3 Device Performance and Stability Measurements

Transitioning from materials characterization to device implementation, the investigated ETLs were incorporated into full devices. For this, EOD, EQE, *J-V*, and shelf-lifetime analyses were applied.

First, the EODs featuring ZnO/$CsPbI_2Br$/PCBM/Ag and ZnO/MgO/$CsPbI_2Br$/PCBM/Ag configurations were constructed to examine the electron extraction and transport dynamics without hole-injection contributions. The space-charge-limited current (SCLC) technique is commonly used to evaluate charge carrier mobility and trap density in semiconductors.[290,291] Accordingly, electron-only or hole-only device structures are employed to isolate the transport of a single charge carrier. The trap-state density (n_{trap}) is calculated as follows: [290]

$$n_{trap} = \frac{2\varepsilon_r \varepsilon_0 V_{TFL}}{(qA^2)} \tag{5.2}$$

where $\varepsilon_r = 8.6$[292] represents the relative dielectric constant of perovskite, ε_0 is the permittivity of vacuum, VTFL is the trap-filled-limit voltage determined from SCLC measurements of the EOD, q signifies the elementary charge, and A denotes the thickness of the perovskite film (320 nm).

Meanwhile, the charge carrier mobility (μ_n) in the SCLC region was extracted using the Mott–Gurney law:[291]

$$\mu_n = \frac{8 J_D A^3}{9\varepsilon_r \varepsilon_0 V^2} \tag{5.3}$$

where J_D represents the current density, and V denotes the applied voltage.

SCLC analysis reveals that MgO interface engineering effectively lowers the trap concentration, reducing from 7.3 x 10^{15} cm^{-3} in the control cell to 6.4 x 10^{15} cm^{-3} in the modified cell—a ~12% reduction (Figure 5.8a). By suppressing these trap sites, carrier lifetimes are extended, and the probability of non-radiative recombination is diminished, directly contributing to enhanced device performance. The observed reduction in trap density correlates with the enhanced perovskite grain morphology seen in SEM (Figure 5.6c).

Electron mobility rises from 3.5×10^{-3} $cm^2 V^{-1}s^{-1}$ in the control cell to 4.3×10^{-3} $cm^2 V^{-1}s^{-1}$ in the MgO-modified device, representing an increase of ~23%. Enhanced electron mobility minimizes resistive losses and facilitates rapid electron transfer, increasing photocurrents and improving overall device efficiency.

The complete devices with ZnO/$CsPbI_2Br$/Spiro-OMeTAD/Au (Figure 5.9a) and ZnO/MgO/$CsPbI_2Br$/Spiro-OMeTAD/Au (Figure 5.9b) configurations were assembled, and their champion *J-V* curves are compared, in Figure 5.8b. The integration of the ultrathin MgO layer supports remarkable improvements in the key parameters. The notable increase in V_{oc} from 1.01 V in the control device to 1.20 V in the optimized device reflects the improved energy level alignment and suppressed interfacial recombination achieved by incorporating MgO (Figure 5.4). The systematically higher V_{oc} observed in the MgO-incorporated PSCs is consistent with prior studies demonstrating that an increased CBM offset at the ETL/perovskite interface improves junction quality and facilitates more efficient electron transport.[249] Furthermore, the J_{sc} parameter reaches 16.4 mA cm^{-2}, compared with 15.1 mA cm^{-2} for the control device. Improved J_{sc} aligns with the previously observed enhancements in electron mobility and lowered trap density. Prior studies using the SnO_2/MgO/$CH_3NH_3PbI_3$[247] and the mp-TiO_2/MgO/$CH_3NH_3PbI_3$[251] architectures have also demonstrated MgO's ability to minimize interfacial recombination and enhance performance.

The hysteresis behavior was calculated using the hysteresis index[293] (HI), as detailed in Figure 5.8c. In mixed halide inorganic PSCs, hysteresis often occurs because of the segregation of halides under light irradiation.[294] The samples demonstrated comparable HI values, with the control device exhibiting an HI of 0.097 and the MgO-modified device of 0.094. The slight decrease in hysteresis for the optimized device indicates that the design strategy has a beneficial, albeit small, impact on reducing hysteresis.

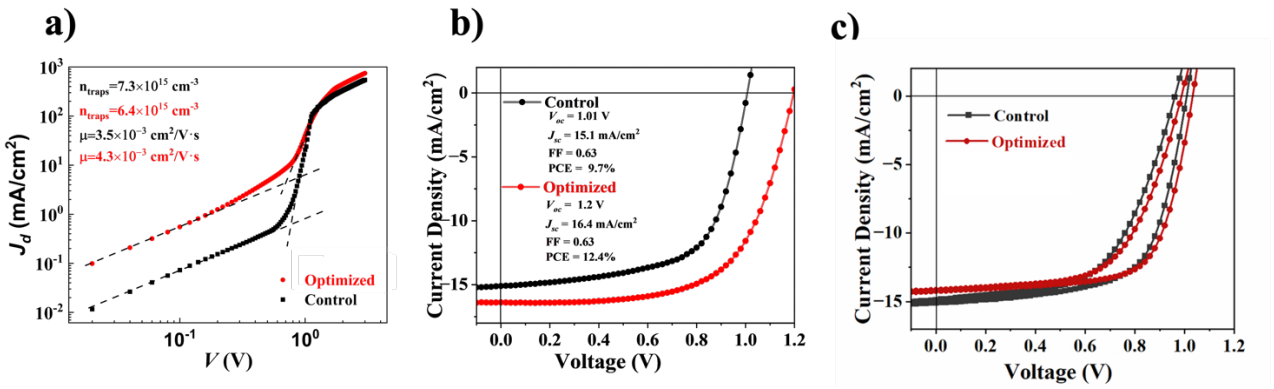

Figure 5.8 a) SCLC characteristics for EODs, showing trap-state density and electron mobility extraction, b) *J-V* curves of champion PSCs with and without MgO layers, c) *J-V* hysteresis comparison of the control and optimized devices. Adapted from Ref[252] under CC BY 4.0

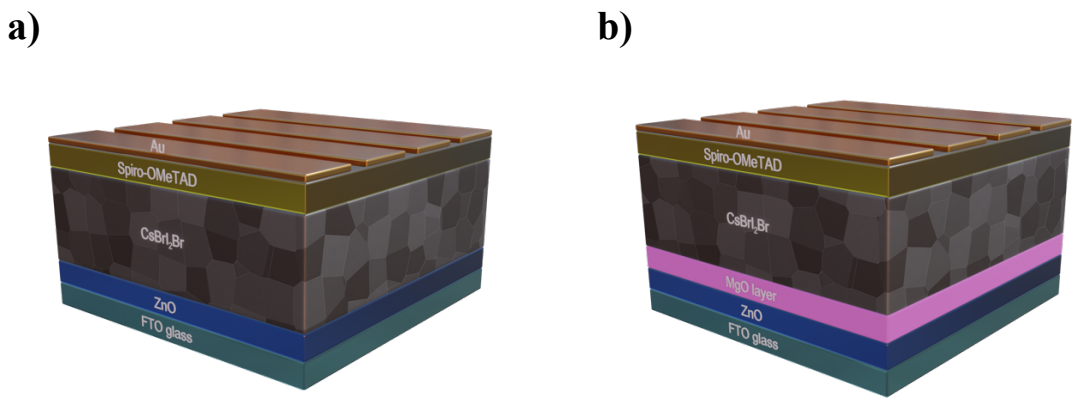

Figure 5.9 The fully assembled a) control and b) optimized devices

Although the champion MgO-modified device demonstrated the highest performance, statistical analysis across multiple devices is essential to validate reproducibility. Table 5.1 summarizes the average V_{oc}, J_{sc}, FF, and PCE values for both the control and MgO-modified device batches, including measurements performed immediately after fabrication and after 7 weeks of aging. In addition, Figure 5.10a shows a box-chart plot illustrating the statistical distribution of the initial device performance. Under fresh condition, the reported average values are based on measurements of 18 MgO-incorporated PSCs and 18 corresponding control devices. The data confirm that the performance improvement noted in the champion device reflects a general trend across the entire batch. After 7 weeks of storage in a glove box, the control devices showed a pronounced

degradation in performance. In particular, J_{sc} dropped by 54%, from 14.4 to 7.8 mA cm^{-2}. The decrease in PCE can be attributed to the instability at the ZnO/$CsPbI_2Br$ interface. Conversely, the optimized devices not only show improved initial performance, highlighted by a higher V_{oc} of 1.07 V, J_{sc} of 15.0 mA cm^{-2}, and PCE of 9.9%, but also maintain better stability; V_{oc} remains at 0.97 V, and J_{sc} decreases slightly to 13 mA cm^{-2}, demonstrating that the MgO interface layer effectively preserves charge transport pathways over time.

Table 5.1 Summary of the PV parameters for fresh, 7-week aged, and PI-tested PSCs. Reproduced from Ref[252] under CC BY 4.0

Parameter	V_{oc} (V)	J_{sc} (mA cm^{-2})	FF (%)	PCE (%)	(%)
Control					
Fresh	1.01±0.06	14.4±1.3	0.58±0.07	8.4±1.3	**-58**
Storage (7 week)	0.96±0.03	7.8±0.1	0.47±0.09	3.5±0.6	
Pre-PI (Initial)	1.02±0.05	14.8±0.7	0.53±0.07	8.1±1.8	**-43**
Post-PI (11 week)	1.01±0.12	8.8±3.6	0.57±0.16	4.65±0.3	
Optimized					
Fresh	1.07±0.07	15.0±0.9	0.61±0.05	9.9±1.3	**-40**
Storage (7 week)	0.97±0.09	13.0±0.3	0.47±0.02	5.9±0.4	
Pre-PI (Initial)	1.03±0.04	15.1±0.4	0.61±0.1	9.4±1.0	**+2**
Post-PI (11 week)	1.06±0.04	12.9±0.3	0.71±0.01	9.6±0.7	

The box chart plot (Figure 5.10a) includes the V_{oc}, J_{sc}, FF, and PCE. Note that the MgO-incorporated devices show significant improvements in both the mean and median values for all parameters compared to the control devices, indicating better overall performance and reproducibility.

The EQE technique indicates a superior optoelectrical response between 350 and 640 nm for the devices modified with MgO (Figure 5.10b). The integrated current densities derived from the EQE results were 12.5 mA cm^{-2} for control devices and 13.6 mA cm^{-2} for optimized devices. These J_{sc} values show a discrepancy of approximately ≈9.2%–12.6% compared with the J_{sc} from solar simulator testing. There is typically a strong correlation between the J_{sc} extracted from EQE measurements and that obtained from *J–V* characterization, with deviations commonly observed within a 10–20% range.[295,296] The variation in the J_{sc} parameter can be attributed to different light intensities and conditions of

illumination: 1 sun with an AM spectrum of 1.5 G for the IV tests and monochromatic light for the EQE assessments.[295]

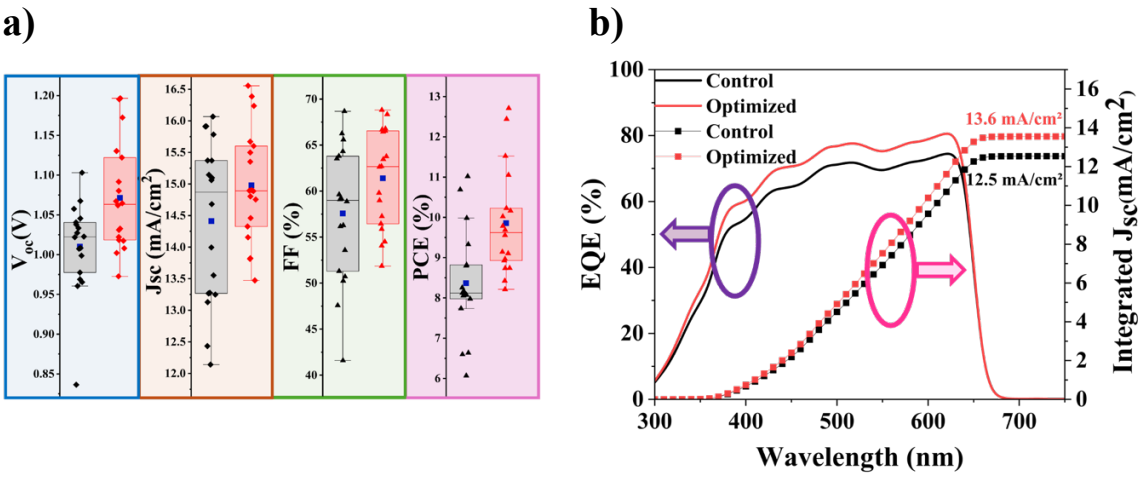

Figure 5.10 a) Box plots of the PV parameters for control and optimized devices, b) EQE spectra with the corresponding integrated J_{sc} values. Adapted from Ref[252] under CC BY 4.0

The enhanced optoelectrical properties determined based on the EQE measurements and corresponding J_{sc} values highlight the success of implementing the MgO thin film. However, evaluating the stability of the devices remains a crucial aspect.

Operational stability was investigated using *I–t* measurements performed over 10,000 s, during which the non-encapsulated devices were biased at their respective maximum power point voltages under ambient conditions (~30% RH) (Figure 5.11a). The MgO-modified PSC exhibits a minor initial rise in photocurrent, followed by stabilization. In contrast, the control device shows steady photocurrent decay over the first 4000 s. The MgO-incorporated device shows a stabilized current density of 16.3 mA/cm^2 at a bias of 0.94 V, corresponding to a stabilized PCE of 15.3%. The control device shows a stabilized current density of 11.5 mA/cm^2 at 0.9 V, yielding a stabilized PCE of 10.4%. The higher stabilized PCE of the MgO-incorporated device arises because *I–t* measurements reflect actual steady-state performance, whereas *J–V* scans are transient and may underestimate efficiency due to scan-rate effects and conditioning phenomena. The enhanced operational stability observed for the MgO-modified device is attributed to improved interfacial quality, characterized by a lower density of interfacial defects and enhanced electron extraction at the

ZnO/MgO/$CsPbI_2Br$ interface, consistent with the trends observed in the EOD device analysis.

To further quantify and compare the degradation behavior, the following decay rate (r) formula was applied to analyze the degradation rate:[297]

$$r = \frac{\Delta E}{t} \tag{5.4}$$

where ΔE signifies the change in efficiency, and t denotes the irradiation time.[297] Thus, the quantitative degradation analysis reveals that MgO-engineered PSCs maintain higher stability than the unmodified devices, highlighting MgO's effectiveness in strengthening the ETL/perovskite interface and enhancing long-term stability. The results are additionally validated by shelf-lifetime performance measurements (Figure 5.11b). The shelf-lifetime test showed that the MgO-modified devices retained 70% of their initial efficiency value, whereas the control cell degraded to 55% in 49 days.

Further stability testing was conducted using the PI test to simulate a harsh radiation environment. In our study, irradiated optimized devices surpassed pre-irradiation efficiencies after 11 weeks. The results demonstrate that PI increases the resilience of both device types. The control device decay rate remains comparable to its pre-irradiation value, but its sustained performance over 77 days demonstrates that proton exposure imparts a modest stability benefit. However, the optimized device following the PI test showed an impressive reduction in decay rate. Thus, the superior stability of the MgO-incorporated devices is evident in their ability to retain performance even under radiation exposure, presenting promising opportunities for future developments in this area, whereas the control device efficiency dropped to 47%.

The shelf-lifetime of devices subjected to PI is illustrated in Figure 5.11c. Both conditions exhibit an initial increase in PCE following PI. The control device shows a PCE enhancement during the first 168 h, while the MgO-incorporated device maintains this improvement for up to 1005 h.

Notably, Table 5.1 also reports statistical parameters averaged over three devices for

each condition measured before and after PI following 11 weeks of storage (Pre-PI and Post-PI). The same set of devices was evaluated in both states, enabling a direct assessment of PI-induced performance changes. The results present a significant enhancement in the FF of MgO-modified devices after PI, increasing from 61% to 71%. This rise in the FF is crucial because it influences the solar cell's efficiency by optimizing the power output at the various operating voltages. In addition, a modest increase in V_{oc} from 1.03 to 1.06 V further indicates improved energy-level alignment at the ETL/perovskite interface, contributing to suppressed recombination losses and overall efficiency gains. Remarkably, after 11 weeks of storage, the PCE slightly increased from 9.4% to 9.6%. While the J_{sc} only decreased from 15.1 to 12.9 mA cm^{-2}, it is important to consider this change in perspective; the control device showed a larger drop, decreasing from 14.8 to 8.8 mA cm^{-2}. These data substantiate the hypothesis that MgO incorporation enhances device robustness, effectively mitigating J_{sc} degradation and preserving overall PV performance. An evident pattern appears when analyzing the devices prior to and after the PI test; the addition of MgO significantly reduces the decay rate in both scenarios. Ultimately, the optimized devices subjected to PI testing showed the most pronounced impact.

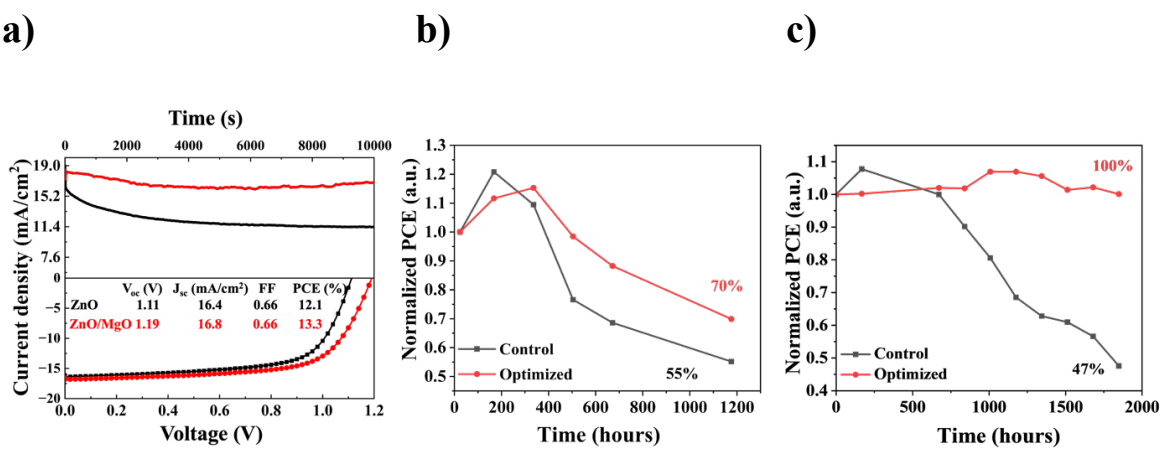

Figure 5.11 a) The *I–t* and *J–V* characteristics of the control and MgO-incorporated non-encapsulated devices were measured under ambient air conditions (≈30% RH). The I–t measurements were conducted at the maximum power point voltage determined from the corresponding J–V curves, shelf-lifetime plots of devices b) without PI, and c) after PI test. Adapted from Ref[252] under CC BY 4.0

Thus, the results indicate that the PI technique may induce a latent "self-healing"

mechanism. Similar post-irradiation recovery behavior has been widely reported in organic optoelectronic[289] devices as well as in hybrid and inorganic perovskite systems. Nevertheless, the fundamental mechanisms underlying this behavior remain incompletely understood and are actively under investigation. For example, some works linked the self-healing mechanism to defect redistribution driven by ion migration.[266,298,299] Owing to the soft and ionic nature of the metal–halide perovskite lattice, point defects such as vacancies and interstitials exhibit high mobility and can migrate and recombine. This process is facilitated by the moderate, localized energy deposited during irradiation. As a result, a partial re-annealing of irradiation-induced defects can occur through irradiation-assisted lattice reorganization.[266,298,299] It has been reported that PI can induce a doping effect in $CH_3NH_3PbI_3$ absorber. This occurs because irradiation generates shallow defects in the Pb–I structure that counteract deep traps associated with material degradation. Consequently, the compensation mechanism mitigates nonradiative recombination pathways, thereby boosting V_{oc} and FF.[268] To investigate the relationship between radiation-induced damage and self-healing processes, Kirmani et al.[262] conducted dual-irradiation studies on triple-cation perovskite materials. By tuning the ratio of IEL to NIEL using protons with energies of 0.06 and 1.0 MeV, they systematically evaluated the respective roles of ionization effects and displacement damage on the perovskite crystal lattice. The study revealed that low-energy PI (0.06 MeV), where NIEL is dominant, primarily causes damage through atomic displacements within the perovskite lattice. Conversely, high-energy protons (1.0 MeV), characterized by a substantially higher IEL/NIEL ratio, facilitated a partial healing process. This restorative effect is driven by IEL-induced phonon vibrations, which promote the relocation of displaced atoms back to their positions, thereby suppressing nonradiative recombination pathways. Nevertheless, when the ionizing contribution exceeds a critical threshold, a decline in PCE is observed, indicating that perovskite materials exhibit a finite radiation tolerance beyond which excessive IEL becomes detrimental.

The i-NURA accelerator generates a mixed ion beam composed of approximately

70% protons and 30% carbon ions, as reported by Shalenov et al.[300] In the device architecture (FTO/ETL/perovskite/HTL/Au), the 70 nm Au top electrode is the first layer exposed to irradiation. It therefore controls the fraction of each ion species that can penetrate the further layers. Because the accelerating voltage is pulsed, the ion energy is not monoenergetic but varies continuously from near 0 up to a peak value of ~170 keV. To evaluate ion transport under these conditions, Transport of Ions in Matter (TRIM, SRIM-2013) simulations were performed for both carbon and proton ions at discrete energies of 20, 70, 120, and 170 keV (Figure 5.12).

For the simulated 20 keV, carbon ions are almost entirely stopped within the Au electrode, whereas protons penetrate through the Au and HTL layers and reach the upper region of the perovskite absorber. At 70 keV, carbon ions penetrate further but still deposit most of their energy in the front part of the device stack, primarily within the Au/HTL and upper perovskite region. At 70–170 keV, the proton component clearly crosses the entire device. Meanwhile, the carbon component remains more spatially localized with simulated longitudinal projected ranges of 216 ± 120.7 nm at 120 keV and 276.5 ± 138.5 nm at 170 keV.

Considering the beam composition and the SRIM depth profiles, the proton component dominates the irradiation of the entire device. In contrast, the carbon component may contribute to additional localized damage near the surface and at interfacial regions. It should be noted that the I-NURA accelerator used in this study was employed as an experimental tool to evaluate the irradiation tolerance of PSCs under pulsed high-energy ion beam exposure. Importantly, both the control and MgO-incorporated devices were irradiated in the same batch under identical experimental conditions. Therefore, the differences observed in device performance and post-irradiation stability primarily reflect the influence of the device architecture, specifically the presence or absence of the MgO at the ETL/perovskite interface.

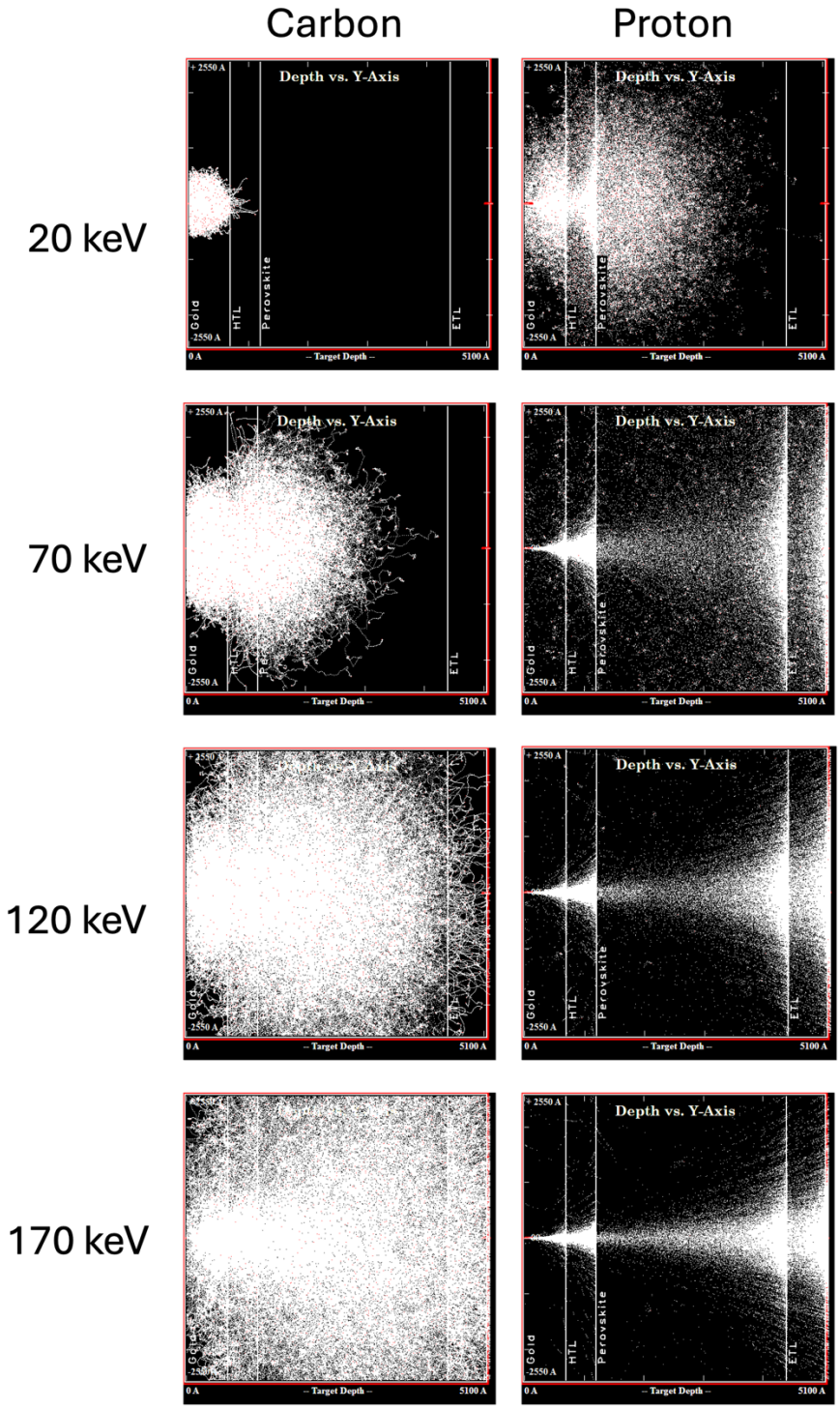

Figure 5.12 SRIM-simulated depth profiles of protons and carbon ions in the PSC structure at different energies.

Based on SRIM simulations, protons are expected to penetrate most of the device stack, thereby playing a dominant role in irradiating the absorber and underlying layers. However, the potential influence of the carbon component cannot be excluded, as heavier ions may induce more localized energy deposition and defect formation near the surface or at interfacial regions. Because irradiation was performed with a mixed ion beam, the

contributions of protons and carbon ions cannot be unambiguously distinguished in the present experiments. Within these limitations, the results presented here allow a reliable comparison of the irradiation stability of PSCs with and without the MgO. The improved stability observed for the optimized devices suggests that incorporating MgO enhances the robustness of the ETL/perovskite interface under PI and during subsequent shelf-life aging. Further investigations using ion sources with controlled single-species beams would be required to precisely determine the individual roles of protons and carbon ions in the observed device response.

Also, the possible contribution of beam-induced heating during proton irradiation was carefully considered. Using an energy density of ~0.0255 J cm^{-2}, and an effective energy-deposition depth of ~1 μm, corresponding to the total thickness of the device stack, the resulting volumetric energy density is estimated to be ~250 J cm^{-3}. Assuming a representative volumetric heat capacity of 2−3 J $cm^{-3}K^{-1}$, the transient local temperature rise during a single pulse is estimated to be ~85−130 °C. According to published data on proton stopping ranges under comparable irradiation conditions, the effective energy-deposition depth is ~1 μm.[301]

However, the ion beam pulse duration is approximately 150 ns, meaning that the associated temperature rise is very short-lived and does not allow significant heat accumulation within the device. In addition, this transient temperature increase is comparable to, or lower than, the temperatures typically used during device fabrication and post-deposition annealing. Therefore, it is less likely to be the dominant factor responsible for the observed changes in device performance and stability. Nevertheless, the potential influence of temperature could be further investigated in future studies as a separate effect.

In this study, we attribute the observed behavior to an irradiation-induced defect reorganization within the perovskite layer. The PI can promote the migration and recombination defects through electronic excitation and localized collision cascades, resulting in a reduction of sub-bandgap trap states.[252,266] Evidence for this behavior is

provided by the confocal laser-scanning microscopy images in Figure 5.7(g,k), which reveal a noticeable enhancement in photoluminescence intensity after PI in both device configurations. This increase in emission intensity indicates a decrease in the density of sub-bandgap trap states. However, the two device architectures follow significantly different shelf-lifetime evolution paths after PI. Because the ETL is the only structural parameter varied between the control and optimized devices, the contrasting post-irradiation stability behavior can be reasonably attributed to differences in the interfacial environment created by the ZnO/MgO structure. The incorporation of MgO onto ZnO film promotes the formation of a more robust $CsPbI_2Br$ with enlarged grain size, as confirmed by SEM analysis (Figure 5.6c), and the enhanced film integrity observed during prolonged air exposure (Figure 5.7c). This optimized interfacial configuration likely improves the perovskite's tolerance to PI. While, the irradiated control device showed a slight increase in PCE in the initial 200 hours, a phenomenon likely attributable to partial defect annealing. However, this transient improvement was quickly superseded by a sharp decline in performance, indicating the rapid emergence of irradiation-induced defects or structural instability. The inferior interfacial stability and higher defect density of perovskite films deposited directly on the ZnO layer compromise the perovskite's resistance to PI, resulting in accelerated performance degradation during subsequent shelf aging.

While the literature generally identifies organic HTLs, such as PTAA and Spiro-OMeTAD, as the most vulnerable components under PI compared to relatively robust ETLs (e.g., TiO_2, SnO_2, and In_2O_3),[302,303] the stability of ZnO-based ETLs can also be affected by irradiation. Proton exposure can modify the conductivity of ZnO in thin-film transistor devices.[304] Thus, the potential effects of PI on the ETL in this work cannot be discounted. Our results suggest that MgO incorporation plays a key role in stabilizing the ETL/perovskite interface by limiting interfacial defect formation and preserving efficient carrier extraction, enabling stable retention of device performance after irradiation.

A consistent and meaningful benchmark of stability performance is established by

comparing the present results exclusively with literature reports that employ the same $CsPbI_2Br$ absorber and evaluate device aging under identical inert N_2 glovebox storage conditions.

As summarized in Table 5.2, the FTO/ZnO/MgO/$CsPbI_2Br$/Spiro-OMeTAD/Au devices retained approximately 70 % of their initial PCE after 1176 h of storage. When compared at equivalent time scales, this stability is competitive with or superior to reported $CsPbI_2Br$-based devices. For example, the ITO/SnO_2/$CsPbI_2Br$/BTEC-2F/Spiro-OMeTAD/Ag/MoO_3 architecture exhibits a 19 % PCE loss after 500 h, while the present devices maintain 100 % of their initial efficiency over the same period (Figure 5.11b). Similarly, devices employing P3HT protection layers retain approximately 80% of PCE after 100 h, whereas the devices reported here maintain full efficiency over an equivalent storage time. The most significant outcome of this study is the pronounced enhancement in long-term stability observed for the irradiated MgO-incorporated devices, which retain 100 % of their initial PCE after 1848 h of storage. Within the subset of literature reports, this performance represents a state-of-the-art level of storage stability, exceeding previously reported retention values over comparable time scales.

Notably, this enhanced stability is achieved without introducing complex device architectures or additional protective layers, relying instead on interfacial engineering at the ETL/perovskite interface and a PI-induced self-healing effect. This combination provides an effective, scalable pathway to suppress degradation mechanisms while maintaining a relatively simple device structure.

Table 5.2 Stability Performance Comparison of $CsPbI_2Br$-based PSCs

Year	Device Architecture	Storage conditions	Time Duration (h)	PCE Retention	Ref.
2019	ITO/SnO_2/$CsPbI_2Br$/Spiro-OMeTAD/MoO_3/Ag	N_2 glovebox	1440	89%	[305]
2020	ITO/SnO_2/CsBr/$CsPbI_2Br$/Spiro-OMeTAD/Ag	N_2 glovebox	960	87%	[306]
2021	ITO/SnO2/$CsPbI_2Br$/BTEC-2F/Spiro-OMeTAD/Ag/MoO_3	N_2 glovebox	500	81%	[307]

2021	ITO/ZnO/SnO_2/$CsPbI_2Br$/(PEABr+CsBr)/Spiro-OMeTAD/Ag	N_2 glovebox	1000	92%	[240]
2021	ITO/SnO_2/ZnO/($CsPbI_2Br$+$BMIMPF_6$)/D-PTAA/MoO_3/Ag	N_2 glovebox	1200	98.9%	[308]
2024	ITO/NiO_x/$CsPbI_2Br$/CFPA/PCBM/BCP/Ag	N_2 glovebox	1992	96%	[309]
2025	ITO/SnO_2/$CsPbI_2Br$/P3HT protection/P3HT/Au	N_2 glovebox	100	80%	[217]
2025	ITO/SnO_2/$CsPbI_2Br$/1-B-3-MIMCl/Carbon	N_2 glovebox	1200	84.7%	[310]
This work	FTO/ZnO/MgO/$CsPbI_2Br$/Spiro-OMeTAD/Au	N_2 glovebox	1176	70%	[252]
	Irradiated FTO/ZnO/MgO/$CsPbI_2Br$/Spiro-OMeTAD/Au	N_2 glovebox	1848	100%	[252]

5.4 Summary

Interfacial engineering was applied in $CsPbI_2Br$-based PSCs by introducing a MgO thin film between the ETL and the absorber layer. The individual impacts of MgO incorporation on the ETL, perovskite absorber, and fully assembled device architecture were systematically investigated. The incorporation of the MgO layer significantly reduces interfacial recombination, as demonstrated by a decrease in trap density from 7.3 to 6.4 × 10^{15} cm^{-3}. Additionally, it improves charge transport by raising electron mobility from 3.5 to 4.3 cm^2 $V^{-1}·s^{-1}$. Furthermore, the introduction of MgO greatly enhanced long-term stability, a crucial issue in the advancement of PSCs. Enhanced durability was demonstrated under three conditions: storage in ambient air (30 % RH), in a glovebox, and after PI testing. After 7 weeks of storage, the MgO-incorporated devices exhibited high stability, with the J_{sc} decreasing only modestly from 15.0 to 13.0 mA^{-2} compared with the significant drop from 14.4 to 7.8 mA cm^{-2} for the control device.

Furthermore, modified and unmodified devices underwent PI testing to evaluate their PV performance and stability under simulated space-radiation conditions, thereby extending the investigation of device resilience to encompass harsh environmental stresses. The shelf-life assessment following PI further validated the resilience of the MgO-modified devices: over 11 weeks, the optimized devices showed a slight improvement in their initial PCE, V_{oc} and FF. These improvements suggest a suppression of non-radiative recombination processes

and facilitated charge transport in the device architecture. The enhancement in V_{oc} from 1.03 to 1.06 V results from the energy offset at the ETL/perovskite interface caused by the MgO layer, which promotes more effective energy alignment. This outstanding post-irradiation stability, coupled with enhanced PV performance, underscores the potential of MgO-incorporated inorganic PSCs for application in high-radiation environments, including space applications.

CHAPTER 6. CONCLUSION

6.1 Conclusion

Driven by the global imperative for sustainable energy solutions and inspired by the remarkable progress of PSCs, this work addressed one of the most fundamental challenges in the PV field: the performance degradation caused by interfacial defects and instability.

A high-quality, defect-free interface between the ETL and the absorber layer is essential for efficient extracting and collecting charge carriers. By reducing interfacial trap states, non-radiative recombination is strongly suppressed, thereby preserving carrier lifetimes and maximizing the V_{oc}. At the same time, careful alignment of the energy levels between the conduction band of the absorber and ETM eliminates energy barriers to electron transfer, reducing resistive losses and ensuring fast, unimpeded carrier extraction.

Recognizing the crucial role of the interface between the ETL and the perovskite absorber in determining device efficiency and stability, this study investigated two different interfacial engineering strategies to optimize charge transport and suppress degradation pathways.

The first strategy involved the growth of SnO_2 NA on ETLs. The penetration of perovskite grains within the nanostructured ETL significantly enlarges the interfacial region, facilitating the rapid transfer of photogenerated electrons into the ETL prior to carrier recombination. The effects of various growth parameters, such as the growth pressure, substrate orientation, ratio of DI water to ethanol, seed layer, acetic acid concentration, and growth duration, on the morphology of solvothermally-grown SnO_2 nanostructures were thoroughly studied. SEM analysis validated the successful creation of vertically aligned and evenly distributed SnO_2 NAs. This work demonstrated that customized nanostructuring SnO_2 is effective in the development of high-quality ETLs. In addition, the results offer a foundation for upcoming research focused on accurately regulating the density, length, diameter, and structural alignment of SnO_2 nanorods, which play a crucial role in the interfacial contact, charge transport dynamics, and performance of PSCs.

The second strategy involved the incorporation of a thin MgO interlayer between the ETL and the perovskite absorber. This modification not only enhanced the crystallinity of the perovskite film but also reduced interfacial trap densities, thereby improving charge collection efficiency. The presence of the MgO layer created a passivated interface, which effectively suppressed non-radiative recombination. As a result, the MgO-incorporated devices exhibited significantly enhanced operational stability. Under ambient conditions, glovebox aging, and PI exposure, these devices retained a much higher portion of their initial efficiency than their unmodified counterparts, demonstrating the critical role of MgO in promoting device durability and reliability for real-world and high-stress applications.

To fully understand and evaluate the interfacial strategies, advanced characterization techniques are essential. As part of the extensive characterization approach employed in this study, specialized cross-sectional AFM holders were developed to facilitate advanced morphological and electronic evaluations of FTO-coated and flexible substrates. The designs were optimized to minimize mechanical vibrations and maintain the integrity of both the sample and the AFM tip throughout the scanning process. The advanced cross-sectional AFM method has significant potential to further elucidate how interfacial engineering approaches influence device performance at the nanoscale. Cross-sectional AFM measurements offer valuable information about the unique characteristics of each layer, including assessments of the adhesion, mechanical strength, and defect distribution.

In conclusion, by thoroughly investigating the fundamentals of PSCs and interfacial modification strategies, this research provides important insights into how interface engineering can be effectively employed to overcome the key challenges faced by PSCs.

6.2 Future Work

One of the key outcomes of the present work is the demonstration that SnO_2 nanostructures can be grown in a controlled manner to increase the contact area between the ETL and the perovskite layer. This not only facilitates better charge extraction but also creates

opportunities to design interfaces with enhanced electronic properties. By adjusting the growth parameters explored in this work, future investigations can intentionally aim for specific morphologies, such as closely packed arrays for optimal surface coverage or branched/hollow structures for improved light scattering, which is particularly beneficial for thinner absorber layers in lightweight, portable, or space-constrained applications. Additional surface treatment methods may be developed to passivate remaining trap sites and enhance wettability for perovskite deposition. Moreover, incorporating aliovalent cations (Sb, F) into SnO_2 or adding secondary oxides (TiO_2, ZnO) may help to finely adjust the band alignment and increase carrier mobility, thus optimizing the PV performance.

Integrating MgO passivation with PI treatment across various device designs: planar, mesoporous, and graded-bandgap tandem stacks, may uncover synergistic improvements in stability, as irradiation may trigger dormant self-healing mechanisms in each architecture. The enhanced stability resulting from the combination of these two approaches may be critical for accelerating the commercialization of perovskite technologies. Next, to confirm their viability for space applications, devices should undergo exposure to higher-energy proton beams (e.g., 1 MeV), along with additional irradiation procedures involving heavy ions, gamma rays, and UV-C, in combination with thermal cycling and vacuum-bake tests, to replicate the full range of extraterrestrial challenges. Extensive testing is expected to provide essential information regarding the mechanical and electronic reliability of these systems in space environments where high durability is required. Furthermore, achieving precise sub-nanometer control over the thickness of MgO through atomic layer or molecular-layer deposition may facilitate the fine-tuning of interfacial dipoles and barrier heights; incorporating secondary oxides (Al_2O_3, ZnO) in graded or cascading heterostructures may enhance electron extraction while preventing hole transport.

Ultimately, interface engineering strategies must be refined to enhance PV performance and stability. These improvements are necessary to support real-world applications and promote a sustainable future.

REFERENCE LIST

[1]"Global overview – Renewables 2024 – Analysis - IEA," Https://Www.Iea.Org/Reports/Renewables-2024/Global-Overview, (2024).

[2]"Kazakhstan's Renewable Energy Sector Gains Momentum with 146 Facilities in Operation - The Astana Times," (n.d.).

[3] J. Kennewell, and A. McDonald, "SWS - The Sun and Solar Activity - The Solar Constant," (2025).

[4] M. Dada, and P. Popoola, "Recent advances in solar photovoltaic materials and systems for energy storage applications: a review," Beni. Suef. Univ. J. Basic Appl. Sci. **12**(1), (2023).

[5] I. Slav, "Solar Is Cheapest Energy Source Says IEA," (2023).

[6] M. Yaghoobi, M. Alaei, M. Shirazi, N. Rezaei, and S. de Gironcoli, "Discovery of novel silicon allotropes with optimized band gaps to enhance solar cell efficiency through evolutionary algorithms and machine learning," Comput. Mater. Sci. **246**, 113392 (2025).

[7] S. Rühle, "Tabulated values of the Shockley–Queisser limit for single junction solar cells," Solar Energy **130**, 139–147 (2016).

[8]"Best Research-Cell Efficiency Chart | Photovoltaic Research | NREL," (2025).

[9] P. Roy, A. Ghosh, F. Barclay, A. Khare, and E. Cuce, "Perovskite Solar Cells: A Review of the Recent Advances," Coatings **12**(8), (2022).

[10] A.P. Saffar, and B.D. Barani, "Thermal effects investigation on electrical properties of silicon solar cells treated by laser irradiation," International Journal of Renewable Energy Development **3**(3), 184–187 (2014).

[11] F. Elhady, M. Fedawy, T.M. Abdolkader, and T.M. Abdolkader', *A Review of Thin Film Solar Cells* (2021).

[12] M. Stuckelberger, Y. Riesen, M. Despeisse, J.W. Schüttauf, F.J. Haug, and C. Ballif, "Light-induced Vocincrease and decrease in high-efficiency amorphous silicon solar cells," J. Appl. Phys. **116**(9), (2014).

[13] R.R. King, D.C. Law, K.M. Edmondson, C.M. Fetzer, G.S. Kinsey, H. Yoon, R.A. Sherif, and N.H. Karam, "40% efficient metamorphic GaInPGaInAsGe multijunction solar cells," Appl. Phys. Lett. **90**(18), (2007).

[14] M.M. Byranvand, C. Otero-Martínez, J. Ye, W. Zuo, L. Manna, M. Saliba, R.L.Z. Hoye, and L. Polavarapu, "Recent Progress in Mixed A-Site Cation Halide Perovskite Thin-Films and Nanocrystals for Solar Cells and Light-Emitting Diodes," Adv. Opt. Mater. **10**(14), (2022).

[15] C. Yang, W. Hu, J. Liu, C. Han, Q. Gao, A. Mei, Y. Zhou, F. Guo, and H. Han, "Achievements, challenges, and future prospects for industrialization of perovskite solar cells," Light Sci. Appl. **13**(1), (2024).

[16] N. Dengo, D.F. Macias-Pinilla, S. Virga, S. Bini, F. Giannici, and F. Bertolotti, “Bonding Mechanisms Underpinning Structural and Electronic Properties of Halide Perovskites,” Coord. Chem. Rev. **552**, 217470 (2026).

[17] X. Liang, J. Klarbring, W.J. Baldwin, Z. Li, G. Csányi, and A. Walsh, “Structural Dynamics Descriptors for Metal Halide Perovskites,” Journal of Physical Chemistry C **127**(38), 19141–19151 (2023).

[18] M.H. Miah, M.U. Khandaker, M.B. Rahman, M. Nur-E-Alam, and M.A. Islam, “Band gap tuning of perovskite solar cells for enhancing the efficiency and stability: issues and prospects,” RSC Adv. **14**(23), 15876–15906 (2024).

[19] L. Zhang, Z. Zhuang, Q. Fang, and X. Wang, “Study on the Automatic Identification of ABX3 Perovskite Crystal Structure Based on the Bond-Valence Vector Sum,” Materials 2023, Vol. 16, Page 334 **16**(1), 334 (2022).

[20] J. Xue, R. Wang, X. Chen, C. Yao, X. Jin, K.-L. Wang, W. Huang, T. Huang, Y. Zhao, Y. Zhai, D. Meng, S. Tan, R. Liu, Z.-K. Wang, C. Zhu, K. Zhu, M.C. Beard, Y. Yan, and Y. Yang, *Reconfiguring the Band-Edge States of Photovoltaic Perovskites by Conjugated Organic Cations* (n.d.).

[21] F. Pakravesh, and M. Izadyar, *Theoretical Insights into the Electronic and Optical Properties of Lithium-Based Perovskite for Solar Cell Applications* (n.d.).

[22] T. Duan, I. Mora-Seró, and Y. Zhou, “Introduction to Perovskite,” in *Halide Perovskite Semiconductors: Structures, Characterization, Properties, and Phenomena,* edited by Y. Zhou and I. Mora-Seró, First Edition, (WILEY-VCH GmbH, 2024), p. 2.

[23] Y. Yu, J. Xia, and Y. Liang, “Basic understanding of perovskite solar cells and passivation mechanism,” AIP Adv. **12**(5), (2022).

[24] W. Travis, E.N.K. Glover, H. Bronstein, D.O. Scanlon, and R.G. Palgrave, “On the application of the tolerance factor to inorganic and hybrid halide perovskites: A revised system,” Chem. Sci. **7**(7), 4548–4556 (2016).

[25] G.T. Chavan, Y. Kim, M.Q. Khokhar, S.Q. Hussain, E.C. Cho, J. Yi, Z. Ahmad, P. Rosaiah, and C.W. Jeon, “A Brief Review of Transparent Conducting Oxides (TCO): The Influence of Different Deposition Techniques on the Efficiency of Solar Cells,” Nanomaterials **13**(7), (2023).

[26] D. Burnat, P. Sezemsky, K. Lechowicz, M. Koba, M. Janczuk-Richter, M. Janik, V. Stranak, J. Niedziółka-Jönsson, R. Bogdanowicz, and M. Śmietana, “Functional fluorine-doped tin oxide coating for opto-electrochemical label-free biosensors,” Sens. Actuators B Chem. **367**, (2022).

[27] R.A. Afre, and D. Pugliese, “Perovskite Solar Cells: A Review of the Latest Advances in Materials, Fabrication Techniques, and Stability Enhancement Strategies,” Micromachines

(Basel). **15**(2), (2024).

[28] *The ABX 3 Perovskite Structure* (2016).

[29] R. Sharif, A. Khalid, S.W. Ahmad, A. Rehman, H.G. Qutab, H.H. Akhtar, K. Mahmood, S. Afzal, and F. Saleem, "A comprehensive review of the current progresses and material advances in perovskite solar cells," Nanoscale Adv. **5**(15), 3803–3833 (2023).

[30] P. Roy, N. Kumar Sinha, S. Tiwari, and A. Khare, "A review on perovskite solar cells: Evolution of architecture, fabrication techniques, commercialization issues and status," Elsevier **198**, 665–688 (2020).

[31] D.B. Mitzi, "Synthesis, Structure, and Properties of Organic-Inorganic Perovskites and Related Materials," Progress in Inorganic Chemistry **48**, 1–121 (2007).

[32] A. Kojima, K. Teshima, Y. Shirai, and T. Miyasaka, "Organometal halide perovskites as visible-light sensitizers for photovoltaic cells," J. Am. Chem. Soc. **131**(17), 6050–6051 (2009).

[33] R. Sharma, A. Sharma, S. Agarwal, and M. Dhaka, "Stability and efficiency issues, solutions and advancements in perovskite solar cells: A review," (2022).

[34] H.S. Kim, C.R. Lee, J.H. Im, K.B. Lee, T. Moehl, A. Marchioro, S.J. Moon, R. Humphry-Baker, J.H. Yum, J.E. Moser, M. Grätzel, and N.G. Park, "Lead iodide perovskite sensitized all-solid-state submicron thin film mesoscopic solar cell with efficiency exceeding 9%," Sci. Rep. **2**, (2012).

[35] T. Webb, S.J. Sweeney, and W. Zhang, "Device Architecture Engineering: Progress toward Next Generation Perovskite Solar Cells," Adv. Funct. Mater. **31**(35), (2021).

[36] M.M. Lee, J. Teuscher, T. Miyasaka, T.N. Murakami, and H.J. Snaith, "Efficient hybrid solar cells based on meso-superstructured organometal halide perovskites," Science (1979). **338**(6107), 643–647 (2012).

[37] J.M. Ball, M.M. Lee, A. Hey, and H.J. Snaith, "Low-temperature processed meso-superstructured to thin-film perovskite solar cells," Energy Environ. Sci. **6**(6), 1739–1743 (2013).

[38] J.Y. Jeng, Y.F. Chiang, M.H. Lee, S.R. Peng, T.F. Guo, P. Chen, and T.C. Wen, "CH3NH3PbI3 Perovskite/Fullerene Planar-Heterojunction Hybrid Solar Cells," Advanced Materials **25**(27), 3727–3732 (2013).

[39] J. Burschka, N. Pellet, S.J. Moon, R. Humphry-Baker, P. Gao, M.K. Nazeeruddin, and M. Grätzel, "Sequential deposition as a route to high-performance perovskite-sensitized solar cells," Nature 2013 499:7458 **499**(7458), 316–319 (2013).

[40] J.H. Im, I.H. Jang, N. Pellet, M. Grätzel, and N.G. Park, "Growth of CH3NH3PbI3 cuboids with controlled size for high-efficiency perovskite solar cells," Nature Nanotechnology 2014 9:11 **9**(11), 927–932 (2014).

[41] J. Dong, Y. Zhao, J. Shi, H. Wei, J. Xiao, X. Xu, J. Luo, J. Xu, D. Li, Y. Luo, and Q. Meng, "Impressive enhancement in the cell performance of ZnO nanorod-based perovskite solar cells with Al-doped ZnO interfacial modification," Chemical Communications **50**(87), 13381–13384 (2014).

[42] C. Xu, P. Shin, L. Cao, and D. Gao, "Preferential growth of long ZnO nanowire array and its application in dye-sensitized solar cells," Journal of Physical Chemistry C **114**(1), 125–129 (2010).

[43] P. Löper, S.J. Moon, S. Martín De Nicolas, B. Niesen, M. Ledinsky, S. Nicolay, J. Bailat, J.H. Yum, S. De Wolf, and C. Ballif, "Organic–inorganic halide perovskite/crystalline silicon four-terminal tandem solar cells," Physical Chemistry Chemical Physics **17**(3), 1619–1629 (2014).

[44] K. Wang, C. Liu, P. Du, J. Zheng, and X. Gong, "Bulk heterojunction perovskite hybrid solar cells with large fill factor," Energy Environ. Sci. **8**(4), 1245–1255 (2015).

[45] F. Giordano, A. Abate, J.P. Correa Baena, M. Saliba, T. Matsui, S.H. Im, S.M. Zakeeruddin, M.K. Nazeeruddin, A. Hagfeldt, and M. Graetzel, "Enhanced electronic properties in mesoporous TiO2 via lithium doping for high-efficiency perovskite solar cells," Nat. Commun. **7**, (2016).

[46] W.S. Yang, J.H. Noh, N.J. Jeon, Y.C. Kim, S. Ryu, J. Seo, and S. Il Seok, "High-performance photovoltaic perovskite layers fabricated through intramolecular exchange," Science (1979). **348**(6240), 1234–1237 (2015).

[47] J.H. Heo, and S.H. Im, "CH3NH3PbBr3–CH3NH3PbI3Perovskite–Perovskite Tandem Solar Cells with Exceeding 2.2 V Open Circuit Voltage," Advanced Materials **28**(25), 5121–5125 (2016).

[48] X. Li, D. Bi, C. Yi, J.D. Décoppet, J. Luo, S.M. Zakeeruddin, A. Hagfeldt, and M. Grätzel, "A vacuum flash-assisted solution process for high-efficiency large-area perovskite solar cells," Science (1979). **353**(6294), 58–62 (2016).

[49] D. Bi, C. Yi, J. Luo, J.D. Décoppet, F. Zhang, S.M. Zakeeruddin, X. Li, A. Hagfeldt, and M. Grätzel, "Polymer-templated nucleation and crystal growth of perovskite films for solar cells with efficiency greater than 21%," Nature Energy 2016 1:10 **1**(10), 1–5 (2016).

[50] W.S. Yang, B.W. Park, E.H. Jung, N.J. Jeon, Y.C. Kim, D.U. Lee, S.S. Shin, J. Seo, E.K. Kim, J.H. Noh, and S. Il Seok, "Iodide management in formamidinium-lead-halide-based perovskite layers for efficient solar cells," Science (1979). **356**(6345), 1376–1379 (2017).

[51] A. Rajagopal, P.W. Liang, C.C. Chueh, Z. Yang, and A.K.Y. Jen, "Defect Passivation via a Graded Fullerene Heterojunction in Low-Bandgap Pb-Sn Binary Perovskite Photovoltaics," ACS Energy Lett. **2**(11), 2531–2539 (2017).

[52] D. Yang, R. Yang, K. Wang, C. Wu, X. Zhu, J. Feng, X. Ren, G. Fang, S. Priya, and S.

(Frank) Liu, “High efficiency planar-type perovskite solar cells with negligible hysteresis using EDTA-complexed SnO2,” Nature Communications 2018 9:1 **9**(1), 1–11 (2018).

[53] H.S. Kim, A. Hagfeldt, and N.G. Park, “Morphological and compositional progress in halide perovskite solar cells,” Chemical Communications **55**(9), 1192–1200 (2019).

[54] Q. Jiang, Y. Zhao, X. Zhang, X. Yang, Y. Chen, Z. Chu, Q. Ye, X. Li, Z. Yin, and J. You, “Surface passivation of perovskite film for efficient solar cells,” Nature Photonics 2019 13:7 **13**(7), 460–466 (2019).

[55] J. Jeong, M. Kim, J. Seo, H. Lu, P. Ahlawat, A. Mishra, Y. Yang, M.A. Hope, F.T. Eickemeyer, M. Kim, Y.J. Yoon, I.W. Choi, B.P. Darwich, S.J. Choi, Y. Jo, J.H. Lee, B. Walker, S.M. Zakeeruddin, L. Emsley, U. Rothlisberger, A. Hagfeldt, D.S. Kim, M. Grätzel, and J.Y. Kim, “Pseudo-halide anion engineering for α-FAPbI3 perovskite solar cells,” Nature **592**(7854), 381–385 (2021).

[56] J. Feng, Y. Jiao, H. Wang, X. Zhu, Y. Sun, M. Du, Y. Cao, D. Yang, and S.F. Liu, “High-throughput large-area vacuum deposition for high-performance formamidine-based perovskite solar cells,” Energy Environ. Sci. **14**(5), 3035–3043 (2021).

[57] G. Schileo, and G. Grancini, “Lead or no lead? Availability, toxicity, sustainability and environmental impact of lead-free perovskite solar cells,” J. Mater. Chem. C Mater. **9**(1), 67–76 (2021).

[58] A.T. Marshall, S. Betts, E.C. Kan, R. McConnell, B.P. Lanphear, and E.R. Sowell, “Association of lead-exposure risk and family income with childhood brain outcomes,” Nature Medicine 2020 26:1 **26**(1), 91–97 (2020).

[59] U.U. Rehman, R.S. Almufarij, A.R. Abd-Elwahed, K.U. Sahar, E. Hussain, A. Ashfaq, K. Mahmood, and C.M. Wang, “Improving efficiency of germanium-based perovskite solar cells with graphene interface layer: A strategy to minimize charge recombination,” Journal of Physics and Chemistry of Solids **198**, 112487 (2025).

[60] B. Bin Yu, Z. Chen, Y. Zhu, Y. Wang, B. Han, G. Chen, X. Zhang, Z. Du, and Z. He, “Heterogeneous 2D/3D Tin-Halides Perovskite Solar Cells with Certified Conversion Efficiency Breaking 14%,” Advanced Materials **33**(36), 2102055 (2021).

[61] N.K. Tailor, R.K. Rohj, K. Dey, S.D. Stranks, D.D. Sarma, and S. Satapathi, “Unraveling low-temperature structural and dielectric characteristics in lead-free bismuth halide perovskites,” J. Mater. Chem. C Mater. **13**(2), 918–927 (2025).

[62] V. Stancu, A.G. Tomulescu, L.N. Leonat, L.M. Balescu, A.C. Galca, V. Toma, C. Besleaga, S. Derbali, and I. Pintilie, “Partial Replacement of Dimethylformamide with Less Toxic Solvents in the Fabrication Process of Mixed-Halide Perovskite Films,” Coatings 2023, Vol. 13, Page 378 **13**(2), 378 (2023).

[63] Z.; Yue, H.; Guo, Y. Cheng, Z. Yue, H. Guo, and Y. Cheng, “Toxicity of Perovskite Solar

Cells," Energies 2023, Vol. 16, Page 4007 **16**(10), 4007 (2023).

[64] R.R. Lauwerys, A. Kivits, M. Lhoir, P. Rigolet, D. Houbeau, J.P. Buchet, and H.A. Roels, "Biological surveillance of workers exposed to dimethylformamide and the influence of skin protection on its percutaneous absorption," Int. Arch. Occup. Environ. Health **45**(3), 189–203 (1980).

[65] R. Wrbitzky, "Liver function in workers exposed to N,N-dimethylformamide during the production of synthetic textiles," Int. Arch. Occup. Environ. Health **72**(1), 19–25 (1999).

[66] J. Xie, H. Wu, L. Zhang, J. Yu, G. You, Y. Zhou, G. Wu, and H. Chen, "Green solvent engineering of quasi-two-dimensional Dion-Jacobson perovskite films for efficient solar cells," Chemical Engineering Journal **509**, 161466 (2025).

[67] P.W.K. Fong, and G. Li, "The Challenge of Ambient Air–Processed Organometallic Halide Perovskite: Technology Transfer From Spin Coating to Meniscus Blade Coating of Perovskite Thin Films," Front. Mater. **8**, (2021).

[68] J.B. Whitaker, D.H. Kim, B.W. Larson, F. Zhang, J.J. Berry, M.F.A.M. Van Hest, and K. Zhu, "Scalable slot-die coating of high performance perovskite solar cells," Sustain. Energy Fuels **2**(11), 2442–2449 (2018).

[69] Y. Yang, Z. Xue, L. Chen, C.F.J. Lau, and Z. Wang, "Large-area perovskite films for PV applications: A perspective from nucleation and crystallization," Journal of Energy Chemistry **59**, 626–641 (2021).

[70] A.U.I. Shah, and E.L. Meyer, "Perovskite-based solar cells in photovoltaics for commercial scalability: Current progress, challenges, mitigations and future prospectus," Solar Energy **286**, (2025).

[71]"Doctor Blade Coating: Method, Coating Thickness and Design | Ossila," (n.d.).

[72] C. Chen, C. Ran, Q. Yao, J. Wang, C. Guo, L. Gu, H. Han, X. Wang, L. Chao, Y. Xia, Y. Chen, C. Chen, C. Ran, L. Gu, X. Wang, Q. Yao, J. Wang, C. Guo, H. Han, L. Chao, Y. Xia, and Y. Chen, "Screen-Printing Technology for Scale Manufacturing of Perovskite Solar Cells," (2023).

[73] R. Patidar, D. Burkitt, K. Hooper, D. Richards, and T. Watson, "Slot-die coating of perovskite solar cells: An overview," Mater. Today Commun. **22**, (2020).

[74] W. Zi, Z. Jin, S. Liu, and B. Xu, "Flexible perovskite solar cells based on green, continuous roll-to-roll printing technology," Journal of Energy Chemistry **27**(4), 971–989 (2018).

[75] S. Sumaiya, K. Kardel, and A. El-Shahat, "Organic Solar Cell by Inkjet Printing—An Overview," Technologies 2017, Vol. 5, Page 53 **5**(3), 53 (2017).

[76] N. Bhati, M.K. Nazeeruddin, and F. Maréchal, "Evaluating the role of inkjet printing in perovskite solar modules manufacturing using mathematical modeling," Comput. Chem. Eng. **186**, 108687 (2024).

[77] Z. Zhang, Z. Li, Y. Chen, Z. Zhang, K. Fan, S. Chen, L. Liu, and S. Chen, "Progress on Inkjet Printing Technique for Perovskite Films and Their Optoelectronic and Optical Applications," ACS Photonics **10**(10), 3435–3450 (2023).

[78] A.G. Ulyashin, A. Hadjadj, and M.A. Butt, "Thin-Film Coating Methods: A Successful Marriage of High-Quality and Cost-Effectiveness—A Brief Exploration," Coatings 2022, Vol. 12, Page 1115 **12**(8), 1115 (2022).

[79] N. Bhati, M.K. Nazeeruddin, and F. Maréchal, "Critical analysis of decision variables for high-throughput experimentation (HTE) with perovskite solar cells," Solar Energy **262**, (2023).

[80] W. Fu, A.G. Ricciardulli, Q.A. Akkerman, R.A. John, M.M. Tavakoli, S. Essig, M. V. Kovalenko, and M. Saliba, "Stability of perovskite materials and devices," Materials Today **58**, 275–296 (2022).

[81] T.T. Ava, A. Al Mamun, S. Marsillac, and G. Namkoong, "A review: Thermal stability of methylammonium lead halide based perovskite solar cells," Applied Sciences (Switzerland) **9**(1), (2019).

[82] N.K. Elumalai, M.A. Mahmud, D. Wang, and A. Uddin, "Perovskite Solar Cells: Progress and Advancements," Energies 2016, Vol. 9, Page 861 **9**(11), 861 (2016).

[83] T.D. Raju, V. Murugadoss, K.A. Nirmal, T.D. Dongale, A.V. Kesavan, and T.G. Kim, "Advancements in perovskites for solar cell commercialization: A review," Advanced Powder Materials **4**(2), 100275 (2025).

[84] M. Afroz, R.K. Ratnesh, S. Srivastava, and J. Singh, "Perovskite solar cells: Progress, challenges, and future avenues to clean energy," Solar Energy **287**, 113205 (2025).

[85] G.G. Njema, J.K. Kibet, and S.M. Ngari, "A review of interface engineering characteristics for high performance perovskite solar cells," Measurement: Energy **2**, 100005 (2024).

[86] X. Cui, J. Jin, Q. Tai, and F. Yan, "Recent Progress on the Phase Stabilization of FAPbI3 for High-Performance Perovskite Solar Cells," Solar RRL **6**(10), 2200497 (2022).

[87] Q. Li, Y. Liu, Y. Zhang, M. Hu, Z. Yang, and S. Liu, "Synergistic enhancement of Cs and Br doping in formamidinium lead halide perovskites for high performance optoelectronics," CrystEngComm **20**(37), 5510–5518 (2018).

[88] Z. Wang, C. Gong, C. Zhang, C. Zhao, T.-S. Su, H. Li, and H. Zhang, "Recent advances in interfacial engineering for high-efficiency perovskite photovoltaics," (2025).

[89] Q. Sun, X. Meng, J. Deng, B. Shen, D. Hu, B. Kang, and S.R.P. Silva, "Buried interface defects passivation of perovskite film by choline halide for high performance inverted perovskite solar cells with efficiency exceeding 22%," J. Alloys Compd. **959**, 170478 (2023).

[90] X. Wu, G. Xiong, Z. Yue, Z. Dong, and Y. Cheng, "Defect passivation engineering of wide-bandgap perovskites for high-performance solar cells," This Journal Is Cite This:

Mater. Chem. Front **8**, 800 (2024).

[91] Z. Dai, S.K. Yadavalli, M. Chen, A. Abbaspourtamijani, Y. Qi, and N.P. Padture, "Interfacial toughening with self-Assembled monolayers enhances perovskite solar cell reliability," Science (1979). **372**(6542), 618–622 (2021).

[92] A. Al-Ashouri, A. Magomedov, M. Roß, M. Još, M. Talaikis, G. Chistiakova, T. Bertram, J.A. Má rquez, E. Kö hnen, E. Kasparavič ius, S. Levcenco, L. Gil-Escrig, C.J. Hages, R. Schlatmann, B. Rech, dg Tadas Malinauskas, T. Unold, C.A. Kaufmann, L. Korte, G. Niaura, V. Getautis, and S. Albrecht, "Conformal monolayer contacts with lossless interfaces for perovskite single junction and monolithic tandem solar cells," Energy Environ. Sci **12**, 3356 (2019).

[93] D.Y. Heo, W.J. Jang, and S.Y. Kim, "Recent review of interfacial engineering for perovskite solar cells: effect of functional groups on the stability and efficiency," Mater. Today Chem. **26**, 101224 (2022).

[94] J.H. Lee, D. Shin, R. Rhee, S. Yun, K.M. Yeom, D.H. Chun, S. Lee, D. Kim, Y. Yi, J.H. Noh, and J.H. Park, "Band Alignment Engineering between Planar SnO2 and Halide Perovskites via Two-Step Annealing," Journal of Physical Chemistry Letters **10**(21), 6545–6550 (2019).

[95] D. Yang, X. Zhou, R. Yang, Z. Yang, W. Yu, X. Wang, C. Li, S. Liu, and R.P.H. Chang, "Surface optimization to eliminate hysteresis for record efficiency planar perovskite solar cells," Energy Environ. Sci. **9**(10), 3071–3078 (2016).

[96] B. Xiao, W. Zhang, Y. Xiong, Y. Huang, C. Huang, Y. Qian, G. Shen, A. Basit, Y. Luo, X. Li, and J. Yang, "Energy Level Alignment Regulation and Carrier Management in Perovskite Solar Cells with Various Bandgaps Using Tailored Metal-Organic Frameworks," Adv. Funct. Mater. **35**(11), 2417293 (2025).

[97] T. Wang, M. Xie, S. Abbasi, Z. Cheng, H. Liu, and W. Shen, "High efficiency perovskite solar cells with tailorable surface wettability by surfactant," J. Power Sources **448**, 227584 (2020).

[98] J. Han, H. Kwon, E. Kim, D.W. Kim, H.J. Son, and D.H. Kim, "Interfacial engineering of a ZnO electron transporting layer using self-assembled monolayers for high performance and stable perovskite solar cells," J. Mater. Chem. A Mater. **8**(4), 2105–2113 (2020).

[99] W. Yang, Y. Zhang, C. Xiao, J. Yang, and T. Shi, "A review of encapsulation methods and geometric improvements of perovskite solar cells and modules for mass production and commercialization," Nano Materials Science, (2025).

[100] K. Lochhead, E. Johlin, D. Yang, K. Lochhead, E. Johlin, and D. Yang, "Encapsulation of Perovskite Solar Cells with Thin Barrier Films," Thin Films - Deposition Methods and Applications, (2022).

[101] Q.Q. Chu, Z. Sun, D. Wang, B. Cheng, H. Wang, C.P. Wong, and B. Fang, "Encapsulation: The path to commercialization of stable perovskite solar cells," Matter **6**(11), 3838–3863 (2023).

[102] Y. Wang, I. Ahmad, T. Leung, J. Lin, W. Chen, F. Liu, A.M.C. Ng, Y. Zhang, and A.B. Djurišić, "Encapsulation and Stability Testing of Perovskite Solar Cells for Real Life Applications," ACS Materials Au **2**(3), 215–236 (2022).

[103] J.M. Choi, H. Suko, K. Kim, J. Han, S. Lee, Y. Matsuo, S. Maruyama, I. Jeon, and H. Daiguji, "Multi-Walled Carbon Nanotube-Assisted Encapsulation Approach for Stable Perovskite Solar Cells," Molecules 2021, Vol. 26, Page 5060 **26**(16), 5060 (2021).

[104] J. Martins, S. Emami, R. Madureira, J. Mendes, D. Ivanou, and A. Mendes, "Novel laser-assisted glass frit encapsulation for long-lifetime perovskite solar cells," J. Mater. Chem. A Mater. **8**(38), 20037–20046 (2020).

[105] Y. Zhou, Y. Yin, X. Zuo, L. Wang, T. De Li, Y. Xue, A. Subramanian, Y. Fang, Y. Guo, Z. Yang, M. Cotlet, C.Y. Nam, and M.H. Rafailovich, "Improving Thermal Stability of Perovskite Solar Cells by Suppressing Ion Migration Using Copolymer Grain Encapsulation," Chemistry of Materials **33**(15), 6120–6135 (2021).

[106]*Deposition Sources* (n.d.).

[107]"Kurt J. Lesker Company | Thermal & Resistive Evaporation Sources | Enabling Technology for a Better World," (n.d.).

[108]"Kurt J Lesker Nano-36 Thermal Evaporator Standard Operating Procedure (SOP)," (n.d.).

[109]"Sputter Coater for SEM: Important Insights You Must Know | Torontech," Https://Torontech.Com/Sputter-Coater-for-Sem/, (2024).

[110] Antonis Nanakoudis, "Scanning Electron Microscopy - SEM - Advancing Materials," Https://Www.Thermofisher.Com/Blog/Materials/What-Is-Sem-Scanning-Electron-Microscopy-Explained/, (2019).

[111]*SPM SmartSPM™-1000 Instruction Manual* (2007).

[112]"How does AFM work?," (n.d.).

[113] M. Li, K. Xun, X. Zhu, D. Liu, X. Liu, X. Jin, and M. Wu, "Research on AFM tip-related nanofabrication of two-dimensional materials," Nanotechnol. Rev. **12**(1), (2023).

[114]"AFM Modes," Https://Www.Nanophys.Kth.Se/Nanolab/Afm/Icon/Bruker-Help/Content/SPM%20Training%20Guide/Atomic%20Force%20Microscopy%20%28AFM%29/AFM%20Modes.Htm, (n.d.).

[115] Park Systems Corp., "Kelvin Probe Force Microscopy (KPFM) | Park Systems," Https://Www.Parksystems.Com/En/Products/Research-Afm/AFM-Modes/Electrical-Modes/Kelvin-Probe-Force-Microscopy--Kpfm-, (2024).

[116] Inc. PerkinElmer, “LAMBDA 1050+ UV/Vis/NIR Spectrophotometer | PerkinElmer,” Https://Www.Perkinelmer.Com/Product/Lambda-1050-2d-Base-Inst-No-Sw-L6020055, (n.d.).

[117] Inc. Agilent Technologies, *The Basics of UV-Vis (Publication No. 5980-1397EN)* (2021).

[118] B.L. Diffey, “Sources and measurement of ultraviolet radiation,” Methods **28**(1), 4–13 (2002).

[119] J. Eymard, R. Clerc, V. Duveiller, B. Commault, and M. Hebert, “Characterization of UV–Vis–NIR optical constants of encapsulant for accurate determination of absorption and backscattering losses in photovoltaics modules,” Solar Energy Materials and Solar Cells, (2022).

[120] I. PerkinElmer, *LAMBDA UV/Vis and UV/Vis/NIR Spectrophotometers* (Waltham, 2012).

[121] L.B. Cheah, R.A.M. Osman, and P. Poopalan, “Ga 2 O 3 thin films by sol-gel method its optical properties,” in *AIP Conf. Proc.*, (American Institute of Physics Inc., 2020).

[122] T. Yan, X. Wang, S. Liu, D. Fan, X. Xu, Q. Zeng, H. Xie, X. Yang, S. Zhu, X. Ma, Z. Yuan, and X. Chen, “Confocal Laser Scanning Microscopy Based on a Silicon Photomultiplier for Multicolor In Vivo Imaging in Near-Infrared Regions I and II,” Small Methods **6**(12), (2022).

[123]*Zeiss LSM780, Confocal Microscope System* (n.d.).

[124] Dutrow L. Barbara, and Clark M. Christine, “X-ray Powder Diffraction (XRD),” Https://Serc.Carleton.Edu/207663, (2018).

[125] Henry Darrell, Eby Nelson, Goodge John, and Mogk David, “X-ray reflection in accordance with Bragg’s Law,” Https://Serc.Carleton.Edu/Research_education/Geochemsheets/BraggsLaw.Html, (2007).

[126]“The International Centre for Diffraction Data -,” Https://Www.Icdd.Com/, (n.d.).

[127] S. Sharma, and S.K. Sharma, “Diverse morphology zinc oxide films formulations and characterizations,” in *Nanostructured Zinc Oxide: Synthesis, Properties and Applications*, (Elsevier, 2021), pp. 57–92.

[128] Wright Andrew, “X-ray Photoelectron Spectroscopy APPLICATION NOTE,” (2019).

[129]*X-Ray Photoelectron Spectroscopy Spectroscopy for Chemical Analysis* (2022).

[130]“Photoelectron Spectroscopy | Ultraviolet Photoelectron Spectroscopy - DE,” (n.d.).

[131] P.S. Bagus, and H.J. Freund, “X-ray photoelectron spectroscopy as a useful tool to study surfaces and model systems for heterogeneous catalysts: A review and perspective,” Surf. Sci. **745**, 122471 (2024).

[132] Jeong Jay, “PHOTOVOLTAICS: Enhancements enable solar simulators to shed light on new photovoltaic designs | Laser Focus World,” Https://Www.Laserfocusworld.Com/Test-Measurement/Test-Measurement/Article/16553008/Photovoltaics-Enhancements-Enable-

Solar-Simulators-to-Shed-Light-on-New-Photovoltaic-Designs, (2007).

[133]"Solar Simulator - Basic Knowledge and Working Principles - EnliTech," (2022).

[134] A.R. Murad, A. Iraqi, S.B. Aziz, S.N. Abdullah, and M.A. Brza, "Conducting Polymers for Optoelectronic Devices and Organic Solar Cells: A Review," Polymers 2020, Vol. 12, Page 2627 **12**(11), 2627 (2020).

[135] M.A. Ansari, G. Ciampi, and S. Sibilio, "Tackling Efficiency Challenges and Exploring Greenhouse-Integrated Organic Photovoltaics," Energies 2023, Vol. 16, Page 6076 **16**(16), 6076 (2023).

[136] A. These, L.J.A. Koster, C.J. Brabec, and V.M. Le Corre, "Beginner's Guide to Visual Analysis of Perovskite and Organic Solar Cell Current Density–Voltage Characteristics," Adv. Energy Mater. **14**(21), 2400055 (2024).

[137] K. Jäger, O. Isabella, A. Smets, R. Swaaij, and M. Zeman, *Solar Energy. Fundamentals, Technology, and Systems* (Delft University of Technology, 2014).

[138]"Oriel IQE-200 | MKS/Newport | Oct 2009 | Photonics Spectra," (n.d.).

[139] M. Kaikanov, D. Nauruzbayev, A. Abduvalov, and K. Baigarin, "Investigation of intense pulsed ion beam generation by a magnetically insulated ion diode at a reduced impedance," Vacuum **217**, 112496 (2023).

[140] E. Kim, A.L. Ramos Figueroa, M. Schrock, E. Zhang, C.J. Newcomb, Z. Bao, and L. Michalek, "A guide for nanomechanical characterization of soft matter via AFM: From mode selection to data reporting," STAR Protoc. **6**(2), (2025).

[141] R. García, "Amplitude Modulation Atomic Force Microscopy," Amplitude Modulation Atomic Force Microscopy, (2010).

[142] J. Rydz, A. Šišková, and A. Andicsová Eckstein, "Scanning Electron Microscopy and Atomic Force Microscopy: Topographic and Dynamical Surface Studies of Blends, Composites, and Hybrid Functional Materials for Sustainable Future," Advances in Materials Science and Engineering **2019**, (2019).

[143] E. Nagao, and J.A. Dvorak, "Phase imaging by atomic force microscopy: Analysis of living homoiothermic vertebrate cells," Biophys. J. **76**(6), 3289–3297 (1999).

[144] D. Mourtzis, F. Tao, B. Wang, A. Riel, S. Huang, E. Carpanzano, D. Marilena, D.' Addona, E. Werner, U. Güth, B. Brockhagen, C. Döpke, and A. Ehrmann, "Examination of Polymer Blends by AFM Phase Images," Technologies 2023, Vol. 11, Page 56 **11**(2), 56 (2023).

[145] B. Cao, H. Liu, L. Yang, X. Li, H. Liu, P. Dong, X. Mai, C. Hou, N. Wang, J. Zhang, J. Fan, Q. Gao, and Z. Guo, "Interfacial Engineering for High-Efficiency Nanorod Array-Structured Perovskite Solar Cells," ACS Appl. Mater. Interfaces **11**(37), 33770–33780 (2019).

[146] Y. Wang, M. Zhong, and L. Chai, “Effective control of the length of ZnO-TiO2 nanorod arrays as electron transport layer of perovskite solar cells with enhanced performance,” Mater. Sci. Semicond. Process. **91**, 66–72 (2019).

[147] M.M. Tavakoli, D. Prochowicz, P. Yadav, R. Tavakoli, and M. Saliba, “Engineered Science COMMUNICATION Zinc Stannate Nanorod as an Electron Transporting Layer for Highly Efficient and Hysteresis-less Perovskite Solar Cells,” (2018).

[148] K. Chen, W. Tang, Y. Chen, R. Yuan, Y. Lv, W. Shan, and W.H. Zhang, “A facile solution processed ZnO@ZnS core–shell nanorods arrays for high-efficiency perovskite solar cells with boosted stability,” Journal of Energy Chemistry **61**, 553–560 (2021).

[149] J.M. Kim, B.S. Lee, and S.W. Hwang, “High-Performance Core/Shell of ZnO/TiO2 Nanowire with AgCl-Doped CdSe Quantum Dots Arrays as Electron Transport Layer for Perovskite Solar Cells,” Molecules 2020, Vol. 25, Page 3969 **25**(17), 3969 (2020).

[150] W.Q. Wu, D. Chen, Y.B. Cheng, and R.A. Caruso, “Low-Temperature Solution-Processed Amorphous Titania Nanowire Thin Films for 1 cm2 Perovskite Solar Cells,” ACS Appl. Mater. Interfaces **12**(10), 11450–11458 (2020).

[151] J. Sun, N. Li, L. Dong, X. Niu, M. Zhao, Z. Xu, H. Zhou, C. Shan, and C. Pan, “Interfacial-engineering enhanced performance and stability of ZnO nanowire-based perovskite solar cells,” Nanotechnology **32**(47), 475204 (2021).

[152] A. Asadzade, and S. Andalibi Miandoab, “Design and simulation of 3D perovskite solar cells based on titanium dioxide nanowires to achieve high-efficiency,” Solar Energy **228**, 550–561 (2021).

[153] M. Irfan, F. Ünlü, K. Lê, T. Fischer, H. Ullah, and S. Mathur, “Electrospun Networks of ZnO-SnO2 Composite Nanowires as Electron Transport Materials for Perovskite Solar Cells,” J. Nanomater. **2022**(1), 6043406 (2022).

[154] A.M. Elseman, Q.L. Song, A.H. Zaki, A.E. Shalan, and M.M. Rashad, “TiO2 nanotubes: An advanced electron transport material for enhancing the efficiency and stability of perovskite solar cells,” Ind. Eng. Chem. Res. **59**(41), 18549–18557 (2020).

[155] H. Tang, Q. Cao, Z. He, S. Wang, J. Han, T. Li, B. Gao, J. Yang, D. Deng, and X. Li, “SnO2–Carbon Nanotubes Hybrid Electron Transport Layer for Efficient and Hysteresis-Free Planar Perovskite Solar Cells,” Solar RRL **4**(1), 1900415 (2020).

[156] M.K.A. Mohammed, and M. Shekargoftar, “Surface treatment of ZnO films with carbon nanotubes for efficient and stable perovskite solar cells,” Sustain. Energy Fuels **5**(2), 540–548 (2021).

[157] A. Khorasani, M. Marandi, A. Iraji zad, and N. Taghavinia, “Application of combinative TiO2nanorods and nanoparticles layer as the electron transport film in highly efficient mixed halides perovskite solar cells,” Electrochim. Acta **297**, 1071–1078 (2019).

[158] L. Yang, X. Wang, X. Mai, T. Wang, C. Wang, X. Li, V. Murugadoss, Q. Shao, S. Angaiah, and Z. Guo, "Constructing efficient mixed-ion perovskite solar cells based on TiO2 nanorod array," J. Colloid Interface Sci. **534**, 459–468 (2019).

[159] M. Wang, J. Duan, J. Du, X. Yang, Y. Duan, T. Zhang, and Q. Tang, "High-Efficiency All-Inorganic Perovskite Solar Cells Tailored by Scalable Rutile TiO2Nanorod Arrays with Excellent Stability," ACS Appl. Mater. Interfaces **13**(10), 12091–12098 (2021).

[160] X. Li, S.M. Dai, P. Zhu, L.L. Deng, S.Y. Xie, Q. Cui, H. Chen, N. Wang, and H. Lin, "Efficient Perovskite Solar Cells Depending on TiO2 Nanorod Arrays," ACS Appl. Mater. Interfaces **8**(33), 21358–21365 (2016).

[161] C. Liu, R. Zhu, A. Ng, Z. Ren, S.H. Cheung, L. Du, S.K. So, J.A. Zapien, A.B. Djurišić, D. Lee Phillips, and C. Surya, "Investigation of high performance TiO2 nanorod array perovskite solar cells," J. Mater. Chem. A Mater. **5**(30), 15970–15980 (2017).

[162] K. Manseki, T. Ikeya, A. Tamura, T. Ban, T. Sugiura, and T. Yoshida, "Mg-doped TiO2 nanorods improving open-circuit voltages of ammonium lead halide perovskite solar cells," RSC Adv. **4**(19), 9652–9655 (2014).

[163] Y. Li, Y. Guo, Y. Li, and X. Zhou, "Fabrication of Cd-Doped TiO2 Nanorod Arrays and Photovoltaic Property in Perovskite Solar Cell," Electrochim. Acta **200**, 29–36 (2016).

[164] S. Wu, C. Chen, J. Wang, J. Xiao, and T. Peng, "Controllable Preparation of Rutile TiO2 Nanorod Array for Enhanced Photovoltaic Performance of Perovskite Solar Cells," ACS Appl. Energy Mater. **1**(4), 1649–1657 (2018).

[165] Q. Cui, X. Zhao, H. Lin, L. Yang, H. Chen, Y. Zhang, and X. Li, "Improved efficient perovskite solar cells based on Ta-doped TiO2 nanorod arrays," Nanoscale **9**(47), 18897–18907 (2017).

[166] Y. Lv, Y. Li, H. Sun, Y. Guo, Y. Li, J. Tan, and X. Zhou, "Yttrium-doped TiO2 nanorod arrays and application in perovskite solar cells for enhanced photocurrent density," Thin Solid Films **651**, 117–123 (2018).

[167] G. Xiao, C. Shi, K. Lv, C. Ying, and Y. Wang, "Nb-Doping TiO2 Electron Transporting Layer for Efficient Perovskite Solar Cells," ACS Appl. Energy Mater. **1**(6), 2576–2581 (2018).

[168] D.K. Jarwal, A. Kumar, A.K. Mishra, S. Ratan, C. Kumar, D. Upadhyay, B. Mukherjee, and S. Jit, "Efficiency Improvement of TiO2 Nanorods Electron Transport Layer Based Perovskite Solar Cells by Solvothermal Etching," IEEE J. Photovolt. **9**(6), 1699–1707 (2019).

[169] Y. Lv, R. Yuan, B. Cai, B. Bahrami, A.H. Chowdhury, C. Yang, Y. Wu, Q. Qiao, S. (Frank) Liu, and W.-H. Zhang, "High-Efficiency Perovskite Solar Cells Enabled by Anatase TiO2 Nanopyramid Arrays with an Oriented Electric Field," Angewandte Chemie **132**(29),

12067–12074 (2020).

[170] M.M. Maitani, H. Satou, A. Ohmura, S. Tsubaki, and Y. Wada, “Crystalline orientation control using self-assembled TiO2 nanosheet scaffold to improve CH3NH3PbI3 perovskite solar cells,” Jpn. J. Appl. Phys. **56**(8), 08MC17 (2017).

[171] S. Jiao, X. Fu, G. Lian, L. Jing, Z. Xu, Q. Wang, and D. Cui, “Ultrathin TiO 2 nanosheets synthesized using a high pressure solvothermal method and the enhanced photoresponse performance of CH 3 NH 3 PbI 3 –TiO 2 composite films,” RSC Adv. **7**(34), 20845–20850 (2017).

[172] W.Q. Wu, F. Huang, D. Chen, Y.B. Cheng, and R.A. Caruso, “Thin Films of Dendritic Anatase Titania Nanowires Enable Effective Hole-Blocking and Efficient Light-Harvesting for High-Performance Mesoscopic Perovskite Solar Cells,” Adv. Funct. Mater. **25**(21), 3264–3272 (2015).

[173] H. Tao, W. Ke, J. Wang, Q. Liu, J. Wan, G. Yang, and G. Fang, “Perovskite solar cell based on network nanoporous layer consisted of TiO2 nanowires and its interface optimization,” J. Power Sources **290**, 144–152 (2015).

[174] Y. Yu, J. Li, D. Geng, J. Wang, L. Zhang, T.L. Andrew, M.S. Arnold, and X. Wang, “Development of lead iodide perovskite solar cells using three-dimensional titanium dioxide nanowire architectures,” ACS Nano **9**(1), 564–572 (2015).

[175] H.M.A. Javed, M.I. Ahmad, W. Que, A.A. Qureshi, M. Sarfaraz, S. Hussain, M.Z. Iqbal, M. Zubair Nisar, M. Shahid, and T.S. AlGarni, “Encapsulation of TiO2 nanotubes with Cs nanoparticles to enhance electron injection and thermal stability of perovskite solar cells,” Surfaces and Interfaces **23**, 101033 (2021).

[176] N. Alias, A. Ali Umar, N.A.A. Malek, K. Liu, X. Li, N.A. Abdullah, M.M. Rosli, M.Y.A. Rahman, Z. Shi, X. Zhang, H. Zhang, F. Liu, J. Wang, and Y. Zhan, “Photoelectrical dynamics uplift in perovskite solar cells by atoms thick 2D TiS2layer passivation of TiO2nanograss electron transport layer,” ACS Appl. Mater. Interfaces **13**(2), 3051–3061 (2021).

[177] S.S. Mali, C.S. Shim, H. Kim, C.A. Betty, P.S. Patil, and C.K. Hong, “Secondary Hydrothermally Processed Engineered Titanium Dioxide Nanostructures for Efficient Perovskite Solar Cells,” Energy Technology **5**(10), 1775–1787 (2017).

[178] F. Yu, G.S. Han, Y.J. Tu, H.S. Roh, and J.K. Lee, “Electron extraction mechanism in low hysteresis perovskite solar cells using single crystal TiO2 nanorods,” Solar Energy **167**, 251–257 (2018).

[179] D. Huh, K.S. Oh, M. Kim, H.J. Choi, D.S. Kim, and H. Lee, “Selectively patterned TiO2 nanorods as electron transport pathway for high performance perovskite solar cells,” Nano Res. **12**(3), 601–606 (2019).

[180] S.S. Azad, R. Keshavarzi, V. Mirkhani, M. Moghadam, S. Tangestaninejad, and I. Mohammadpoor-Baltork, "Stability enhancement of perovskite solar cells using multifunctional inorganic materials with UV protective, self cleaning, and high wear resistance properties," Sci. Rep. **14**(1), (2024).

[181] N. Islavath, E. Ramasamy, D. Das, and S. V. Joshi, "Spray coated seed layer for scalable synthesis of aligned ZnO nanowire arrays on FTO substrate and their photovoltaic properties," Ceram. Int. **41**(3), 4118–4122 (2015).

[182] R. Zhang, C. Fei, B. Li, H. Fu, J. Tian, and G. Cao, "Continuous Size Tuning of Monodispersed ZnO Nanoparticles and Its Size Effect on the Performance of Perovskite Solar Cells," ACS Appl. Mater. Interfaces **9**(11), 9785–9794 (2017).

[183] Z. Zhang, 张振雲, L. Xu, 许磊, J. Qi, and 齐俊杰, "Improved efficiency and stability of perovskite solar cells with molecular ameliorating of ZnO nanorod/perovskite interface and Mg-doping ZnO*," Chinese Physics B **30**(3), 038801 (2021).

[184] M.S. Selim, A.M. Elseman, and Z. Hao, "ZnO Nanorods: An Advanced Cathode Buffer Layer for Inverted Perovskite Solar Cells," ACS Appl. Energy Mater. **3**(12), 11781–11791 (2020).

[185] R. Irandoost, and S. Soleimani-Amiri, "Design and analysis of high efficiency perovskite solar cell with ZnO nanorods and plasmonic nanoparticles," Optik (Stuttg). **202**, 163598 (2020).

[186] S. Yun, T. Guo, Y. Li, X. Gao, A. Huang, and L. Kang, "Well-ordered vertically aligned ZnO nanorods arrays for high-performance perovskite solar cells," Mater. Res. Bull. **130**, 110935 (2020).

[187] S. Li, P. Zhang, Y. Wang, H. Sarvari, D. Liu, J. Wu, Y. Yang, Z. Wang, and Z.D. Chen, "Interface engineering of high efficiency perovskite solar cells based on ZnO nanorods using atomic layer deposition," Nano Res. **10**(3), 1092–1103 (2017).

[188] Y. Wang, M. Zhong, W. Wang, Q. Wang, W. Wu, and X. Luo, "Effects of ZnSe modification on the perovskite films and perovskite solar cells based on ZnO nanorod arrays," Appl. Surf. Sci. **495**, 143552 (2019).

[189] S. Bhatt, R. Shukla, C. Pathak, and S.K. Pandey, "Evaluation of performance constraints and structural optimization of a core-shell ZnO nanorod based eco-friendly perovskite solar cell," Solar Energy **215**, 473–481 (2021).

[190] Y. Zhang, G. Zhai, L. Gao, Q. Chen, J. Ren, J. Yu, Y. Yang, Y. Hao, X. Liu, B. Xu, and Y. Wu, "Improving performance of perovskite solar cells based on ZnO nanorods via rod-length control and sulfidation treatment," Mater. Sci. Semicond. Process. **117**, 105205 (2020).

[191] K. Sekar, R. Doineau, S. Mayarambakam, B. Schmaltz, and G. Poulin-Vittrant, "Control

of ZnO nanowires growth in flexible perovskite solar cells: A mini-review," Heliyon **10**(3), e24706 (2024).

[192] S. Li, P. Zhang, Y. Wang, H. Sarvari, D. Liu, J. Wu, Y. Yang, Z. Wang, Z.D. Chen, and S.-V. Berlin, *Interface Engineering of High Efficiency Perovskite Solar Cells Based on ZnO Nanorods Using Atomic Layer Deposition* (n.d.).

[193] C. Liu, W. Wu, D. Zhang, Z. Li, G. Ren, W. Han, and W. Guo, "Effective stability enhancement in ZnO-based perovskite solar cells by MACl modification," J. Mater. Chem. A Mater. **9**(20), 12161–12168 (2021).

[194] T. Chen, J. Xie, and P. Gao, "Ultraviolet Photocatalytic Degradation of Perovskite Solar Cells: Progress, Challenges, and Strategies," Advanced Energy and Sustainability Research **3**(6), (2022).

[195] J. Kim, K.S. Kim, and C.W. Myung, "Efficient electron extraction of SnO2 electron transport layer for lead halide perovskite solar cell," NPJ Comput. Mater. **6**(1), (2020).

[196] V.N. Jafarova, and G.S. Orudzhev, "Structural and electronic properties of ZnO: A first-principles density-functional theory study within LDA(GGA) and LDA(GGA)+U methods," Solid State Commun. **325**, (2021).

[197] M. Nabil, I. V. Perez-Quintana, M. Acosta, J.A. Mendez-Gamboa, and R. Castro-Rodriguez, "Morphological, Structural, and Optical Bandgap Characterization of Extracted ZnO Nanoparticles from Commercial Paste," Advances in Materials Science and Engineering **2021**, (2021).

[198] Z. Qian, L. Chen, J. Wang, L. Wang, Y. Xia, X. Ran, P. Li, Q. Zhong, L. Song, P. Müller-Buschbaum, Y. Chen, and H. Zhang, "Manipulating SnO2 Growth for Efficient Electron Transport in Perovskite Solar Cells," Adv. Mater. Interfaces **8**(10), 2100128 (2021).

[199] C.H. Chiang, C.W. Kan, and C.G. Wu, "Synergistic Engineering of Conduction Band, Conductivity, and Interface of Bilayered Electron Transport Layers with Scalable TiO2and SnO2Nanoparticles for High-Efficiency Stable Perovskite Solar Cells," ACS Appl. Mater. Interfaces **13**(20), 23606–23615 (2021).

[200] S. Ullah, M.F.U. Din, J. Khan Kasi, A. Khan Kasi, K. Vegso, M. Kotlar, M. Micusik, M. Jergel, V. Nadazdy, P. Siffalovic, E. Majkova, and A. Fakharuddin, "Mesoporous SnO2Nanoparticle-Based Electron Transport Layer for Perovskite Solar Cells," ACS Appl. Nano Mater. **5**(6), 7822–7830 (2022).

[201] X. Zhang, Y. Rui, Y. Wang, J. Xu, H. Wang, Q. Zhang, and P. Müller-Buschbaum, "SnO2 nanorod arrays with tailored area density as efficient electron transport layers for perovskite solar cells," J. Power Sources **402**, 460–467 (2018).

[202] Y. Lv, P. Wang, B. Cai, Q. Ma, X. Zheng, Y. Wu, Q. Jiang, J. Liu, and W.H. Zhang, "Facile Fabrication of SnO2 Nanorod Arrays Films as Electron Transporting Layer for

Perovskite Solar Cells," Solar RRL **2**(9), 1800133 (2018).

[203] Y. Xu, Y. Rui, X. Wang, B. Li, Z. Jin, Y. Wang, and Q. Zhang, "Boosted charge extraction of SnO2 nanorod arrays via nanostructural and surface chemical engineering for efficient and stable perovskite solar cells," Appl. Surf. Sci. **607**, 154986 (2023).

[204] X. Xu, Z. Xu, J. Tang, X. Zhang, L. Zhang, J. Wu, and Z. Lan, "High-performance planar perovskite solar cells based on low-temperature solution-processed well-crystalline SnO2 nanorods electron-transporting layers," Chemical Engineering Journal **351**, 391–398 (2018).

[205] Y. Wang, C. Duan, J. Li, W. Han, M. Zhao, L. Yao, Y. Wang, C. Yan, and T. Jiu, "Performance Enhancement of Inverted Perovskite Solar Cells Based on Smooth and Compact PC61BM:SnO2 Electron Transport Layers," ACS Appl. Mater. Interfaces **10**(23), 20128–20135 (2018).

[206] Q. Liu, M.C. Qin, W.J. Ke, X.L. Zheng, Z. Chen, P.L. Qin, L. Bin Xiong, H.W. Lei, J.W. Wan, J. Wen, G. Yang, J.J. Ma, Z.Y. Zhang, and G.J. Fang, "Enhanced Stability of Perovskite Solar Cells with Low-Temperature Hydrothermally Grown SnO2 Electron Transport Layers," Adv. Funct. Mater. **26**(33), 6069–6075 (2016).

[207] W.Q. Wu, D. Chen, Y.B. Cheng, and R.A. Caruso, "Thin Films of Tin Oxide Nanosheets Used as the Electron Transporting Layer for Improved Performance and Ambient Stability of Perovskite Photovoltaics," Solar RRL **1**(11), 1700117 (2017).

[208] K. Mahmood, A. Khalid, F. Nawaz, and M.T. Mehran, "Low-temperature electrospray-processed SnO2 nanosheets as an electron transporting layer for stable and high-efficiency perovskite solar cells," J. Colloid Interface Sci. **532**, 387–394 (2018).

[209] Z. Yelzhanova, G. Nigmetova, D. Aidarkhanov, B. Daniyar, B. Baptayev, M.P. Balanay, A.N. Jumabekov, and A. Ng, "A Morphological Study of Solvothermally Grown SnO2 Nanostructures for Application in Perovskite Solar Cells," Nanomaterials **12**(10), (2022).

[210] F. Babar, U. Mehmood, H. Asghar, M.H. Mehdi, A.U.H. Khan, H. Khalid, N. ul Huda, and Z. Fatima, "Nanostructured photoanode materials and their deposition methods for efficient and economical third generation dye-sensitized solar cells: A comprehensive review," Renewable and Sustainable Energy Reviews **129**, (2020).

[211] Q. Zhou, J.Z. Wen, P. Zhao, and W.A. Anderson, "Synthesis of vertically-aligned zinc oxide nanowires and their application as a photocatalyst," Nanomaterials **7**(1), (2017).

[212] S. Chen, M. Wang, J. Ye, J. Cai, Y. Ma, H. Zhou, and L. Qi, "Kinetics-controlled growth of aligned mesocrystalline SnO2 nanorod arrays for lithium-ion batteries with superior rate performance," Nano Res. **6**(4), 243–252 (2013).

[213]"Water, Reagent (Deionized water), ACS, Thermo Scientific Chemicals | Fisher Scientific," (n.d.).

[214]"Ethanol," (n.d.).

[215] D. Aidarkhanov, Z. Ren, C.K. Lim, Z. Yelzhanova, G. Nigmetova, G. Taltanova, B. Baptayev, F. Liu, S.H. Cheung, M. Balanay, A. Baumuratov, A.B. Djurišić, S.K. So, C. Surya, P.N. Prasad, and A. Ng, "Passivation engineering for hysteresis-free mixed perovskite solar cells," Solar Energy Materials and Solar Cells **215**, (2020).

[216] G.E. Patil, D.D. Kajale, V.B. Gaikwad, and G.H. Jain, "Preparation and characterization of SnO2 nanoparticles by hydrothermal route," International Nano Letters 2012 2:1 **2**(1), 1–5 (2012).

[217] R. Roy, M.M. Byranvand, M.R. Zohdi, T. Magorian Friedlmeier, C. Das, W. Hempel, W. Zuo, M. Kedia, J.J. Rendon, S. Boehringer, B. Hailegnanw, M. Vorochta, S. Mehl, M. Rai, A. Kulkarni, S. Mathur, and M. Saliba, "All-inorganic CsPbI2Br perovskite solar cells with thermal stability at 250 °C and moisture-resilience via polymeric protection layers," Energy Environ. Sci., (2025).

[218] I.M. Maafa, "All-Inorganic Perovskite Solar Cells: Recent Advancements and Challenges," Nanomaterials **12**(10), (2022).

[219] D. Zhang, D. Li, Y. Hu, A. Mei, and H. Han, "Degradation pathways in perovskite solar cells and how to meet international standards," Commun. Mater. **3**(1), (2022).

[220] Y. Liang, F. Li, X. Cui, T. Lv, C. Stampfl, S.P. Ringer, X. Yang, J. Huang, and R. Zheng, "Toward stabilization of formamidinium lead iodide perovskites by defect control and composition engineering," Nat. Commun. **15**(1), (2024).

[221] L. Zhang, G. Luo, W. Zhang, Y. Yao, P. Ren, X. Geng, Y. Zhang, X. Wu, L. Xu, P. Lin, X. Yu, P. Wang, and C. Cui, "Strain Regulation and Defect Passivation of FA-Based Perovskite Materials for Highly Efficient Solar Cells," Advanced Science **11**(7), (2024).

[222] B. Li, Y. Zhang, L. Fu, T. Yu, S. Zhou, L. Zhang, and L. Yin, "Surface passivation engineering strategy to fully-inorganic cubic CsPbI3 perovskites for high-performance solar cells," Nat. Commun. **9**(1), (2018).

[223] A. Marronnier, G. Roma, S. Boyer-Richard, L. Pedesseau, J.M. Jancu, Y. Bonnassieux, C. Katan, C.C. Stoumpos, M.G. Kanatzidis, and J. Even, "Anharmonicity and Disorder in the Black Phases of Cesium Lead Iodide Used for Stable Inorganic Perovskite Solar Cells," ACS Nano **12**(4), 3477–3486 (2018).

[224] T. Ozturk, E. Akman, A.E. Shalan, and S. Akin, "Composition engineering of operationally stable CsPbI 2 Br perovskite solar cells with a record efficiency over 17%," Nano Energy **87**, 106157 (2021).

[225] H. Näsström, P. Becker, J.A. Márquez, O. Shargaieva, R. Mainz, E. Unger, and T. Unold, "Dependence of phase transitions on halide ratio in inorganic CsPb(Br: XI1- x)3perovskite thin films obtained from high-throughput experimentation," J. Mater. Chem. A Mater. **8**(43), 22626–22631 (2020).

[226] Y. Gu, H. Wang, J. Sun, Y. Lu, P. Luo, and J. Hu, “Fabrication of efficient and stable wide band gap CsPbIBr2 inorganic perovskite solar cells via doping with lead chloride compound,” J. Alloys Compd. **963**, 171291 (2023).

[227] Y. Guo, X. Yin, M. Que, J. Zhang, S. Wen, D. Liu, H. Xie, and W. Que, “Quantum dot-modified CsPbIBr2 perovskite absorber for efficient and stable photovoltaics,” Org. Electron. **86**, (2020).

[228] R.J. Sutton, G.E. Eperon, L. Miranda, E.S. Parrott, B.A. Kamino, J.B. Patel, M.T. Hörantner, M.B. Johnston, A.A. Haghighirad, D.T. Moore, and H.J. Snaith, “Bandgap-Tunable Cesium Lead Halide Perovskites with High Thermal Stability for Efficient Solar Cells,” Adv. Energy Mater. **6**(8), (2016).

[229] X. Liu, H. Lian, Z. Zhou, C. Zou, J. Xie, F. Zhang, H. Yuan, S. Yang, Y. Hou, and H.G. Yang, “Stoichiometric Dissolution of Defective CsPbI2Br Surfaces for Inorganic Solar Cells with 17.5% Efficiency,” Adv. Energy Mater. **12**(14), 2103933 (2022).

[230] Z. Wang, S. Wang, G. Yang, Y. Yin, X. Zou, Y. Hao, H. Wang, B. Xu, and S. Yin, “A simple strategy passivating ZnO electron transport layers for realizing high efficiency in organic solar cells,” Surfaces and Interfaces **44**, 103699 (2024).

[231] X. Chen, J. Liu, Z. Xiao, Z. Suo, J. Wang, Z. Yao, C. Li, X. Wan, and Y. Chen, “A hybrid ZnO nanoparticle electron transporting layer for inverted structure organic solar cells with efficiency over 19%,” Sci. China Chem. **68**(4), 1418–1425 (2024).

[232] H. Li, B. Yu, and H. Yu, “An Efficient and Stable Inverted Structure Organic Solar Cell Using ZnO Modified by 2D ZrSe2 as a Composite Electron Transport Layer,” Adv. Funct. Mater. **34**(37), 2402128 (2024).

[233] L. Yan, Y. Wang, W. Zhao, H. Zha, H. Song, H. Hao, Y. Hao, Q. Luo, F. Liu, Y. Yang, Q. Su, H. Wang, and C.Q. Ma, “Simultaneous UV and air stability improvement of organic solar cells enabled by carbon-coated zinc oxide as cathode buffer layer,” Cell Rep. Phys. Sci. **4**(11), 101654 (2023).

[234] J. Jang, J.H. Kim, S. Lee, C.M. Oh, I.W. Hwang, S. Kim, A. Park, D. Kang, C. Jang, T. Ki, H. Kim, and K. Lee, “Efficient Flexible Organic Solar Cells with a Low-Temperature-Processed Al-Doped Zinc Oxide Electron Transport Layer,” ACS Appl. Energy Mater. **6**(18), 9778–9787 (2023).

[235] P. Wang, H. Wang, Y. Mao, H. Zhang, F. Ye, D. Liu, and T. Wang, “Organic Ligands Armored ZnO Enhances Efficiency and Stability of CsPbI2Br Perovskite Solar Cells,” Advanced Science **7**(21), 2000421 (2020).

[236] F. Deng, X. Li, X. Lv, J. Zhou, Y. Chen, X. Sun, Y.Z. Zheng, X. Tao, and J.F. Chen, “Low-Temperature Processing All-Inorganic Carbon-Based Perovskite Solar Cells up to 11.78% Efficiency via Alkali Hydroxides Interfacial Engineering,” ACS Appl. Energy

Mater. **3**(1), 401–410 (2020).

[237] Z. Niu, W. Liu, K. Wang, W. Sun, X. Huo, Y. Miao, T. You, and P. Yin, "Acetate-Assisted Buried Interface Engineering for Highly Efficient Carbon-Based CsPbI2Br Perovskite Solar Cells," ACS Appl. Energy Mater. **7**(9), 3635–3644 (2024).

[238] J. Wang, X. Wu, Y. Liu, Q. Xue, H.L. Yip, A.K.Y. Jen, and Z. Zhu, "Interface Engineering for All-Inorganic CsPbIBr2 Perovskite Solar Cells with Enhanced Power Conversion Efficiency over 11%," Energy Technology **9**(11), (2021).

[239] L. Yan, Q. Xue, M. Liu, Z. Zhu, J. Tian, Z. Li, Z. Chen, Z. Chen, H. Yan, H.L. Yip, and Y. Cao, "Interface Engineering for All-Inorganic CsPbI2Br Perovskite Solar Cells with Efficiency over 14%," Advanced Materials **30**(33), 1802509 (2018).

[240] J. He, J. Su, Z. Lin, J. Ma, L. Zhou, S. Zhang, S. Liu, J. Chang, Y. Hao, J. He, J. Su, Z. Lin, J. Ma, L. Zhou, S. Zhang, J. Chang, Y. Hao, and S. Liu, "Enhanced Efficiency and Stability of All-Inorganic CsPbI2Br Perovskite Solar Cells by Organic and Ionic Mixed Passivation," Advanced Science **8**(17), 2101367 (2021).

[241] J. Bahadur, S.W. Cho, P. Pandey, J. Ryu, S. Yoon, D.G. Lee, J.T. Song, J.S. Cho, and D.W. Kang, "Surface defect passivation of All-Inorganic CsPbI2Br perovskites via fluorinated ionic liquid for efficient Outdoor/Indoor photovoltaics processed in ambient air," Appl. Surf. Sci. **637**, (2023).

[242] C. Qiu, Y. Wu, J. Song, W. Wang, and Z. Li, "Efficient Planar Perovskite Solar Cells with ZnO Electron Transport Layer," Coatings **12**(12), (2022).

[243] Y. Li, Y. Zhang, P. Zhu, J. Li, J. Wu, J. Zhang, X. Zhou, Z. Jiang, X. Wang, and B. Xu, "Achieving 17.46% Efficiency CsPbI2Br Perovskite Solar Cells via Multifunction Lead Chloride-Modified ZnO Electron Transporting Layer," Adv. Funct. Mater. **33**(52), (2023).

[244] J. Li, J. Yang, J. Ma, J. Liang, Y. Liu, X. Hu, C. Chen, W. Yang, J. Min, Q. Bao, G. Fang, and C. Tao, "Minimizing Open-Circuit voltage deficit via interface engineering for highly efficient CsPbI2Br perovskite solar cells," Chemical Engineering Journal **417**, 129247 (2021).

[245] T. Huma, N. Hakimi, M. Younis, T. Huma, Z. Ge, and J. Feng, "MgO Heterostructures: From Synthesis to Applications," Nanomaterials **12**(15), (2022).

[246] J. Cao, B. Wu, R. Chen, Y. Wu, Y. Hui, B.W. Mao, and N. Zheng, "Efficient, Hysteresis-Free, and Stable Perovskite Solar Cells with ZnO as Electron-Transport Layer: Effect of Surface Passivation," Advanced Materials **30**(11), (2018).

[247] J. Dagar, S. Castro-Hermosa, G. Lucarelli, F. Cacialli, and T.M. Brown, "Highly efficient perovskite solar cells for light harvesting under indoor illumination via solution processed SnO2/MgO composite electron transport layers," Nano Energy **49**, 290–299 (2018).

[248] H. Wang, H. Li, S. Cao, M. Wang, J. Chen, and Z. Zang, "Interface Modulator of Ultrathin

Magnesium Oxide for Low-Temperature-Processed Inorganic CsPbIBr2 Perovskite Solar Cells with Efficiency Over 11%," Solar RRL **4**(9), (2020).

[249] Q. Wang, F. Zu, P. Caprioglio, C.M. Wolff, M. Stolterfoht, M. Li, S.H. Turren-Cruz, N. Koch, D. Neher, and A. Abate, "Large Conduction Band Energy Offset Is Critical for High Fill Factors in Inorganic Perovskite Solar Cells," ACS Energy Lett. **5**(7), 2343–2348 (2020).

[250] S. Huang, B. Kang, L. Duan, and D. Zhang, "Highly efficient inverted polymer solar cells by using solution processed MgO/ZnO composite interfacial layers," J. Colloid Interface Sci. **583**, 178–187 (2021).

[251] X. Guo, H. Dong, W. Li, N. Li, and L. Wang, "Multifunctional MgO layer in perovskite solar cells," ChemPhysChem **16**(8), 1727–1732 (2015).

[252] Z. Yelzhanova, | Gaukhar Nigmetova, | Dana Mukasheva, H.P. Parkhomenko, | Gulzhan Zhumadil, D. Aidarkhanov, M. Kaikanov, | Timur Elebessov, T. Wang, A. Kalmakhanbet, D. Duan, H. Hu, | Tri, T. Pham, | Mannix, P. Balanay, | Askhat, N. Jumabekov, | Annie Ng, and A. Ng, "Solution-Processed Magnesium Oxide Buffer Layer for Improved Stability of CsPbI 2 Br Perovskite Solar Cells," (2026).

[253] Z. Kang, H. Si, M. Shi, C. Xu, W. Fan, S. Ma, A. Kausar, Q. Liao, Z. Zhang, and Y. Zhang, "Kelvin probe force microscopy for perovskite solar cells," Sci. China Mater. **62**(6), 776–789 (2019).

[254] M. Zayed, N. Nasser, M. Shaban, H. Alshaikh, H. Hamdy, and A.M. Ahmed, "Effect of morphology and plasmonic on au/zno films for efficient photoelectrochemical water splitting," Nanomaterials **11**(9), (2021).

[255] S. Visweswaran, R. Venkatachalapathy, M. Haris, and R. Murugesan, "Characterization of MgO thin film prepared by spray pyrolysis technique using perfume atomizer," Journal of Materials Science: Materials in Electronics **31**(17), 14838–14850 (2020).

[256] Z. Su, D. Xu, Q. Ma, K. Gao, C. Zhang, C. Xing, S. Wang, W. Shi, X. Wang, K. Li, J. Hui, and X. Yang, "Atomic Layer Deposited ZnO–SnO2 Electron Transport Bilayer for Wide-Bandgap Perovskite Solar Cells," Solar RRL **7**(3), 2201026 (2023).

[257] S. Wang, S. Frisch, H. Zhang, O. Yildiz, M. Mandal, N. Ugur, B. Jeong, C. Ramanan, ac Denis Andrienko, H.I. Wang, M. Bonn, P.W. M Blom, M. Kivala, W. Pisula, and T. Marszalek, "Grain engineering for improved charge carrier transport in two-dimensional lead-free perovskite field-effect transistors †," **9**, 2633 (2022).

[258] M.Z. Toe, W.K. Tan, H. Muto, G. Kawamura, A. Matsuda, and S.Y. Pung, "Evaluation of the Structural, Optical and Photoconversion Efficiency of ZnO Thin Films Prepared Using Aerosol Deposition," Applied Sciences 2023, Vol. 13, Page 1905 **13**(3), 1905 (2023).

[259] Y. Litaiem, "Simple and low cost growth of flower-like ZnO onto ITO/PET and FTO substrates through hydrothermal process for photoelectrochemical applications," JMSA **6**(2),

(2022).

[260] Y. Zhang, T. Wang, Y. Wang, J. Chen, L. Peng, X. Liu, and J. Lin, "Interface modification for efficient carbon-electrode CsPbI2Br perovskite solar cells using ionic liquid," Nanotechnology **35**(20), (2024).

[261] H. Xiao, C. Zuo, F. Liu, and L. Ding, "Drop-coating produces efficient CsPbI2Br solar cells," Journal of Semiconductors **42**(5), (2021).

[262] A.R. Kirmani, T.A. Byers, Z. Ni, K. Vansant, D.K. Saini, R. Scheidt, X. Zheng, T.B. Kum, I.R. Sellers, L. Mcmillon-Brown, J. Huang, B. Rout, and J.M. Luther, "Unraveling radiation damage and healing mechanisms in halide perovskites using energy-tuned dual irradiation dosing," (n.d.).

[263] D.T. Nguyen, D. Walter, K.J. Weber, T. Duong, and T.P. White, "Simulating Proton Radiation Tolerance of Perovskite Solar Cells for Space Applications," Advanced Energy and Sustainability Research **4**(12), (2023).

[264] Z. Huan, Y. Zheng, K. Wang, Z. Shen, W. Ni, J. Zu, and Y. Shao, "Advancements in radiation resistance and reinforcement strategies of perovskite solar cells in space applications," J. Mater. Chem. A Mater. **12**(4), 1910–1922 (2024).

[265] M.M. Solovan, A.I. Mostovyi, D. Aidarkhanov, H.P. Parkhomenko, G. Akhtanova, N. Schopp, E.A. Asare, D. Nauruzbayev, M. Kaikanov, A. Ng, and V. V. Brus, "Extreme Radiation Resistance of Self-Powered High-Performance Cs0.04Rb0.04(FA0.65MA0.35)0.92Pb(I0.85Br0.14Cl0.01)3 Perovskite Photodiodes," Adv. Opt. Mater. **11**(10), 2203001 (2023).

[266] H.S. Rao, W.-H. Chiu, S.-H. Chen, M.-C. Wu, and K.-M. Lee, "Impact of proton radiation on the performance of single-junction perovskite solar cells for space applications," Solar Energy Materials and Solar Cells **295**, 114015 (2026).

[267] B.K. Durant, H. Afshari, S. Singh, B. Rout, G.E. Eperon, and I.R. Sellers, "Tolerance of Perovskite Solar Cells to Targeted Proton Irradiation and Electronic Ionization Induced Healing," ACS Energy Lett. **6**(7), 2362–2368 (2021).

[268] V. V. Brus, F. Lang, J. Bundesmann, S. Seidel, A. Denker, B. Rech, G. Landi, H.C. Neitzert, J. Rappich, and N.H. Nickel, "Defect Dynamics in Proton Irradiated CH3NH3PbI3 Perovskite Solar Cells," Adv. Electron. Mater. **3**(2), 1600438 (2017).

[269] A.D. Wright, C. Verdi, R.L. Milot, G.E. Eperon, M.A. Pérez-Osorio, H.J. Snaith, F. Giustino, M.B. Johnston, and L.M. Herz, "ARTICLE Electron-phonon coupling in hybrid lead halide perovskites," (2016).

[270] P. Luo, X.Y. Sun, Y. Li, L. Yang, W.Z. Shao, L. Zhen, and C.Y. Xu, "Correlation between Structural Evolution and Device Performance of CH3NH3PbI3Solar Cells under Proton Irradiation," ACS Appl. Energy Mater. **4**(12), 13504–13515 (2021).

[271] S. Erickson, C. Lum, K. Stephens, M. Parashar, D.K. Saini, B. Rout, C. Park, T.J. Peshek, L. McMillon-Brown, and S. Ghosh, "Elucidating early proton irradiation effects in metal halide perovskites via photoluminescence spectroscopy," IScience **28**(1), 111586 (2024).

[272] F. Lang, N.H. Nickel, J. Bundesmann, S. Seidel, A. Denker, S. Albrecht, V. V. Brus, J. Rappich, B. Rech, G. Landi, and H.C. Neitzert, "Radiation Hardness and Self-Healing of Perovskite Solar Cells," Advanced Materials **28**(39), 8726–8731 (2016).

[273] W.O. Herrera Martínez, N.B. Correa Guerrero, V.A. Gómez Andrade, M. Alurralde, and M.D. Perez, "Evaluation of the resistance of halide perovskite solar cells to high energy proton irradiation for space applications," Solar Energy Materials and Solar Cells **238**, 111644 (2022).

[274] H. Huang, W. Qian, C. Dai, Y. Zhao, Y. Liang, R. Lei, X. Wang, S. Yang, and J. Xue, "Unraveling the Degradation and Air-Induced Healing Mechanisms of Halide Perovskites under Proton Irradiation," ACS Appl. Mater. Interfaces **16**(47), 65108–65118 (2024).

[275] B. Xue, L. Zhang, N. Liu, T. Zhang, and Y. Liang, "Radiation resistance comparison of MAPbI3 and MAPbBr3 perovskite thin films under 100 keV proton irradiation," Vacuum **243**, 114832 (2026).

[276] P. Luo, X.Y. Sun, H. Jiang, L. Yang, Y. Li, W.Z. Shao, L. Zhen, and C.Y. Xu, "Enhanced proton irradiation resistance in Cs-doped CH3NH3PbI3 films and solar cells," Journal of Energy Chemistry **69**, 261–269 (2022).

[277] J. Shin, K.Y. Baek, J. Lee, W. Lee, J. Kim, J. Jang, J. Park, K. Kang, K. Cho, and T. Lee, "Proton irradiation effects on mechanochemically synthesized and flash-evaporated hybrid organic–inorganic lead halide perovskites," Nanotechnology **33**(6), 065706 (2021).

[278] C. Costa, M. Manceau, T. Nuns, S. Duzellier, and R. Cariou, "In-Situ & Ex-Situ Study of Protons and Electrons Irradiations of Perovskite Solar Cells," IEEE, 1–1 (2023).

[279] H. Afshari, S.A. Chacon, S. Sourabh, T.A. Byers, V.R. Whiteside, R. Crawford, B. Rout, G.E. Eperon, and I.R. Sellers, "Radiation tolerance and self-healing in triple halide perovskite solar cells," APL Energy **1**(2), (2023).

[280] H.P. Parkhomenko, M.M. Solovan, S. Sahare, A.I. Mostovyi, D. Aidarkhanov, N. Schopp, T. Kovaliuk, M. Kaikanov, A. Ng, and V. V. Brus, "Impact of a Short-Pulse High-Intense Proton Irradiation on High-Performance Perovskite Solar Cells," Adv. Funct. Mater. **34**(10), 2310404 (2024).

[281] E. Aleksanyan, V. Harutyunyan, A. Badalyan, N. Grigoryan, N. Margaryan, A. Manukyan, L. Matevosyan, H. Okrepka, V. Trepalin, Y. Ding, M. Zhukovskyi, M. Kuno, A. Aprahamian, and K. Manukyan, "Superior Stability of CsPbBr3 Films under High-Energy Proton Irradiation," Journal of Physical Chemistry C **128**(40), 16854–16860 (2024).

[282] G. Nigmetova, Z. Yelzhanova, G. Zhumadil, H.P. Parkhomenko, M. Tilegen, X. Zhou,

V. Pavlenko, A. Beisenbayev, D. Aidarkhanov, A.N. Jumabekov, M. Kaikanov, T.T. Pham, M.P. Balanay, C.K. Lim, Y. Wang, H. Hu, and A. Ng, "Controlling the Growth of Cs2PbX4 Nanostructures Enhances the Stability of Inorganic Cesium-Based Perovskite Solar Cells for Potential Low Earth Orbit Applications," ACS Appl. Mater. Interfaces, (2025).

[283] M.K.A. Mohammed, B.T. Al-Azraq, A.K. Al-Mousoi, E.Y. Salih, A. Rajiv, B.N. Sahu, M.F. Rahman, and E. Akman, "Multiphysics insights into CsPbI3 perovskite photovoltaics under proton irradiation," Renew. Energy **256**, 124571 (2026).

[284] D. Hughes, S.M.P. Meroni, J. Barbé, D. Raptis, H.K.H. Lee, K.C. Heasman, F. Lang, T.M. Watson, and W.C. Tsoi, "Proton Radiation Hardness of Perovskite Solar Cells Utilizing a Mesoporous Carbon Electrode," Energy Technology **9**(12), (2021).

[285] A.Y. Boboev, N.Y. Yunusaliyev, G.G. Tojiboyev, O. Shk Muminov, and S.R. Kadirov, "SRIM simulation of irradiation damage by protons in ZnO:S compound," Journal of Ovonic Research **21**(6), 781–788 (n.d.).

[286] W. Siiocklev, and A.W.T. Read, "A SOLUBLE PROBLEM IN ENERGY HANDS Statistics of the Recombinations of Holes and Electrons," (1952).

[287] W. Chu, Q. Zheng, O. V. Prezhdo, J. Zhao, and W.A. Saidi, "Low-frequency lattice phonons in halide perovskites explain high defect tolerance toward electron-hole recombination," Sci. Adv. **6**(7), 7453–7467 (2020).

[288] A.R. Kirmani, and I.R. Sellers, "Are metal-halide perovskite solar cells really radiation tolerant?," Joule **9**(3), (2025).

[289] H.P. Parkhomenko, A.I. Mostovyi, G. Akhtanova, M.M. Solovan, M. Kaikanov, N. Schopp, and V. V. Brus, "Self-Healing of Proton-Irradiated Organic Photodiodes and Photovoltaics (Adv. Energy Mater. 37/2023)," Adv. Energy Mater. **13**(37), (2023).

[290] X. Han, X. Wang, J. Feng, H. Huang, Z. Zhu, T. Yu, Z. Li, and Z. Zou, "Carrier Mobility Enhancement in (121)-Oriented CsPbBr3Perovskite Films Induced by the Microstructure Tailoring of PbBr2Precursor Films," ACS Appl. Electron. Mater. **3**(1), 373–384 (2021).

[291] M. Salman Kiani, H.P. Parkhomenko, M. Mangrulkar, S. Aigarayeva, A. Akhanuly, E.O. Shalenov, A. Ng, and A.N. Jumabekov, "Stepping toward Portable Optoelectronics with SnO 2 Quantum Dot-Based Electron Transport Layers," (2023).

[292] Q. Zeng, X. Zhang, C. Liu, T. Feng, Z. Chen, W. Zhang, W. Zheng, H. Zhang, and B. Yang, "Inorganic CsPbI2Br Perovskite Solar Cells: The Progress and Perspective," Solar RRL **3**(1), (2019).

[293] G.A. Nemnes, C. Besleaga, A.G. Tomulescu, A. Palici, L. Pintilie, A. Manolescu, and I. Pintilie, "How measurement protocols influence the dynamic J-V characteristics of perovskite solar cells: Theory and experiment," Solar Energy **173**, 976–983 (2018).

[294] Y. Long, K. Liu, Y. Zhang, and W. Li, "Ambient air temperature assisted crystallization

for inorganic CsPbI2Br perovskite solar cells," Molecules **26**(11), (2021).

[295] M. Saliba, and L. Etgar, "Current density mismatch in Perovskite solar cells," ACS Energy Lett. **5**(9), 2886–2888 (2020).

[296] M. Saliba, E. Unger, L. Etgar, J. Luo, and T.J. Jacobsson, "A systematic discrepancy between the short circuit current and the integrated quantum efficiency in perovskite solar cells," Nat. Commun. **14**(1), 5445 (2023).

[297] J. Ji, X. Liu, H. Jiang, M. Duan, B. Liu, H. Huang, D. Wei, Y. Li, and M. Li, "Two-Stage Ultraviolet Degradation of Perovskite Solar Cells Induced by the Oxygen Vacancy-Ti4+ States," IScience **23**(4), (2020).

[298] D. Yun, Y. Cho, H. Shin, and G.H. Kim, "Development of High-Efficiency and High-Stability Perovskite Solar Cells with Space Environmental Resistance," Energies (Basel). **18**(13), (2025).

[299] R. Pallotta, S. Cavalli, M. Degani, and G. Grancini, "Smart Materials to Empowering Perovskite Solar Cells with Self-Healing Capability," Small Struct. **5**(5), (2024).

[300] E.O. Shalenov, K.N. Dzhumagulova, T.S. Ramazanov, A. Tikhonov, and M. Kaikanov, "On plasma neutralization of the ion beam," J. Phys. Conf. Ser. **1697**(1), (2020).

[301] H.P. Parkhomenko, Y. Yerlanuly, A.K. Azamat, C.-Q. Ma, M. Kaikanov, A. Ng, A.N. Jumabekov, and K. Astana, "Short-pulsed proton irradiation stability in slot-die-coated bifacial perovskite photodetectors," Scientific Reports 2025 16:1 **16**(1), 3224- (2025).

[302] T. Zhang, L. Zhang, N. Liu, B. Xue, and Y. Liang, "Performance degradation in P3HT-based perovskite solar cells induced by proton irradiation at room temperature and 150 °C," Solar Energy Materials and Solar Cells **294**, 113919 (2026).

[303] N. Liu, L. Zhang, Y. Liang, B. Xue, and D. Wang, "Effects of Carrier Transport Layers on Performance Degradation in Perovskite Solar Cells under Proton Irradiation," ACS Appl. Energy Mater. **6**(12), 6673–6680 (2023).

[304] Y.M. Kim, J.K. Park, W.S. Ko, K.N. Kim, and G.W. Lee, "Characterization of ZnO Thin-film Transistors with Various Active Layer Structures after Exposure to Different Proton Energies," Journal of Semiconductor Technology and Science **24**(2), 63–68 (2024).

[305] L. Zhou, X. Guo, Z. Lin, J. Ma, J. Su, Z. Hu, C. Zhang, S. (Frank) Liu, J. Chang, and Y. Hao, "Interface engineering of low temperature processed all-inorganic CsPbI2Br perovskite solar cells toward PCE exceeding 14%," Nano Energy **60**, 583–590 (2019).

[306] J. He, J. Su, Z. Ning, J. Ma, L. Zhou, Z. Lin, J. Zhang, S. Liu, J. Chang, and Y. Hao, "Improved Interface Contact for Highly Stable All-Inorganic CsPbI2Br Planar Perovskite Solar Cells," ACS Appl. Energy Mater. **3**(6), 5173–5181 (2020).

[307] K. Zheng, J. Ge, C. Liu, Q. Lou, X. Chen, Y. Meng, X. Yin, S. Bu, C. Liu, and Z. Ge, "Improved phase stability of CsPbI2Br perovskite by released microstrain toward highly

efficient and stable solar cells," InfoMat **3**(12), 1431–1444 (2021).

[308] A. Wang, J. Wang, X. Niu, C. Zuo, F. Hao, and L. Ding, "Inhibiting octahedral tilting for stable CsPbI2Br solar cells," InfoMat **4**(1), e12263 (2022).

[309] S. Cao, L. Wang, X. She, W. Li, L. Wei, X. Xiong, Z. Wang, J. Li, H. Tian, X. Cui, M. Zhang, H. Sun, D. Yang, and X. Liu, "Enhanced Efficiency and Stability of Inverted CsPbI2Br Perovskite Solar Cells via Fluorinated Organic Ammonium Salt Surface Passivation," Langmuir, (2023).

[310] S. Zhang, Y. Li, J. Huang, S. Li, Z. Wang, Z. Peng, J. Chen, and J. Chen, "Interface modification of imidazolium ionic liquid toward efficient and stable carbon-electroded CsPbI2Br perovskite solar cells," J. Power Sources **660**, 238495 (2025).